Modelling Breast Cancer Treatment

Mechanically Coupled Reaction-Diffusion model to predict tumour response in HER2+ patients

Eva Slingerland

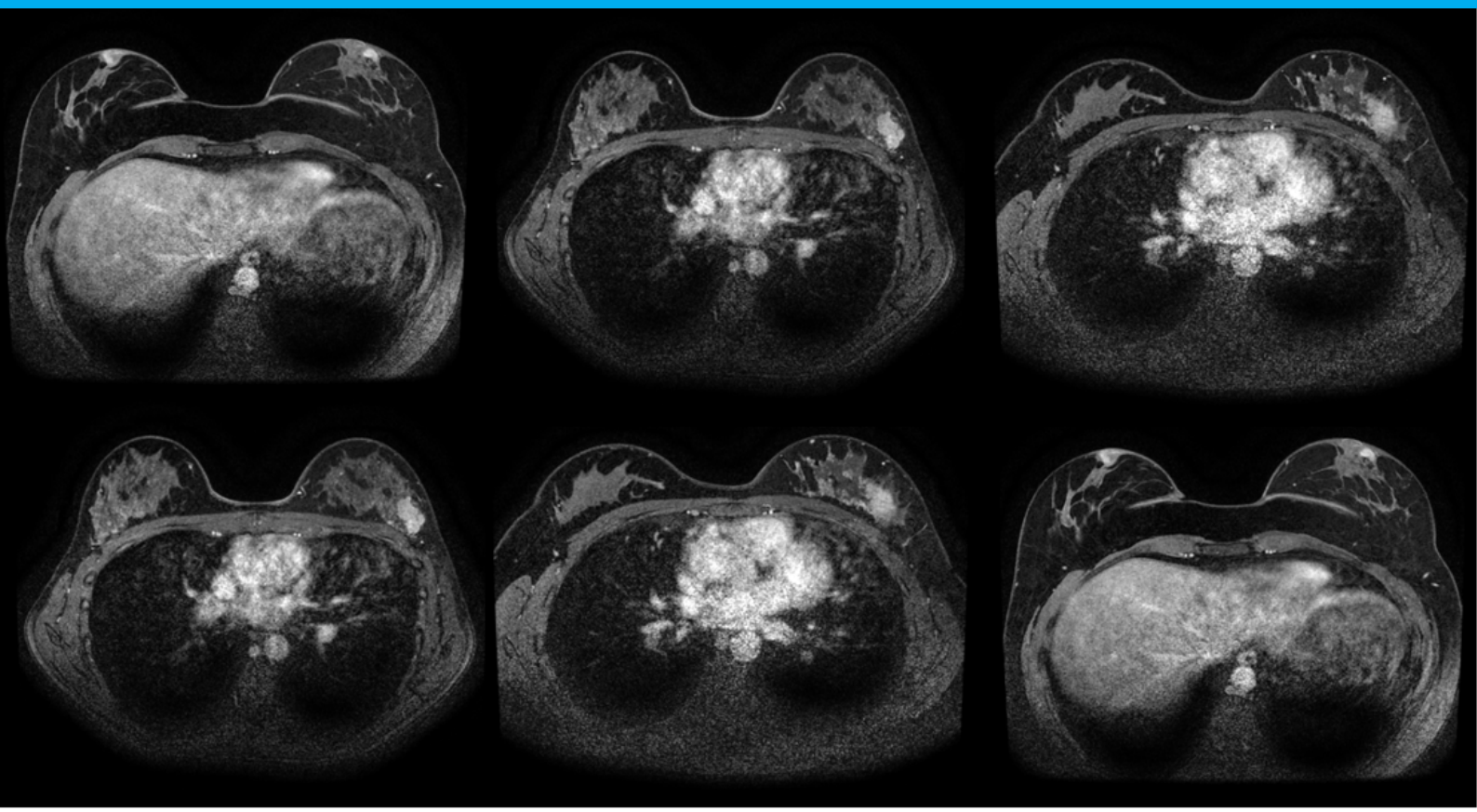

TU Delft

Erasmus MC

Modelling Breast Cancer Treatment

Mechanically Coupled Reaction-Diffusion model to predict tumour response in HER2+ patients

by

Eva Slingerland

to obtain the degree of Master of Science
at the Delft University of Technology,
to be defended publicly on Wednesday August 31st, 2022 at 10:30 AM.

Student number:	4572580	
Project duration:	November 15th, 2021 – August 31st, 2022	
Thesis committee:	Prof. dr. ir. M. van Gijzen,	TU Delft, supervisor
	Dr. ir. L. Rens,	TU Delft, supervisor
	Dr. A. Jager,	Erasmus MC
	Prof. ir. A. Heemink,	TU Delft

An electronic version of this thesis is available at http://repository.tudelft.nl/.

TU Delft

Abstract

HER2+ breast cancer patients suffer from aggressive tumours that often respond well to treatment compared to HER2- patients. Currently, patients are all treated with the same number of anti-tumour treatments, although the required number to eradicate all tumour cells varies between patients. The goal is thus to have an individualised model based on an MRI before the start of therapy and an MRI after several rounds of therapy that predicts how many treatments are needed to eradicate all tumour cells. In the previous MSc thesis by N. Oudhof, a two-dimensional spatiotemporal mechanically coupled reaction-diffusion model was implemented. This was used to model the number of tumour cells in each position of the breast, where the mechanics are included to simulate the behaviour of the surrounding tissue.
The goal of this thesis is to improve that model by improving the calibration in which the patient-specific parameters are optimised, by taking into account the treatment schedule of the patients and by extending the model to three dimensions. For calibration, the first and second MRI scans are used and a third MRI is used for validation. To simulate the chemotherapy, both the Kety-Tofts model and a Normalised Blood Volume Map are applied, of which the latter appeared the best option. In 2D, four models are implemented: the reaction-diffusion models with and without mechanics and with and without chemotherapy term. These were compared by analysing the predicted and measured tumour densities for a cohort of three HER2+ patients. For 3D, only the basic reaction-diffusion and chemotherapy-incorporated reaction-diffusion models are implemented. The models are compared in terms of mean squared error, global relative error and concordance correlation coefficient. For both 2D and 3D, the models without chemotherapy gave slightly better results in terms of these measures, although the differences between the models were rather small. To determine the required number of therapy rounds, it is however better to use the chemotherapy-incorporated models because they offer more possibilities to simulate different treatment strategies. The computation time of the 3D implementation should be reduced before the mechanics can be included, which will allow conclusions to be drawn on which model is most accurate. Other directions for future improvements include using the second MRI to calculate the chemotherapy concentrations after calibration, adding an immunotherapy term and increasing the number of patients.

Preface

This thesis is my final project for the Master Applied Mathematics at the Delft University of Technology and thus also marks the end of my study time here in Delft. When I started my bachelor here six years ago, I had no idea that there were so many different aspects of mathematics and I have truly enjoyed seeing its application to such a relevant theme with this thesis. Over the past 8 months, a lot of people have asked me what my thesis was about, often out of interest but sometimes also simply out of politeness. Most of them view mathematics as a very complex topic, so while they were bracing themselves for some complicated answer, I simply told them I was working on a mathematical model to predict the response of a tumour to treatment for breast cancer patients. Their facial expressions always went from scared, to surprised and ended in excitement, which also put a smile on my face every time it happened.

I am extremely grateful to have had Martin as a supervisor, thank you for all your guidance and support. During all these months, you have truly helped me to stay motivated despite the setbacks and you have encouraged me to present my work at a workshop, which was a great experience. You always took the time to catch up, freed up your calendar for an extra meeting if I got stuck on something and also showed interest in my personal well-being. Besides our academic discussions, I also enjoyed our political conversations on for example the government policy regarding the pandemic or the university policy regarding education-related issues. In addition, I would also like to thank Agnes for supervising me. It was great to get insights from the practical field and you have really helped me with some of the medical background. I appreciate that you found time in your busy schedule for our short but efficient meetings. Every time you got called away for a medical emergency during these meetings reminded me of the relevance of this work. Thank you also for giving me the opportunity to present our work during the regional breast cancer meeting, where we have excited many people that can hopefully help with this topic in the future.

Finally, I would also like to express my appreciation to all my friends and family who have supported and motivated me during my studies. I would like to give a small shout-out to some of my friends that have joined me for lunches, cups of coffee (or in my case tea), walks over campus and study sessions during this thesis: Marijn, Sam, Salomon, Charlotte, Rocky, Simone, Roel and Maaike. Last but not least, a big thank you to Roel, Federico and David for their feedback on my thesis. Thank you all!

Eva Slingerland
Delft, August 2022

List of Abbreviations

MRI	Magnetic resonance imaging
EMC	Erasmus Medical Center
HER	Human epidermal growth factor receptor
RD	Reaction-Diffusion
MCRD	Mechanically Coupled Reaction-Diffusion
DIRD	Drug-Incorporated Reaction-Diffusion
DIMCRD	Drug-Incorporated Mechanically coupled reaction-diffusion
2D	Two-dimensional
3D	Three-dimensional
NAT	Neoadjuvant therapy
DW-MRI	Diffusion weighted magnetic resonance imaging
DCE-MRI	Dynamic contrast-enhanced magnetic resonance imaging
pCR	Pathologic complete response
rCR	Radiologic complete response
ADC	Apparent diffusion coefficient
CA	Contrast agent
ROI	Region of interest
KT	Kety-Tofts
NBVM	Normalised Blood Volume Map
AUC	Area Under the Curve
FDM	Finite difference method
LM	Levenberg-Marquardt
TRF	Trust region reflective
AIF	Arterial input function
LC	Linear conversion
NLC	Non-linear conversion
SPGRE	Spoiled gradient echo
MSE	Mean squared error
GRE	Global relative error
CCC	Concordance correlation coefficient

Contents

1 Introduction **1**
- 1.1 Context . . . 1
- 1.2 Problem Description . . . 1
- 1.3 Scope . . . 2
- 1.4 Document Structure . . . 2

2 Medical background **3**
- 2.1 HER2+ patients . . . 3
- 2.2 Tumour growth . . . 3
- 2.3 Treatment . . . 4
- 2.4 MRI scans . . . 4

3 Mathematical Models **7**
- 3.1 Mechanically Coupled Reaction-Diffusion Model . . . 7
- 3.2 Drug-Incorporated Mechanically Coupled Reaction-Diffusion Model . . . 9
- 3.3 Overview of variables and parameters . . . 11
- 3.4 Model overview . . . 11

4 Research questions and methodology **13**
- 4.1 Research Questions . . . 13
- 4.2 Methodology . . . 13
  - 4.2.1 Data . . . 13
  - 4.2.2 Calibration . . . 14
  - 4.2.3 Chemotherapy extension . . . 14
  - 4.2.4 Three-dimensional extension . . . 14

5 Implementation **15**
- 5.1 Data . . . 15
- 5.2 Modelling pipeline . . . 16
- 5.3 Discretisations . . . 17
  - 5.3.1 Reaction-Diffusion equation . . . 18
  - 5.3.2 Linear-Elastic equation . . . 20
- 5.4 Calibration . . . 21
  - 5.4.1 Parameter reduction . . . 21
  - 5.4.2 Non-linear least squares algorithm . . . 23

6 Chemotherapy extension **25**
- 6.1 Kety-Tofts model . . . 25
  - 6.1.1 Overview of steps . . . 25
  - 6.1.2 Choosing arterial input function . . . 26
  - 6.1.3 Deriving CA concentration from DCE scans . . . 28
  - 6.1.4 Fitting parameters . . . 30
  - 6.1.5 Deriving concentration of drug in plasma . . . 31
- 6.2 Normalised Blood Volume Map . . . 32
  - 6.2.1 Overview of steps . . . 32
  - 6.2.2 Estimating drug decay rate . . . 32

6.3 Comparison of methods . . . 34
6.4 Model analysis . . . 36
6.4.1 Influence of D_0 . . . 36
6.4.2 Influence of α . . . 36
6.4.3 Influence of $k(\overline{x})$ . . . 37
6.4.4 Calibration with all 3 MRI scans . . . 40
6.4.5 Influence of slice thickness . . . 41
6.5 Results and comparison of models . . . 42

7 Three-dimensional extension **47**
7.1 Discretisations . . . 47
7.2 Influence of slice thickness . . . 48
7.3 Downsampled (x, y) plane . . . 49
7.4 Comparison of 3D model versus 2D model . . . 50
7.5 Results and comparison of models . . . 51

8 Discussion and recommendations **53**
8.1 Model implementation . . . 53
8.2 Chemotherapy . . . 55
8.3 Results . . . 56

9 Conclusion **59**

A Appendix **61**
A.1 Acquisition parameters for the first MRI scan of p_2 . . . 61
A.2 Pre-processing information . . . 61
A.2.1 Registration . . . 61
A.2.2 Tissue segmentation . . . 62
A.2.3 Tumour density . . . 62
A.3 Stability criterion . . . 63
A.4 Proof for Section 6.1.2 . . . 65
A.5 Poster for Workshop . . . 70

1 Introduction

Cancer is one of the leading causes of death worldwide. The most frequently diagnosed and primary cause of death by cancer for women is breast cancer [1], and it is estimated that one in eight women will be diagnosed with breast cancer during their life [2]. As more and more research is done into new treatment options and the behaviour of tumours in response to them, the chances of survival increase. Nowadays multiple treatments are possible depending on the size and type of tumour. Chemotherapy, which reduces the tumour size, is often given in preparation for surgery where the tumour is removed. The growth of a tumour is a complex process and its response to chemotherapy is often still unpredictable. Much research has been done into modelling this process to gain more insights into the underlying dynamics and to optimise the treatment plan based on the new insights. If it is possible to perfectly model the growth of a tumour, then an optimal treatment strategy can be determined where for example the time between rounds of chemotherapy or the used components of chemotherapy is correctly adjusted to eradicate as many tumour cells as possible.

Attention for patient-specific models based on *magnetic resonance images* (MRI) has grown over the past decade [3] as this is a non-invasive method to obtain information on the tumour and it greatly aids the doctor in determining a treatment plan. In more recent years, promising results were accomplished with a mathematical model that predicts the tumour density and its response to chemotherapy in the breast region [4–9]. In this thesis, this model is applied to a set of MRI scans of breast cancer patients.

In Section 1.1 of this introductory chapter, some context is provided on the topic and the collaboration with Erasmus Medical Center. Section 1.2 further describes the problem, Section 1.3 lays down the scope of this thesis and Section 1.4 contains the outline of this thesis.

1.1. Context

The *Erasmus Medical Center* (EMC) is a Dutch hospital that has been treating cancer patients for many years. In 2020 the EMC Cancer Institute was opened, where doctors and researchers collaborate to find new treatment possibilities and work together to directly implement them. It enables patient-tailored therapy to provide the best possible care. In the past years, the collaboration between the EMC and the Delft University of Technology has intensified as the technological and medical sectors can provide useful insights to each other. Under this collaboration, the department of Numerical Analysis from the Delft University of Technology works together with the department of Oncology of EMC.

1.2. Problem Description

The growth behaviour of a tumour depends on many factors, including some genetic ones. The *human epidermal growth factor receptor 2* (HER2) is a gene that has been shown to cause more aggressive breast cancer tumours. If a patient is HER2+, meaning the gene is overexpressed, the chances of survival are significantly lower compared to HER2- patients [10]. On the other hand, these HER2+

tumours often respond well to anti-tumour treatment where the eradication of the tumour cells is the main goal. Although the number of treatments required for this varies greatly from patient to patient, currently HER2+ patients at EMC are treated with the same number of anti-tumour treatments. These treatment rounds do not only destroy tumour cells but also destroy healthy cells. It therefore comes with many side effects and in addition these treatments are costly. For this reason, EMC wants to be able to determine per patient how many rounds of therapy are needed, because this can both reduce the impact on the patient and improve the long-term prognosis. They thus need a model that can be calibrated with patient-specific data to predict the response of the tumour to therapy. Currently, MRI scans are made during the treatment process to track the response of the tumour to therapy and these scans thus serve as useful input data for the model to predict its behaviour. With this model, the goal is to be able to predict tumour response to therapy, which could aid doctors in determining a patient-specific treatment plan.

1.3. Scope

This thesis explores how a *Mechanically Coupled Reaction-Diffusion* (MCRD) model can be used to predict tumour response to chemotherapy to determine patient-specific treatment plans. Previous research has shown that both this model [3–6] and an extended model [7–9], called the *Drug-Incorporated Mechanically Coupled Reaction-Diffusion* (DIMCRD) model, can be used to this end. In a previous master thesis by Nathalie Oudhof [11], the MCRD model was applied to a dataset of MRI scans of HER2+ patients from EMC to predict tumour growth of breast cancer patients based on their MRI scans. In that research, the treatment schedule of the patients was not taken into account and the model was only implemented in two dimensions (2D). Therefore, this thesis will build upon that research and explore the possibilities of the model by both extending it to the DIMCRD model and extending it to three dimensions (3D). The general research question that we aim to answer is:

How can the MCRD model be improved to achieve better results in modelling chemotherapy and the growth of tumours to determine the correct number of treatment rounds in HER2+ breast cancer patients?

1.4. Document Structure

Following this introductory chapter, Chapter 2 and 3 give necessary background information on concepts and methods that are used in this thesis. Chapter 2 provides medical background on breast cancer and its treatment. Chapter 3 moves on to explain the mathematical models previously described in the literature that will be applied in this research. Based on this background information, the research question is further specified and the corresponding methodology is described in Chapter 4. Following this chapter, the modelling pipeline including the pre-processing steps, discretisations for the 2D model and improvements for the calibration are presented in Chapter 5. Chapter 6 explains how the chemotherapy term can be calculated for the DIMCRD model and includes analyses of the parameters. In that chapter, the results for the different models and patients in 2D are also presented and evaluated. The extension to the three-dimensional model is explained and analysed in Chapter 7. In Chapter 8 the results are discussed and recommendations for future research are given. Last but not least, in Chapter 9 the conclusions are presented.

2

Medical background

This chapter several medical concepts that are used in this thesis are explained. Firstly, background information on HER2+ patients is given in Section 2.1. Next, in Section 2.2 tumour growth is described, which is followed by an explanation of treatment in Section 2.3. In Section 2.4 information is provided on the different types of MRI scans that are used in this thesis.

2.1. HER2+ patients

As explained in the introductory chapter, this thesis focuses on HER2+ patients. Approximately 25% of the breast cancer patients overexpress the HER2 gene, which is sometimes also referred to as the *ERBB2* gene and plays an important role in normal cell growth. Due to the amplification of the gene, the number of receptors at the tumour-cell surface increases. These growth factor receptors bind to growth factors and transmit a signal to the cell to start proliferation. In this way, overexpression of the HER2 gene leads to excessive cellular division and the formation of fast-growing tumours [10]. As a result, cancer in HER2+ patients is more aggressive and has a poor prognosis of survival [12, 13]. Because it can cause cancer, HER2 is called an *oncogene*.

2.2. Tumour growth

To model the growth of tumours, it is important to understand the dynamics between the tumour and the healthy tissue within the breast. The breast tissue of a patient with breast cancer is a heterogeneous mixture of adipose, fibroglandular and tumour tissue. Adipose tissue consists of body fat and fibroglandular tissue is a combination of connective tissue and glandular tissue which contains the ducts of the breast. It has been shown that breast fibroglandular tissue is twice as stiff as adipose tissue, so fibroglandular tissue has higher mechanical properties than adipose tissue [3]. This means that these tissues respond differently when a deformation nearby poses stress on the tissue. As a tumour grows outwards within the breast, it imposes an external force on the surrounding tissue, which leads to deformation and stress in that tissue. In this way a growing tumour displaces surrounding tissue, a phenomenon called *mass effect* in literature [3, 5]. Depending on the stiffness of the surrounding tissue, the mass effect of the tumour causes a change in the energy state of that tissue. The increase in mechanical stress restricts further expansion of the tumour [14]. Note that when tumours are mentioned in this thesis, we always refer to malignant tumours, as benign tumours do not invade the surroundings or spread through the body and are therefore usually harmless.

When talking about cell growth, often the term *doubling time* is used. This refers to the time it takes for a group of cells to double in size. Researchers used to think that the doubling time of tumour cells was constant like normal cells, implying growth to be exponential. A curve describing the total number of tumour cells would thus be J-shaped. So if one cell would take T time to turn into two cells, then two cells would take T time to proliferate into 4 cells, etc. However, researchers found that tumour cells did not grow exponentially but rather logistically [15]. Hence, the growth of tumour cells can be described by a Gompertzian or Sigmoid S-shaped curve for which the doubling time increases with

increasing tumour size, implying that smaller groups of cells grow faster than larger groups of cells [13].

2.3. Treatment

Treatment against cancer can be of various forms like chemotherapy, radiotherapy or surgery. Usually, a combination is used and in this thesis the focus will be on *neoadjuvant therapy* (NAT), which is used in preparation for surgery. This means chemotherapy is applied to the tumour to reduce its size until it is small enough to be removed in surgery [3], although is also often happens that NAT has already eradicated all tumour cells. After removal of the tissue in surgery, the tissue is sent to the lab where it is examined. If there are no more signs of cancer cells present in the tissue, it is called *pathological complete response* (pCR). This means that the treatment completely removed all cancer cells. For HER2+ patients, NAT often leads to pCR. Several studies within the medical field have been done to investigate if *radiologic complete response* (rCR), which refers to the situation where no tumour is visible on the radiologic scans, can predict pCR. Research showed that for HER2+ patients rCR often corresponds to pCR [16]. For this thesis, it is assumed that the tumour densities which are determined based on the MRI scans are equal to the true tumour densities in tissue, so it is assumed that indeed rCR predicts pCR. We will return to this point in the Discussion in Chapter 8. Tumours of HER2+ patients do not decrease into multiple small tumour while treated, but instead they usually just remain in one piece while shrinking.

HER2+ patients are in general treated with nine rounds of treatment at Erasmus MC, consisting of *trastuzumab, pertuzumab, carboplatin* and *paclitaxel* which are all administered intravenously. Both carboplatin and paclitaxel are chemotherapy treatments, meaning that they kill fast-growing cells, which are usually tumour cells as they grow quicker and faster than normal cells. Trastuzumab and pertuzumab are *immunotherapy* treatments, meaning they consists of monoclonal antibodies that attach to the receptors on the tumour cell to stop it from growing and dividing. This addition to the normal chemotherapy treatment for HER2+ patients has significantly improved the prognosis and increased survival rates [10]. One round of treatment consists of three weeks, where in the first week trastuzumab, pertuzumab, carboplatin and paclitaxel are administered, in the second week only paclitaxel is used and in the third week no treatment is given. The next round of therapy starts in the following week with again all four drugs. The dosage of each component varies throughout the weeks. After three or four treatments, an MRI scan is made to see if the tumour has responded to therapy and has decreased in size, and after all nine treatments are finished surgery takes place.

How a tumour grows and responds to treatment of course differs per patient and depends on a big number of factors, like the stage the tumour is in, the location of the tumour, the weight of the patient, etc. However, all HER2+ patients are treated with the same treatment schedule. It is often thought by doctors that a patient-specific treatment schedule that for example dictates the number of treatment rounds that are needed for the best long-term result would work better. This number could be both higher or lower than the current standard of nine rounds, depending on the prediction of how many rounds will be necessary to eradicate all tumour cells. There are thus possibilities to improve patient care by finding the optimal number of treatment rounds.

2.4. MRI scans

It is crucial to know as soon as possible if NAT is effective against a tumour as untreated tumours can easily grow into sizes that are no longer suitable for surgery or other forms of treatment. Thus, if it turns out that the tumour does not respond well, it is possible to choose a different treatment strategy based on other components. To evaluate how well a tumour responds to therapy, medical imaging is used like MRI scans or ultrasound. Conventional MRI scans and ultrasounds can only provide information after the patient has received several treatment cycles, but as technology has evolved new types of MRI scans have been invented. *Diffusion-weighted MRI* (DW-MRI) and *dynamic contrast-enhanced MRI* (DCE-MRI) for example can give insights into tumour response after only one cycle of NAT and can thus be used to predict growth after multiple cycles of treatment [3]. DW-MRI measures the motion of water within tissue and is used to estimate the *apparent diffusion coefficient* (ADC) value that describes the rate of water diffusion in cellular tissue. Based on these ADC values, the number of tumour cells

for each position in the breast, which is needed for the models, can be estimated. In DCE-MRI a fast acquisition of images is made while a *contrast agent* (CA) is inserted into a vein of a patient. As the name suggests, a contrast agent is used to create more contrast between the different tissues on an MRI image and thus improves the quality of an MRI image [2]. This means that one DCE scan consists of multiple images that are made at different time points. The first images are called *pre-contrast* images, as they were made before the CA was used and the other images are called *post-contrast* images. Note that it depends on the MRI machine and the MRI protocol of the hospital, which dictates the different MRI settings, how many pre-contrast and post-contrast images should be made. In the models, DCE-MRI is used to detect a *region of interest* (ROI) that contains the tumour, determine certain parameter values and estimate the distribution of drugs in tumour tissue.

3

Mathematical Models

In this chapter, the mathematical model that used in this thesis are presented. Firstly, the Mechanically Coupled Reaction-Diffusion model is explained in Section 3.1. Secondly, the extended version of this model, called the Drug-Incorporated Mechanically Coupled Reaction-Diffusion model is explained in Section 3.2. Section 3.3 provides an overview of the variables and parameters, and Section 3.4 provides an overview of the models.

3.1. Mechanically Coupled Reaction-Diffusion Model

Much research has been done into modelling breast cancer tumours and their response to chemotherapy based on MRI images. In recent years, there has been more attention for patient-specific models that can make these predictions already after one round of chemotherapy. The tumour density was in most cases predicted with a classical reaction-diffusion model describing the proliferation (reaction) and movement (diffusion) of tumour cells. One of the restrictions of this approach is that tumour growth is only limited by the boundaries of the simulated domain while in practice the stiffness of the surrounding tissue plays an important role [17]. For this reason, researchers started looking into biomechanical models that take the surrounding tissue into account. In 2013, a paper was published that showed that the *Mechanically Coupled Reaction-Diffusion* (MCRD) model more accurately predicted the response of breast cancer tumours to chemotherapy than standard reaction-diffusion models [3]. In this paper, the available quantitative data from the newest imaging technologies (i.e. DCE-MRI and DW-MRI) was combined with a reaction-diffusion model that takes the mechanical properties of the different tissue types into account to predict the tumour density in every position of the breast. The mechanics were included by restricting the tumour cell diffusion in such a way that tissue with high stiffness (i.e. fibroglandular tissue) is less likely to be invaded by the tumour than tissue with low stiffness (i.e. adipose tissue). In this way, the growth patterns of tumours were more closely simulated compared to the standard models without restricted cell diffusion.

The first paper of this group of researchers compared 2D non-mechanical and mechanical models and showed that the latter models the response of a tumour to chemotherapy more accurately. In a second paper in which the MCRD model was applied to breast cancer patients, parameters which were previously taken from literature were estimated based on patient-specific data to predict pCR [5], and in a third paper the model was extended to 3D [6].

Let us now summarize the approach before presenting the model. Firstly, the DW- and DCE-MRI scans are pre-processed to derive the tumour densities and segment the tissue into adipose, fibroglandular and tumorous tissue. The tumour densities consist of the number of tumour cells for each voxel in the breast. Then, using the MRI scans from the first and second time points, denoted at t_0 and t_1, the model parameters are calibrated in such a way that there is an accurate prediction from the first to the second scan. Then the model is used to predict from t_1 to t_2, which is the time point of the last MRI scan. The modelled and measured tumour densities at t_2 are then compared to evaluate the results. More details on the modelling pipeline are given in Section 5.2.

The model is described by the following set of coupled partial differential equations:

$$\frac{\partial N(\overline{x},t)}{\partial t} = \nabla \cdot (D(\overline{x},t)\nabla N(\overline{x},t)) + k(\overline{x})N(\overline{x},t)\Big(1 - \frac{N(\overline{x},t)}{\theta}\Big) \tag{3.1}$$

$$D(\overline{x},t) = D_0 e^{-\gamma \sigma_{vm}(\overline{x},t)} \tag{3.2}$$

$$\nabla \cdot G\nabla\vec{u} + \nabla\Big(\frac{G}{1-2\nu}(\nabla \cdot \vec{u})\Big) - \lambda\nabla N(\overline{x},t) = 0 \tag{3.3}$$

In Equation 3.1 the spatiotemporal rate of change of the tumour cell number is described as the sum of the random tumour cell movement (diffusion, first term) and the logistic growth (reaction, second term). In the above formula, $N(\overline{x},t)$ is the estimated number of tumour cells of voxel $\overline{x}$ at time t, θ represents the maximum tumour density per voxel, which is often also referred to as the *carrying capacity* and $k(\overline{x})$ is the net tumour proliferation, which represents he difference between cell growth and cell death. Equation 3.1 is also used in the standard reaction-diffusion models, but the MCRD model is extended with Equations 3.2 and 3.3 to simulate the mechanical properties of the tissue.

Equation 3.2 defines the tumour cell diffusion term D, where σ_{vm} is the *von Mises stress* reflecting the interaction between the growing tumour and its environment, γ is a coupling constant for the von Mises stress, and D_0 is the diffusion when there is no external stress, so without mechanical restrictions. From this definition, it can be seen that as the local von Mises stress increases, there will be a decrease in tumour cell movement and the tumour cell diffusion coefficient D will be lower, thereby simulating the mechanical effect on the surrounding tissue. The von Mises stress σ_{vm} is calculated with the tissue displacement vector $\vec{u}$ caused by the growing tumour, which is found by solving Equation 3.3 for $\vec{u}$.

To obtain Equation 3.3, the mechanical equilibrium $\nabla \cdot \sigma_{vm}(\overline{x},t) - \lambda \cdot \nabla N(\overline{x},t) = 0$ is rewritten in terms of the displacement vector $\vec{u}$. This step is made under the assumption that breast tissue is linear elastic isotropic. Equation 3.3 thus describes a so-called *linear elastic isotropic mechanical equilibrium*, on which an external force is acting depending on a coupling constant λ and the change in tumour cell number $N(\overline{x},t)$. The first two terms of Equation 3.3 represent the linear-elastic description of tissue displacement and the third term represents the local body force generated by the invading tumour [17]. It thus governs the response of the displacement vector $\vec{u}$ to the tumour cell growth.
In the equation, $G = \frac{E}{2(1+\nu)}$ represents the shear modulus, which is an intrinsic mechanical property of breast and tumour tissue, and E and ν are material properties of *Young's modulus* and *Poisson's ratio* respectively. Young's modulus is the elasticity modulus measuring the stiffness of a material under a lengthwise force. It corresponds to the ratio between stress and strain. Stress is a quantity that describes the distribution of internal forces within an object and is often denoted by σ. Normal stress is stress under a force that is perpendicular to the surface and shear stress is stress under a force that is parallel to the surface. Strain, on the other hand, is a quantity that describes the deformations that occur within a body, denoted by ϵ. Poisson's ratio measures the Poisson effect that occurs when a force is applied and the material deforms in perpendicular direction to the force. These two ratios determine the deformation of the material and are used in a deformation matrix that is used to calculate the von Mises stress. For this, Hooke's Law will be applied, which states that stress is the product of Young's modulus and strain.
After solving Equation 3.3 for $\vec{u} = (u,v,w)$ where u,v,w are the local deformations in $x-, y-$, and $z-$direction, the normal strains $(\epsilon_{xx}, \epsilon_{yy}, \epsilon_{zz})$ and shear strains $(\epsilon_{xy}, \epsilon_{xz}, \epsilon_{yz})$ are calculated. As only small deformations occur, ϵ_{ij} can be calculated as the change in length in direction i divided by the original length in direction j, as given in Equation 3.4. Note that three-dimensional notation is used here, but this can be simplified to the two-dimensional case by only considering plane stress [11].

$$\begin{pmatrix} \epsilon_{xx} \\ \epsilon_{yy} \\ \epsilon_{zz} \\ \epsilon_{xy} \\ \epsilon_{xz} \\ \epsilon_{yz} \end{pmatrix} = \begin{pmatrix} \partial u/\partial x \\ \partial v/\partial y \\ \partial w/\partial z \\ \partial u/\partial y \\ \partial u/\partial z \\ \partial v/\partial z \end{pmatrix} \tag{3.4}$$

Now Hooke's law for linear isotropic materials is applied to calculate the normal and shear stresses.

$$\begin{pmatrix}\sigma_{xx}\\ \sigma_{yy}\\ \sigma_{zz}\\ \sigma_{xy}\\ \sigma_{xz}\\ \sigma_{yz}\end{pmatrix} = \frac{2G}{1-2\nu}\begin{bmatrix}1-\nu & \nu & \nu & 0 & 0 & 0\\ \nu & 1-\nu & \nu & 0 & 0 & 0\\ \nu & \nu & 1-\nu & 0 & 0 & 0\\ 0 & 0 & 0 & 1-2\nu & 0 & 0\\ 0 & 0 & 0 & 0 & 1-2\nu & 0\\ 0 & 0 & 0 & 0 & 0 & 1-2\nu\end{bmatrix}\begin{pmatrix}\epsilon_{xx}\\ \epsilon_{yy}\\ \epsilon_{zz}\\ \epsilon_{xy}\\ \epsilon_{xz}\\ \epsilon_{yz}\end{pmatrix}$$

Finally, the normal and shear stresses are used to calculate the von Mises stress for each voxel.

$$\sigma_{vm} = \left[\frac{1}{2}\left((\sigma_{xx}-\sigma_{yy})^2 + (\sigma_{xx}-\sigma_{zz})^2 + (\sigma_{zz}-\sigma_{yy})^2 + 6(\sigma_{xy}^2+\sigma_{xz}^2+\sigma_{yz}^2)\right)\right]^{\frac{1}{2}}$$

For the forward prediction the following steps are taken:

1. Calculate $\nabla N(\overline{x},t)$
2. Solve Equation 3.3 for $\vec{u}$
3. Calculate $\sigma_{vm}(\overline{x},t)$
4. Update $D(\overline{x},t)$ with Equation 3.2
5. Calculate $N(\overline{x},t+\Delta t)$ with Equation 3.1

These steps are also displayed in Figure 3.1.

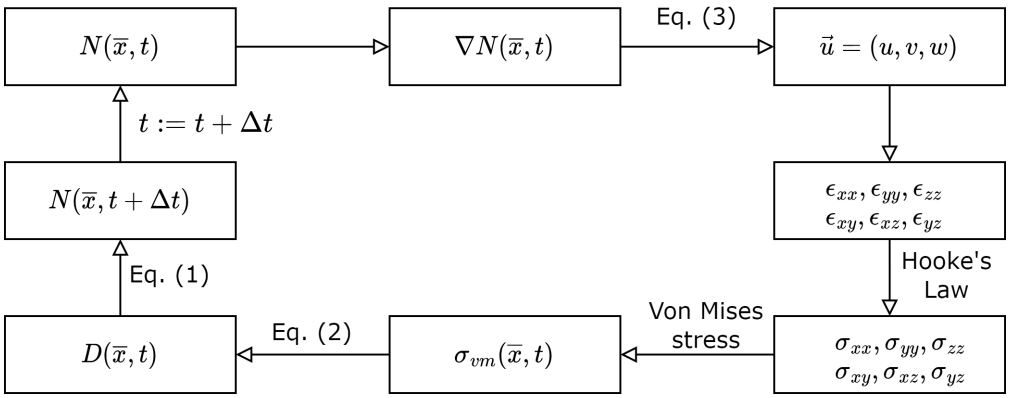

Figure 3.1: Schematic drawing of the steps taken in one time iteration for the MCRD model.

In this thesis, we will refer to Equation 3.1 as the *first* or *reaction-diffusion* equation, Equation 3.2 will be called the *second* or *diffusion coefficient* equation and Equation 3.3 will be indicated as the *third* or *linear-elastic* equation.

3.2. Drug-Incorporated Mechanically Coupled Reaction-Diffusion Model

One of the main limitations of the MCRD model is that it assumes constant proliferation of the tumour cells, implying NAT to have an unrealistic linear effect [3, 5, 6]. In 2018, a paper on an extension to the MCRD model was published, which performed better at predicting the tumour cell density at the conclusion of treatment [7]. In a subsequent paper, different treatment strategies were modelled and compared [8]. This model, which was referred to as the *Drug incorporated Mechanically Coupled Reaction-Diffusion* (DIMCRD) model, takes a non-uniform distribution of drugs into account by adding an explicit death term in the form of a spatiotemporal $C_{tissue}^{drug}(\overline{x},t)$ term combined with a calibrated

efficacy term α to the reaction-diffusion equation. This results in the system of equations given in below.

$$\frac{\partial N(\overline{x},t)}{\partial t} = \nabla \cdot (D\nabla N(\overline{x},t)) + k(\overline{x})N(\overline{x},t)\Big(1 - \frac{N(\overline{x},t)}{\theta}\Big) - \alpha C^{drug}_{tissue}(\overline{x},t) \tag{3.5}$$

$$D = D_0 e^{-\gamma \sigma_{vm}(\overline{x},t)} \tag{3.6}$$

$$\nabla \cdot G\nabla\vec{u} + \nabla\Big(\frac{G}{1-2\nu}(\nabla \cdot \vec{u})\Big) + \lambda\nabla N(\overline{x},t) = 0 \tag{3.7}$$

The $C^{drug}_{tissue}(\overline{x},t)$ represents the drug concentration in position $\overline{x}$ at time t, which can be calculated in various ways based on the DCE-MRI scans. In the first paper of 2018, the extended *Kety-Tofts* (KT) model was used. This is a pharmacokinetic model that describes the change in drug concentration between the tissue and blood plasma spaces, which is why it is called a two-compartment model. It is a model that is widely used in papers regarding cancer modelling for estimating physiological parameters describing the perfusion and permeability, analysing the vasculature and estimating drug concentrations in tissue [2, 4, 18–22]. For this model, the assumption is made that chemotherapy spreads out in the same way as the contrast agent that was used for the DCE-MRI scans.

In Figure 3.2 a schematic drawing is given for the Kety-Tofts model, where Gd represents the gadolinium that is part of the contrast agent and $k_{ep} = \frac{K_{trans}}{v_e}$ is the reflux rate of the gadolinium. $K^{trans}(\overline{x})$ is the volume transfer constant that represents the transport rate of the gadolinium from the blood plasma to the tissue extravascular extracellular space, which is the space between the tissue cells and the blood vessel. The volume fraction of this extravascular-extracellular space is given by $v_e(\overline{x})$ and the volume fraction of the plasma space is given by $v_p(\overline{x})$.

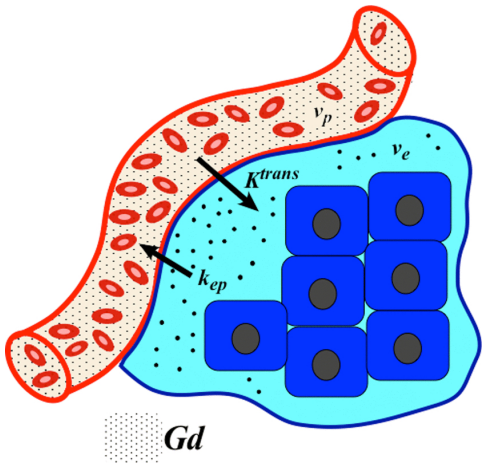

Figure 3.2: Schematic drawing of the Kety-Tofts model [23].

By assuming that the behaviour of the drugs are comparable to the behaviour of the contrast agent, the concentration of drug in the tissue at location $\overline{x}$ at time t can be calculated with Equation 3.8, where $C^{drug}_{plasma}(t)$ is defined as the concentration of drug in the plasma at time t, which is a literature-based function for the drug that is considered.

$$C^{drug}_{tissue}(\overline{x},t) = K^{trans}(\overline{x}) \int_0^t \Big(C^{drug}_{plasma}(s) \cdot \exp\big(-\frac{K^{trans}(\overline{x})}{v_e(\overline{x})}(t-s)\big)\Big)ds + v_p(\overline{x})C^{drug}_{plasma}(t) \tag{3.8}$$

The values of $K^{trans}(\overline{x}), v_e(\overline{x})$ and $v_p(\overline{x})$ are found based on the DCE data, for which more details will be given in Section 6.1. For the standard Kety-Tofts model, which is also described in various literature, $v_p(\overline{x})$ is put to zero, so the second term in Equation 3.8 turns zero and only the integral remains.

In a subsequent on the DIMCRD model, a so-called *Normalised Blood Volume Map* (NBVM) is scaled by the peak concentration of drug to estimate the drug distribution in each position of the breast, where the peak concentration is calculated with the standard Kety-Tofts model [8]. Another paper on the DIMCRD model, also published in 2020, only uses the NBVM and does not use Kety-Tofts [9]. This NBVM is calculated based on the DCE data by subtracting the average pre-contrast signal from the post-contrast values for each voxel, calculating the *area under the curve* (AUC) of these baseline-subtracted signal curves and then normalising by the maximum AUC value found within the tumour. More details on these steps are provided in Section 6.2. Once the NBVM is calculated, which is denoted by $C_{tissue}^{drug}(\overline{x}, t^*)$, where t^* refers to the time of treatment, it is multiplied with an exponential decay term to simulate the washout of the drug after each dose. Thus, based on the NBVM, $C_{tissue}^{drug}(\overline{x}, t)$ can be calculated with the formula in Equation 3.9, where β describes the decay of the drug.

$$C_{tissue}^{drug}(\overline{x}, t) = C_{tissue}^{drug}(\overline{x}, t^*)e^{-\beta(t-t^*)} \tag{3.9}$$

3.3. Overview of variables and parameters

The two tables below contain all the previously mentioned variables and parameters and their units.

Variable	Description
$N(\overline{x}, t)$	Number of tumour cells in the voxel at position $\overline{x}$ at time t
$D(\overline{x}, t)$	Diffusion coefficient of tumour cells (mm^2/day)
σ_{vm}	von Mises stress (kPa)
G	Shear modulus due to breast tissue properties (kPa)
$\vec{u}$	Displacement vector due to tumour growth (mm)
$C_{tissue}^{drug}(\overline{x}, t)$	Concentration of drugs in tissue in voxel at position $\overline{x}$ at time t (μM)
$C_{plasma}^{drug}(t)$	Concentration of drugs in plasma at time t (μM)

Table 3.1: Variables and their descriptions

Parameter	Description
$k(\overline{x})$	Proliferation rate of tumour cells per voxel (1/day)
θ	Carrying capacity
D_0	Diffusion coefficient without stress (mm^2/day)
γ	Coupling constant for von Mises stress (1/kPa)
E	Material property of Young's Modulus (kPa)
ν	Material property of Poisson ratio
λ	Coupling constant for displacement vector
α	Efficacy of the drug against tumour cells ($1/(\mu M \cdot$ day))
$K^{trans}(\overline{x})$	Volume transfer constant from plasma to tissue space (1/day)
$v_e(\overline{x})$	Volume fraction of extravascular extracellular space
$v_p(\overline{x})$	Volume fraction of plasma space
β	Drug decay rate (1/day)

Table 3.2: Parameters and their descriptions

3.4. Model overview

In this thesis, various models will be compared. For clarity, the modelling equations and the abbreviations for these models are repeated below.

- Reaction-Diffusion model (RD):

$$\frac{\partial N(\overline{x}, t)}{\partial t} = \nabla \cdot (D \nabla N(\overline{x}, t)) + k(\overline{x}) N(\overline{x}, t)\Big(1 - \frac{N(\overline{x}, t)}{\theta}\Big)$$

- Mechanically Coupled Reaction-Diffusion model (MCRD):

$$\frac{\partial N(\overline{x},t)}{\partial t} = \nabla \cdot (D\nabla N(\overline{x},t)) + k(\overline{x})N(\overline{x},t)\left(1 - \frac{N(\overline{x},t)}{\theta}\right)$$

$$D = D_0 e^{-\gamma \sigma_{vm}(\overline{x},t)}$$

$$\nabla \cdot G\nabla\vec{u} + \nabla\left(\frac{G}{1-2\nu}(\nabla \cdot \vec{u})\right) + \lambda\nabla N(\overline{x},t) = 0$$

- Drug Incorporated Reaction-Diffusion model (DIRD):

$$\frac{\partial N(\overline{x},t)}{\partial t} = \nabla \cdot (D\nabla N(\overline{x},t)) + k(\overline{x})N(\overline{x},t)\left(1 - \frac{N(\overline{x},t)}{\theta}\right) - \alpha C_{tissue}^{drug}(\overline{x},t)N(\overline{x},t)$$

- Drug Incorporated Mechanically Coupled Reaction-Diffusion model (DIMCRD):

$$\frac{\partial N(\overline{x},t)}{\partial t} = \nabla \cdot (D\nabla N(\overline{x},t)) + k(\overline{x})N(\overline{x},t)\left(1 - \frac{N(\overline{x},t)}{\theta}\right) - \alpha C_{tissue}^{drug}(\overline{x},t)N(\overline{x},t)$$

$$D = D_0 e^{-\gamma \sigma_{vm}(\overline{x},t)}$$

$$\nabla \cdot G\nabla\vec{u} + \nabla\left(\frac{G}{1-2\nu}(\nabla \cdot \vec{u})\right) + \lambda\nabla N(\overline{x},t) = 0$$

4

Research questions and methodology

In this chapter, the research plan for this thesis is established. For this, firstly the research question and the accompanying sub-questions are formulated. Next, the steps that are taken to answer these questions are summarised.

4.1. Research Questions

As stated in Section 1.3, the research question of this thesis is:

How can the MCRD model be improved to achieve better results in modelling chemotherapy and the growth of tumours to determine the correct number of treatment rounds in HER2+ breast cancer patients?

To answer the research question, several sub-questions will be formulated. However, before we do this, we first make some remarks on what was found in the research by Oudhof, in which the MCRD model was used to model the tumour growth for HER2+ patients in a similar way to the method explained in the literature [3, 5, 6]. One of the things that were found in that thesis was that in the calibration phase the number of parameters was higher than the number of data points. The papers do not elaborate on how this is solved, and in the solution of Oudhof a Tikhonov regularisation term was used to overcome the problem, but the value that was given to this regularisation term turned out to have a big influence on the results. For that reason, we want to investigate how we can reduce the number of parameters, as for the DIMCRD model there is at least one additional parameter. Furthermore, an important recommendation from her research was to include the treatment schedule of the patients to calculate a chemotherapy term for the reaction-diffusion equation. This was motivated by the fact that in the MCRD model there is a proliferation term that represents both cell growth and cell death which is constant in time and therefore is not realistic. Another limitation of the implementation was that one slice of the MRI scan was used because the model was only implemented in 2D, which meant that it was not possible to include the entire tumour in the model. With this information, the following sub-questions are posed for this thesis:

1. How can the number of parameters be reduced for the calibration?
2. How should the chemotherapy term be calculated based on the treatment data and MRI scans of patients?
3. How can the model be extended from 2D to 3D?
4. How accurate are the predictions of the model?

4.2. Methodology

4.2.1. Data

The dataset of this thesis consists of DCE- and DW-MRI scans before (t_0), during (t_1) and after treatment (t_2) of three HER2+ patients that were treated at EMC. These MRI scans have already been

pre-processed by Oudhof and we are thus already provided with the tumour densities at these time points and the segmentation of adipose, fibroglandular and tumorous tissue. In addition to this data, we are provided with the metadata of the scans, including the dates of the scans and the acquisition parameters, and the dates, components and dosages of treatment that were given to these patients. More information on the data can be found in Section 5.1.

4.2.2. Calibration

As the data is already pre-processed, we can immediately move on to the calibration phase, in which the parameters are tweaked using a non-linear least squares algorithm to minimise the error between the modelled tumour density at t_1 and the measured tumour density at that time point. For the spatial discretisations finite difference discretisations will be used and for the time integration, Forward Euler will be used. For solving the linear elastic equation a direct solver that was already implemented by Oudhof is used. In the calibration for the RD and MCRD models, the proliferation rate k is determined for each voxel and D_0 is determined as a global parameter. For the DIRD and DIMCRD models, an additional global parameter α needs to be fitted. This means that for all cases there are more parameters than data points. For this reason, we will create a mask such that this proliferation rate is no longer determined for each voxel, which will decrease both the number of parameters that need to be estimated and the computation time. In addition, we will look into using another non-linear least square algorithm with which we can provide bounds on the parameters to prevent unwanted negative values on some parameters.

4.2.3. Chemotherapy extension

To incorporate the treatment schedule of the patients, we need to calculate the $C_{tissue}^{drug}(\overline{x}, t)$ for the DIRD and DIMCRD model. For this, we will use the standard Kety-Tofts model and the Normalised Blood Volume Map that were introduced in Section 3.2. We will evaluate and compare these methods and decide which one is best to use for our dataset. Once this choice is made, we will make a thorough model analysis to investigate the influence of the parameters and the effect of certain choices. We will also compare the results of the different models to see if this addition has improved the predictions.

4.2.4. Three-dimensional extension

To extend the model to three dimensions, the discretisations have to be slightly adjusted and the implementation should be updated accordingly. Here, we expect difficulty regarding the computational complexity of the model, so we will look at different options to decrease the number of computations or speedup the computations. Hence, several choices have to be made regarding the number of slices that are considered and whether each slice should be downsampled or not. These will also be evaluated and we will evaluate whether this extension has improved the results compared to the two-dimensional implementation.

5 Implementation

In this chapter, information is given on the implementation of the models. Firstly, details are provided on the data for this thesis in Section 5.1. Next, the modelling pipeline is presented in Section 5.2, which provides an overview of all the steps that have to be taken to get to a model prediction. In Section 5.3, the discretisations for the modelling equations are worked out, which are needed to make predictions with the model based on the tumour densities that are calculated based on the MRI scans. Lastly, Section 5.4 improvements that were made for the calibration phase are explained.

5.1. Data

For this thesis, three patients that are HER2+, were treated at Erasmus MC and had three MRI scans, have been selected by dr A. Jager, who is the involved internist-oncologist from EMC. We will refer to these patients are p_1, p_2 and p_3 as all data has been anonymized. Note that a fourth patient was also included in the previous research [11], but it turned out that the data for this patient was not suitable: the tumour had a strange shape and the dimensions of all scans were different, making the pre-processing harder.

All three patients did not achieve pCR after their treatment, meaning that tumour cells were still visible on the third MRI scan. Both p_1 and p_2 had multiple tumours, of which the biggest one is chosen and selected for the model as the other tumours were no longer visible on the scan at t_2. The tumour of p_3 was oddly shaped and did not shrink centrally.

Table 5.1 provides information on the MRI acquisition parameters that were used for the scans at EMC. This info was retrieved from either the metadata or the MRI imaging protocol of EMC. All scans were made with a magnetic field strength of 1.5T and for the DCE images 8 scans were made: 2 pre-contrast and 6 post-contrast, where 15 mL ProHance was used as a gadolinium-based contrast agent. Approximately every 70 seconds a scan was made. The first scan of p_2 has been made at a different hospital and thus acquisition parameters are different from the ones of EMC. The corresponding acquisition parameters can be found in Appendix A.1. The information on the type of scan sequence, repetition time, echo time and flip angle will be used in Chapter 6to calculate the concentration of chemotherapy based on the DCE scans. The size of the voxels and the acquisition matrix are important for the pre-processing steps.

	DW-MRI	DCE-MRI
Scan sequence	Spin Echo	Vibrant
Repetition time (ms)	5468	4.724
Echo time (ms)	68.6	2.208
Flip angle (degrees)	90	10
Voxel dimension (mm)	1.4 × 1.4	0.66 × 0.66
Acquisition matrix	256 ×256	512 × 512

Table 5.1: MRI acquisition parameters

In Table 5.2 the voxel length and the number of slices in z-dimension are stated. It can be seen that these numbers vary quite a lot between the different scans and patients, especially for the DCE scans, which is why they have been summarised below. This information is important for the pre-processing and the three-dimensional implementation of the model. After pre-processing, the tumour densities for p_1 and p_3 are represented by arrays of size $(180, 180, 120)$, for p_2 this is an array of size $(210, 210, 86)$. Each of the 120 or 86 slices is then downsampled by a factor three. At each time point, the slice with the highest number of tumour cells is chosen as measured data for the two-dimensional model.

		DW			DCE		
		t_0	t_1	t_2	t_0	t_1	t_2
Voxel length (mm)	p_1	6.5	6.5	6.5	1.6	1.6	2.2
	p_2	4.8	6.5	6.5	0.9	2.2	2.2
	p_3	6.5	6.5	6.5	1.6	1.6	2.2
Number of slices	p_1	32	32	32	120	120	86
	p_2	34	32	32	160	86	86
	p_3	32	32	32	120	120	86

Table 5.2: Length of the voxel in z-direction and the number of slices in z-direction for all patients and scans.

All patients have been treated with the same type of treatment schedule consisting of paclitaxel, carboplatin, trastuzumab and pertuzumab. As explained in Section 2.3, pertuzumab and trastuzumab are immunotherapy often used in the treatment of HER2+ patients, and carboplatin and paclitaxel are chemotherapy medications that are used to treat various forms of cancer. For p_1, Figure 5.1 displays the treatment schedule. It can be seen that every three weeks a mix of all four drugs is given. After the first week, additional paclitaxel is given, which is followed by a week of no drugs. Note that the amount of administered drugs in each mix varies and that the final treatment was given after the last MRI scan. The treatment schedule for the other patients is similar.

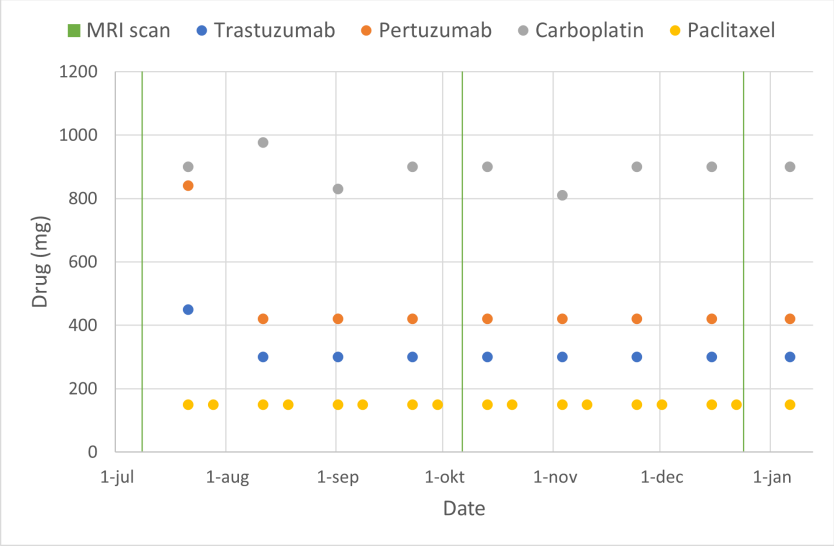

Figure 5.1: Treatment schedule for p_1. The dates of the MRI scans are shown by vertical lines in green.

5.2. Modelling pipeline

To give an overview of all the steps that are taken to get from MRI scans and a treatment schedule to a model prediction, a modelling pipeline has been formulated. It is described below and illustrated in Figure 5.2.

- **Registration**: Using both rigid and non-rigid registration, the images from different sessions are aligned to correct for body movements.

- **Tissue segmentation**: With the help of a radiologist, the tumour is segmented from the surrounding tissue. Next, global histogram equalization is used to distinguish between fibroglandular and adipose tissue.
- **Calculating tumour densities**: The tumour segmentation and calculated ADC values are combined to determine the tumour densities, denoted by $\hat{N}(\overline{x}, t_0), \hat{N}(\overline{x}, t_1)$ and $\hat{N}(\overline{x}, t_2)$, for the three time points t_0, t_1 and t_2.
- **Calculating chemotherapy concentrations**: The concentration of drug at each time t and in each voxel $\overline{x}$ is calculated using the DCE scans and the treatment schedule
- **Calibration**: Based on initial guesses, the optimal value for the patient-specific parameters $k(\overline{x}), D_0$ and α are determined by running the model forward in time from t_0 to t_1 and comparing the estimated tumour density $N(\overline{x}, t_1)$ with the actual tumour density $\hat{N}(\overline{x}, t_1)$.
- **Evaluation**: The model is run from t_1 to t_2, yielding $N(\overline{x}, t_2)$ which is compared to $\hat{N}(\overline{x}, t_2)$ to evaluate the results.

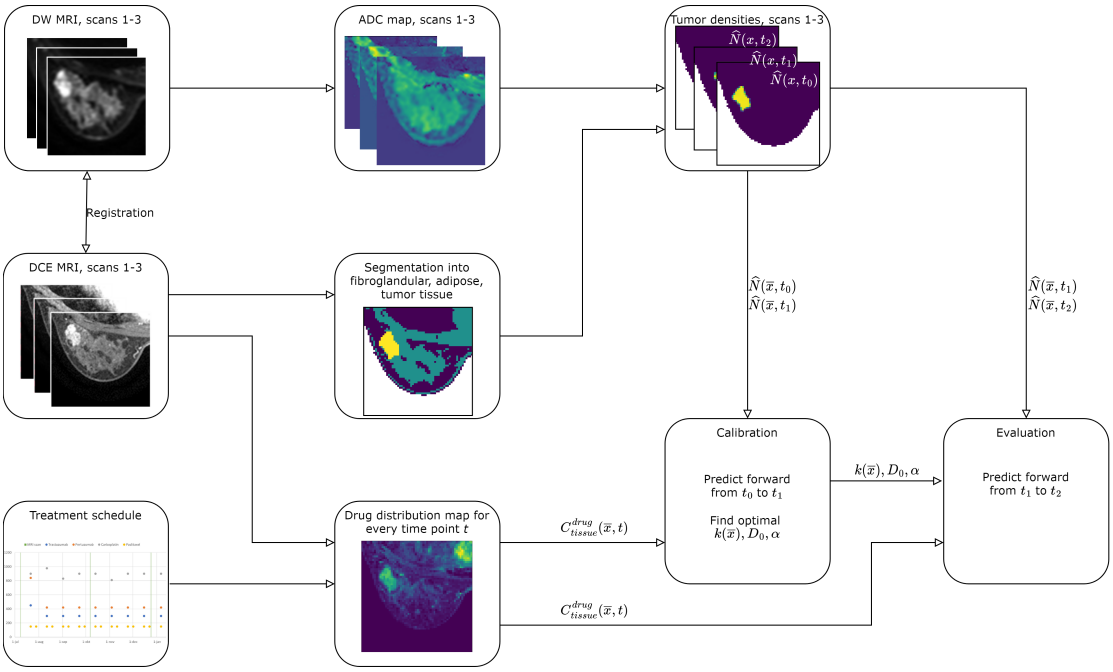

Figure 5.2: Modelling pipeline

The pre-processing steps consist of registration, tissue segmentation and calculating the tumour densities. More information on these pre-processing steps is given in Appendix A.2 and in the work of Oudhof [11]. As the data has already been pre-processed, this work is based on the calculated tumour densities and tissue segmentation, which are shown for p_1 in Figure 5.3 below.

5.3. Discretisations

For the forward calculations in time in the calibration and evaluation phases, spatial and temporal discretisations will be used to approximate the continuous variables. In this section, the discretisations for the modelling equations are worked out. In the literature, different methods are used: some papers use the *Finite Difference Method* (FDM) for the spatial discretisation [7–9, 14, 24] but a few others use the *Finite Element Method* (FEM) [3, 5, 6] which is more complex. In this thesis, the Finite Difference Method as described in Vuik et al. (2016), Chapter 7 and van Kan et al. (2014) Chapter 3 is applied [25, 26]. This is a technique that uses finite differences to approximate derivatives to solve differential equations. The discretisations in this chapter are given in two dimensions but they can easily be extended to three dimensions.

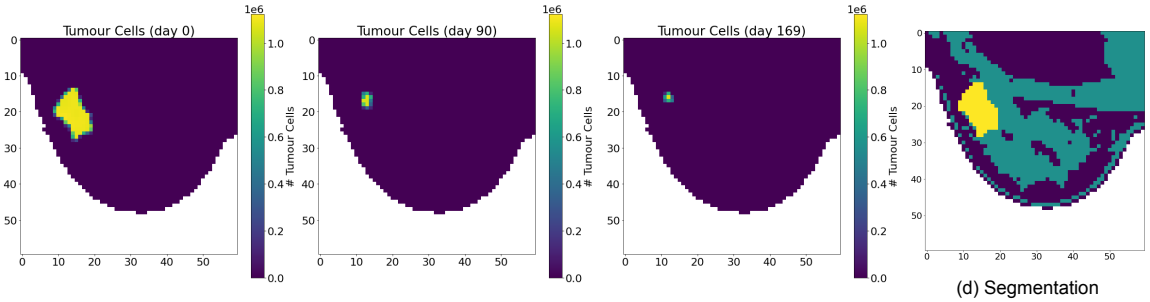

(a) $\hat{N}(\overline{x}, t_0)$ (b) $\hat{N}(\overline{x}, t_1)$ (c) $\hat{N}(\overline{x}, t_2)$ (d) Segmentation

Figure 5.3: Tumour densities and segmentation for p_1. The left three images show the measured tumour densities for p_1 on t_0, t_1 and t_2 from left to right. The right image shows the segmentation, where the tumour is displayed in yellow, the fibroglandular tissue in green and the adipose tissue in purple.

5.3.1. Reaction-Diffusion equation

Spatial discretisation

As a first step for the spatial discretisation of Equation 3.5, the right-hand side is rewritten, where for simplicity $C = C_{tissue}^{drug}$ denotes the concentration of drug in the tissue.

$$\nabla \cdot (D\nabla N) + kN\Big(1 - \frac{N}{\theta}\Big) - \alpha CN = \frac{\partial}{\partial x}\Big(D\frac{\partial N}{\partial x}\Big) + \frac{\partial}{\partial y}\Big(D\frac{\partial N}{\partial y}\Big) + kN\Big(1 - \frac{N}{\theta}\Big) - \alpha CN$$

For the discretisation, the centres of the pixels of the MRI images are taken as grid points, so a cell-centred approach is used to form a $n_x \times n_y$ grid. These grid points make up the mathematical domain which is considered two-dimensional for now. For notation, let us introduce $N_{i,j} = N(x_i, y_j)$ which is the tumour density in point (x_i, y_j). In a similar way $D_{i,j}, k_{i,j}$ and $C_{i,j}$ are defined.

Next, the partial derivatives are discretised using repeated central differences. For this, we write $M(x,y) = D(x,y)\frac{\partial N(x,y)}{\partial x}$ and apply central difference for $M_{i,j}$ using midpoints $x_{i-\frac{1}{2}}$ and $x_{i+\frac{1}{2}}$. This yields

$$\frac{\partial M_{i,j}}{\partial x} = \frac{M_{i+\frac{1}{2},j} - M_{i-\frac{1}{2},j}}{\Delta x} + \mathcal{O}(\Delta x^2).$$

Replacing $M_{i,j}$ by $D_{i,j}\frac{\partial N_{i,j}}{\partial x}$ thus gives the following result:

$$\frac{\partial}{\partial x}\Big(D_{i,j}\frac{\partial N_{i,j}}{\partial x}\Big) = \frac{D_{i+\frac{1}{2},j}\frac{\partial N_{i+\frac{1}{2},j}}{\partial x} - D_{i-\frac{1}{2},j}\frac{\partial N_{i-\frac{1}{2},j}}{\partial x}}{\Delta x} + \mathcal{O}(\Delta x^2).$$

The case of $\frac{\partial}{\partial y}(D_{i,j}\frac{\partial N_{i,j}}{\partial y})$ is similar. Using this information and truncating the partial derivatives yields the discretisation of Equation 3.5.

$$\frac{\partial N_{i,j}}{\partial t} = \frac{D_{i+\frac{1}{2},j}\frac{\partial N_{i+\frac{1}{2},j}}{\partial x} - D_{i-\frac{1}{2},j}\frac{\partial N_{i-\frac{1}{2},j}}{\partial x}}{\Delta x} + \frac{D_{i,j+\frac{1}{2}}\frac{\partial N_{i,j+\frac{1}{2}}}{\partial y} - D_{i,j-\frac{1}{2}}\frac{\partial N_{i,j-\frac{1}{2}}}{\partial y}}{\Delta y} + k_{i,j}N_{i,j}\Big(1 - \frac{N_{i,j}}{\theta}\Big) - \alpha C_{i,j}N_{i,j} \quad (5.1)$$

In the next step, central differences are again applied for the partial derivatives that are still present in Equation 5.1 and the values for the diffusion coefficient are approximated using the known values in the grid points.

$$\frac{\partial N_{i+\frac{1}{2},j}}{\partial x} = \frac{N_{i+1,j} - N_{i,j}}{\Delta x} + \mathcal{O}(\Delta x^2) \qquad D_{i+\frac{1}{2},j} \approx \frac{D_{i+1,j} + D_{i,j}}{2}$$
$$\frac{\partial N_{i-\frac{1}{2},j}}{\partial x} = \frac{N_{i,j} - N_{i-1,j}}{\Delta x} + \mathcal{O}(\Delta x^2) \qquad D_{i-\frac{1}{2},j} \approx \frac{D_{i,j} + D_{i-1,j}}{2}$$
$$\frac{\partial N_{i,j+\frac{1}{2}}}{\partial y} = \frac{N_{i,j+1} - N_{i,j}}{\Delta y} + \mathcal{O}(\Delta y^2) \qquad D_{i,j+\frac{1}{2}} \approx \frac{D_{i,j+1} + D_{i,j}}{2}$$
$$\frac{\partial N_{i,j-\frac{1}{2}}}{\partial y} = \frac{N_{i,j} - N_{i,j-1}}{\Delta y} + \mathcal{O}(\Delta y^2) \qquad D_{i,j-\frac{1}{2}} \approx \frac{D_{i,j} + D_{i,j-1}}{2}$$

Finally, using all of the above information, it can be seen that the discretised form of Equation 3.5 can be written in the form $\frac{\partial \mathbf{N}}{\partial t} = A\mathbf{N} + f(\mathbf{N})$, where A consists of the coefficients and $f(N_{i,j}) = k_{i,j}N_{i,j}\left(1 - \frac{N_{i,j}}{\theta}\right) - \alpha C_{i,j}N_{i.j}$. For this matrix-vector notation, it is necessary to introduce a global ordering of the nodes. This is done by assigning to node (i,j) the global index $I = i + j \cdot n_x$. Homogeneous Neumann boundary conditions are imposed for both the boundary of the breast and the boundaries of the grid, meaning there is no diffusive flux of tumour cells on the boundaries. This was also done in the literature [3, 7–9, 11], but it should be noted that this assumes that the tumour cells do not invade the chest wall.

Time discretisation

Most of the papers based on some version of MCRD use a fully explicit method for the time integration [3, 6, 9, 14, 24, 27]. This explicit method, which is often also called the *Forward Euler Method*, uses the so-called *left rectangle* rule for approximation of the integral. For a non-linear equation $\frac{\partial \mathbf{N}}{\partial t} = A\mathbf{N} + f(\mathbf{N})$ this leads to Equation 5.2, where the time domain is discretised into $m = 0, \ldots, n_t$ and thus $\mathbf{N}^0 = \mathbf{N}(t_0)$.

$$\mathbf{N}^{m+1} = \mathbf{N}^m + \Delta t\left(A\mathbf{N}^m + f(\mathbf{N}^m)\right) \tag{5.2}$$

For the reaction-diffusion equation, this leads to Equation 5.3.

$$\begin{aligned} N_{i,j}^{m+1} = N_{i,j}^m + \Delta t\Bigg(& \frac{1}{2\Delta x^2}\Big(\big(D_{i,j} + D_{i-1,j}\big)N_{i-1,j}^m - \big(D_{i-1,j} + 2D_{i,j} + D_{i+1,j}\big)N_{i,j}^m + \big(D_{i,j} + D_{i+1,j}\big)N_{i+1,j}^m\Big) \\ & + \frac{1}{2\Delta y^2}\Big(\big(D_{i,j} + D_{i,j-1}\big)N_{i,j-1}^m - \big(D_{i,j-1} + 2D_{i,j} + D_{i,j+1}\big)N_{i,j}^m + \big(D_{i,j} + D_{i,j+1}\big)N_{i,j+1}^m\Big) \\ & + k_{i,j}N_{i,j}^m\Big(1 - \frac{N_{i,j}^m}{\theta}\Big) - \alpha C_{i,j}^m N_{i.j}^m\Bigg) \end{aligned} \tag{5.3}$$

The main advantage of this method is that it is fully explicit: the values of the next time step can easily be calculated without solving a big system of equations, which is usually the case for implicit methods. The downside however is that this is a first-order approximation, meaning that the local truncation error is of order Δt. The local truncation error is the new error that is made in each time step. In addition, it is conditionally stable, meaning that this method is only stable for certain values of Δt [25]. Because this restriction leads to a small time step, n_t will be big, so many computations are needed to predict the model forwards in time. For the reaction-diffusion equation that is used in this thesis, the stability criterion is given by Equation 5.4. The derivation for this bound is given in Appendix A.3.

$$\Delta t \leq \frac{2}{4D_{\max}\left(\frac{1}{\Delta x^2} + \frac{1}{\Delta y^2}\right) + |k|_{\max} + \alpha C_{\max}} \tag{5.4}$$

Note that this bound depends on the calibrated parameters, but for the calibration a time step Δt should be defined. Therefore, in the simulations by default $\Delta t = 0.5$ is chosen, which means that one time

step covers half a day. Then, after calibration, it is checked with the parameters if this Δt satisfies the bound that was calculated. In most cases it does, but when it does not, Δt is halved and calibration is run again, after which the bound is checked again. In this way, it is ensured that there is numerical stability.

5.3.2. Linear-Elastic equation

Now let us consider Equation 3.7, which we first rewrite by working out the inner products and vector notations. Note that we write $\vec{u} = (u, v)$, so u refers to the first component of $\vec{u}$ and v refers to the second component.

$$\frac{\partial}{\partial x}\Big(G\frac{\partial u}{\partial x}\Big) + \frac{\partial}{\partial y}\Big(G\frac{\partial u}{\partial y}\Big) + \frac{1}{1-2\nu}\frac{\partial}{\partial x}\Big(G\big(\frac{\partial u}{\partial x} + \frac{\partial v}{\partial y}\big)\Big) - \lambda\frac{\partial N}{\partial x} = 0 \tag{5.5}$$

$$\frac{\partial}{\partial x}\Big(G\frac{\partial v}{\partial x}\Big) + \frac{\partial}{\partial y}\Big(G\frac{\partial v}{\partial y}\Big) + \frac{1}{1-2\nu}\frac{\partial}{\partial y}\Big(G\big(\frac{\partial u}{\partial x} + \frac{\partial v}{\partial y}\big)\Big) - \lambda\frac{\partial N}{\partial y} = 0 \tag{5.6}$$

We now again discretise and use repeated central differences to approximate the partial derivatives.

$$\begin{aligned}&\frac{G_{i+\frac{1}{2},j}\dfrac{\partial u_{i+\frac{1}{2},j}}{\partial x} - G_{i-\frac{1}{2},j}\dfrac{\partial u_{i-\frac{1}{2},j}}{\partial x}}{\Delta x} + \frac{G_{i,j+\frac{1}{2}}\dfrac{\partial u_{i,j+\frac{1}{2}}}{\partial y} - G_{i,j-\frac{1}{2}}\dfrac{\partial u_{i,j-\frac{1}{2}}}{\partial y}}{\Delta y}\\ &+ \frac{1}{1-2\nu}\frac{G_{i+\frac{1}{2},j}\dfrac{\partial u_{i+\frac{1}{2},j}}{\partial x} - G_{i-\frac{1}{2},j}\dfrac{\partial u_{i-\frac{1}{2},j}}{\partial x} + G_{i+\frac{1}{2},j}\dfrac{\partial v_{i+\frac{1}{2},j}}{\partial y} - G_{i-\frac{1}{2},j}\dfrac{\partial v_{i-\frac{1}{2},j}}{\partial y}}{\Delta x} - \lambda\frac{\partial N_{i,j}}{\partial x} = 0\end{aligned} \tag{5.7}$$

$$\begin{aligned}&\frac{G_{i+\frac{1}{2},j}\dfrac{\partial v_{i+\frac{1}{2},j}}{\partial x} - G_{i-\frac{1}{2},j}\dfrac{\partial v_{i-\frac{1}{2},j}}{\partial x}}{\Delta x} + \frac{G_{i,j+\frac{1}{2}}\dfrac{\partial v_{i,j+\frac{1}{2}}}{\partial y} - G_{i,j-\frac{1}{2}}\dfrac{\partial v_{i,j-\frac{1}{2}}}{\partial y}}{\Delta y}\\ &+ \frac{1}{1-2\nu}\frac{G_{i,j+\frac{1}{2}}\dfrac{\partial u_{i,j+\frac{1}{2}}}{\partial x} - G_{i,j-\frac{1}{2}}\dfrac{\partial u_{i,j-\frac{1}{2}}}{\partial x} + G_{i,j+\frac{1}{2}}\dfrac{\partial v_{i,j+\frac{1}{2}}}{\partial y} - G_{i,j-\frac{1}{2}}\dfrac{\partial v_{i,j-\frac{1}{2}}}{\partial y}}{\Delta y} - \lambda\frac{\partial N_{i,j}}{\partial y} = 0\end{aligned} \tag{5.8}$$

$$\begin{aligned}
\frac{\partial u_{i+\frac{1}{2},j}}{\partial x} &= \frac{u_{i+1,j} - u_{i,j}}{\Delta x} + \mathcal{O}(\Delta x^2) & \frac{\partial v_{i+\frac{1}{2},j}}{\partial x} &= \frac{v_{i+1,j} - v_{i,j}}{\Delta x} + \mathcal{O}(\Delta x^2)\\
\frac{\partial u_{i-\frac{1}{2},j}}{\partial x} &= \frac{u_{i,j} - u_{i-1,j}}{\Delta x} + \mathcal{O}(\Delta x^2) & \frac{\partial v_{i-\frac{1}{2},j}}{\partial x} &= \frac{v_{i,j} - v_{i-1,j}}{\Delta x} + \mathcal{O}(\Delta x^2)\\
\frac{\partial u_{i,j+\frac{1}{2}}}{\partial y} &= \frac{u_{i,j+1} - u_{i,j}}{\Delta y} + \mathcal{O}(\Delta y^2) & \frac{\partial v_{i,j+\frac{1}{2}}}{\partial y} &= \frac{v_{i,j+1} - v_{i,j}}{\Delta y} + \mathcal{O}(\Delta y^2)\\
\frac{\partial u_{i,j-\frac{1}{2}}}{\partial y} &= \frac{u_{i,j} - u_{i,j-1}}{\Delta y} + \mathcal{O}(\Delta y^2) & \frac{\partial v_{i,j-\frac{1}{2}}}{\partial y} &= \frac{v_{i,j} - v_{i,j-1}}{\Delta y} + \mathcal{O}(\Delta y^2)\\
\frac{\partial u_{i,j}}{\partial x} &= \frac{u_{i+1,j} - u_{i-1,j}}{2\Delta x} + \mathcal{O}(\Delta x^2) & \frac{\partial v_{i,j}}{\partial y} &= \frac{v_{i,j+1} - v_{i,j-1}}{2\Delta y} + \mathcal{O}(\Delta y^2)
\end{aligned}$$

$$\begin{aligned}
G_{i+\frac{1}{2},j} &\approx \frac{G_{i+1,j} + G_{i,j}}{2} & \frac{\partial G_{i,j}}{\partial x} &= \frac{G_{i+1,j} - G_{i-1,j}}{2\Delta x} + \mathcal{O}(\Delta x^2)\\
G_{i-\frac{1}{2},j} &\approx \frac{G_{i,j} + G_{i-1,j}}{2} & \frac{\partial G_{i,j}}{\partial y} &= \frac{G_{i,j+1} - G_{i,j-1}}{2\Delta y} + \mathcal{O}(\Delta y^2)\\
G_{i,j+\frac{1}{2}} &\approx \frac{G_{i,j+1} + G_{i,j}}{2} & \frac{\partial N_{i,j}}{\partial x} &= \frac{N_{i+1,j} - N_{i-1,j}}{2\Delta x} + \mathcal{O}(\Delta x^2)\\
G_{i,j-\frac{1}{2}} &\approx \frac{G_{i,j} + G_{i,j-1}}{2} & \frac{\partial N_{i,j}}{\partial y} &= \frac{N_{i,j+1} - N_{i,j-1}}{2\Delta y} + \mathcal{O}(\Delta y^2)
\end{aligned}$$

After working out the equations and approximating all the partial derivatives, Equations 5.7 and 5.8 can be written as a linear system of equations: $B\mathbf{u} = g(\mathbf{N})$, where B is a matrix containing all the coefficients for u and v, and $g(\mathbf{N}) = \lambda\nabla\mathbf{N}$. This system is solved with a direct solver and was already implemented by Oudhof [11].

5.4. Calibration

For the parameter calibration, a non-linear least squares algorithm is used. This means the sum of the squared differences between the estimated and measured tumour cell numbers is minimised.

$$\text{argmin}_\beta ||N_\beta(\overline{x}, t_1) - \hat{N}(\overline{x}, t_1)||_2^2 \quad \text{for } \overline{x} \in \mathcal{X},$$

where $\mathcal{X}$ is the set of grid points, $\beta = (D_0, \alpha, k_1, \dots, k_n)$, $N_\beta(\overline{x}, t_1)$ is the result of predicting forward from t_0 to t_1 with the parameter estimate β and $\hat{N}(\overline{x}, t_1)$ is the measured tumour cell density at t_1. The calibration phase is in general the bottleneck regarding the computation time. One iteration consists of updating the parameters, calculating forward from t_0 to t_1 and comparing the outcome to the measured tumour density. If the convergence criterion is met, then the calibration is stopped. Else, the parameters are updated again and the algorithm continues.

As stated in Chapter 4, issues arise in the calibration phase as the number of parameters is higher than the number of data points. This section explains how these issues were solved and which non-linear least squares algorithm was used for calibration.

5.4.1. Parameter reduction

To speed up calibration, in the implementation of Oudhof [11] a region of interest (ROI) was defined around the tumour, which will be denoted by $\mathcal{K}$. Within that region of interest, the value of $k(\overline{x})$ is determined and outside of that region the values are set to zero, meaning $\beta = (D_0, \alpha, k_1, \dots, k_{n_k})$, where $n_k < n$. The minimisation problem is thus given by:

$$\text{argmin}_\beta ||N_\beta(\overline{x}, t_1) - \hat{N}(\overline{x}, t_1)||_2^2 \quad \text{for } \overline{x} \in \mathcal{K}$$

It is logical to assume the proliferation is zero outside of this ROI as the tumour will only grow in the nearby area around the tumour. This indeed speeds up computation, but one problem still remains: the number of unknowns is bigger than the number of data points. Suppose in the ROI there are n_k points, then in the calibration for each of those n_k points a value for $k(\overline{x})$ needs to be found. In addition, the global parameters D_0 and α need to be determined. This means there are n_k values to determine $n_k + 2$ parameters. In the work by Oudhof [11], there was one parameter less as the chemotherapy was not included, so α did not need to be estimated. There, the problem was solved by introducing a Tikhonov regularisation term to make sure that the problem was no longer ill-posed, which led to the minimisation problem given below.

$$\text{argmin}_\beta \left(||N_\beta(\overline{x}, t_1) - \hat{N}(\overline{x}, t_1)||_2^2 + ||\Lambda\beta_0||_2^2 \right) \text{ for } \overline{x} \in \mathcal{K}$$

Here, Λ denotes the Tikhonov regularisation term and $\beta_0 = D_0$. In this way the number of parameters and the number of data points were equal. With this addition to the minimisation formula, D_0 is forced to be small when Λ is big and D_0 can be calibrated more freely when Λ is small. The downside of this method was that the Λ still had to be estimated and the choice for Λ influenced the results quite a lot.

For the chemotherapy extension in this thesis, there is however an additional global parameters, so there are two more unknowns than data points. If the same method would be applied, two Tikhonov regularisation terms would have to be introduced, Λ_0 and Λ_1 and the minimisation problem would be as follows:

$$\text{argmin}_\beta \left(||N_\beta(\overline{x}, t_1) - \hat{N}(\overline{x}, t_1)||_2^2 + ||\Lambda_0\beta_0||_2^2 + ||\Lambda_1\beta_1||_2^2 \right) \text{ for } \overline{x} \in \mathcal{K}$$

Once again, different choices of the combination of Λ_0 and Λ_1 led to different results and thus it was decided to use a different method to solve the issue by reducing the number of parameters.

There are several options for this. One option, for example, would be to take literature values for α and D_0 and in this way make sure the number of unknowns equals the number of knowns. In that case, the proliferation rate, which is calibrated per voxel, would be the only value that is calibrated and thus differs for each patient. These parameters D_0 and α are however global parameters and are thus important to determine for each patient. Because of this, the idea emerged to try to reduce the number of voxels for which the proliferation rate has to be determined and thus define a reduced mask with fewer voxels in it. For this, it was observed in previous research [11] that the proliferation map returned by the calibration shows a smooth distribution of the values with no or little harsh boundaries. Therefore, one could say that the proliferation rate in one voxel is approximately equal to the average of its neighbours. This idea is central to the way that the reduced mask was set up.

The reduced mask $\mathcal{K}_{red}$ is defined within the ROI, meaning it is a subset of the original mask $\mathcal{K}$, where it includes all the points on the boundary of the ROI and in the interior of the ROI a chessboard structure is used. It is constructed as follows:

for $x_{i,j} \in \mathcal{X}$ **do**
  if $x_{i,j} \in \partial\mathcal{K}$ **then**
    $x_{i,j} \in \mathcal{K}_{red}$
  else
    if $(i \mod 2 = 0 \wedge j \mod 2 = 0) \vee (i \mod 2 = 1 \wedge j \mod 2 = 1)$ **then**
      $x_{i,j} \in \mathcal{K}_{red}$

The minimisation problem can then be written in terms of this reduced mask, where $\beta = (D_0, \alpha, k_1, \dots, k_{\hat{n}_k})$ and $\hat{n}_k$ represents the number of points in $\mathcal{K}_{red}$.

$$\text{argmin}_\beta ||N_\beta(\overline{x}, t_1) - \hat{N}(\overline{x}, t_1)||_2^2 \quad \text{for } \overline{x} \in \mathcal{K}_{red}$$

For the voxels that are within the ROI but are not included in the reduced mask, $k(\overline{x})$ is determined by taking the average of the neighbouring voxels that were included in the reduced mask. Because of the way that this mask was set up, these four neighbouring voxels that are part of the reduced mask will always exist. During calibration, the following steps are used to determine the proliferation rate value for each position in the breast.

for $x_{i,j} \in \mathcal{X}$ **do**
  if $x_{i,j} \in \mathcal{K}_{red}$ **then**
    $k_{i,j} = \beta(k_{i,j})$
  else
    if $x_{i,j} \notin \mathcal{K}_{red} \wedge x_{i,j} \in \mathcal{K}$ **then**
      $k_{i,j} = \frac{1}{4}\big(\beta(k_{i-1,j}) + \beta(k_{i+1,j}) + \beta(k_{i,j-1}) + \beta(k_{i,j+1})\big)$
    else
      $k_{i,j} = 0$

In Figure 5.4 the ROI $\mathcal{K}$ and the reduced mask $\mathcal{K}_{red}$ is displayed in yellow for p_1.

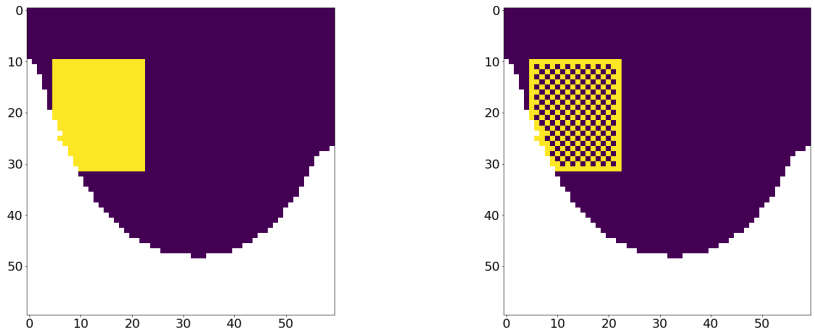

(a) $\mathcal{K}$ (b) $\mathcal{K}_{red}$

Figure 5.4: Masks for parameter calibration for p_1.

Note that at first there were n_k data points and $n_k + 2$ parameters to be estimated. With this mask, there are n_k data points and $\hat{n}_k + 2$ parameters, with $\hat{n}_k + 2 < n_k$. In this way, there are thus fewer parameters than there are data points.

5.4.2. Non-linear least squares algorithm

There are different choices for the non-linear least squares optimisation algorithm. In quite a lot of papers, the *Levenberg-Marquardt* (LM) algorithm is used for parameter calibration [3, 7–9, 14, 17]. However, in this thesis the *Trust Region Reflective* (TRF) algorithm, which is suitable for large sparse problems, is used instead. This algorithm is just like LM one of the methods that can be chosen in the `least_squares` function of the `scipy.optimize` library in Python.

Let us now shortly explain the workings of the algorithm to find the optimal parameters before we motive this choice. Suppose that the objective function, i.e. the function that should be minimised, is $f(\beta)$, where β represents the parameters. Then $f(\beta)$ is approximated by a quadratic function $q(s)$ that simulates the behaviour of $f(\beta)$ around the current point β in a neighbourhood N, which is called the trust-region. The so-called trust-region sub-problem consists of computing a trial step s by minimising the area N. Then, if $f(\beta + s) < f(\beta)$, β is updated to be $\beta + s$ and the step is successful and the trust region remains the same. However, if the step is unsuccessful, then β stays the same and the trust region N is reduced for the next step [28]. More details on the exact workings of the algorithm can be found in [29].

This algorithm was chosen instead of LM as it was usually faster in finding the optimised parameters. Another big advantage of TRF is that bounds can be given to the parameters. In general, no bounds were given, but when the calibration yielded a negative value for either D_0 or α, then the calibration was run again with a lower bound for these parameters.

6

Chemotherapy extension

In this chapter, two methods to calculate the chemotherapy term are introduced. Firstly, with the standard Kety-Tofts model in Section 6.1 and secondly with the Normalised Blood Volume Map in Section 6.2, followed by a comparison in Section 6.3. Next, an extensive model analysis is made in Section 6.4 and lastly, the results for all models and patients are presented in Section 6.5.

6.1. Kety-Tofts model

As explained in Section 3.2, one of the options to calculate the chemotherapy term is to use the standard or extended Kety-Tofts model. For simplicity, only the standard Kety-Tofts (KT) model (i.e. the model with $v_p = 0$) is used in this thesis. This section explains how this model can be used to estimate the concentration of chemotherapy in the tissue.

6.1.1. Overview of steps

The parameters for the basic model are K^{trans} and v_e, which need to be determined for each voxel. To calculate these parameters, information is needed on the concentration of contrast agent (CA) found in the plasma and in the tissue, as these are used to determine the parameters with which the concentration of drug in the tissue is estimated. This means that the DCE-MRI images are used to derive $C^{CA}_{plasma}(t)$ and based on the literature a function is chosen for $C^{CA}_{tissue}(t)$, which is also called the *arterial input function* (AIF) [4, 19]. Once these are determined, the values can be fit to Equation 6.1 for each voxel to yield parameters estimates $K^{trans}(\overline{x})$ and $v_e(\overline{x})$.

$$C^{CA}_{tissue}(t) = K^{trans} \int_0^t \Big(C^{CA}_{plasma}(s) \cdot \exp\big(-\frac{K^{trans}}{v_e}(t-s) \big) \Big) ds \tag{6.1}$$

After finding reasonable parameter estimates, the next step is to determine $C^{drug}_{plasma}(t)$ based on the literature and the treatment schedule. Next, the parameters and these values are combined to calculate $C^{drug}_{tissue}(\overline{x}, t)$ with Equation 6.2.

$$C^{drug}_{tissue}(\overline{x}, t) = K^{trans}(\overline{x}) \int_0^t \Big(C^{drug}_{plasma}(s) \cdot \exp\big(-\frac{K^{trans}(\overline{x})}{v_e(\overline{x})}(t-s) \big) \Big) ds \tag{6.2}$$

In summary, finding the chemotherapy term with the KT model comes down to the following steps:

1. Derive $C^{CA}_{plasma}(t)$ and $C^{CA}_{tissue}(t)$
2. Calculate $K^{trans}(x)$ and $v_e(x)$ by fitting $C^{CA}_{plasma}(t)$ and $C^{CA}_{tissue}(t)$ to Equation 6.1
3. Derive $C^{drug}_{plasma}(t)$
4. Calculate $C^{drug}_{tissue}(\overline{x}, t)$ with Equation 6.2

This approach is similar to the one presented by Jarret et al. [7] and in the next sections these steps are worked out.

6.1.2. Choosing arterial input function

There are many different options to obtain an AIF. One approach is to sample directly from the blood during the administering period. Although this yields accurate characterisations of $C^{CA}_{plasma}(t)$, this approach is impractical and invasive for the patient. Secondly, it is possible to determine the AIF per patient based on the DCE-MRI images. Although this is non-invasive and patient-based, it is time-consuming and requires that a major vessel like the aorta is visible on the scan, which is often far from the tumour in the breast. Other options also exist, but the most common and convenient way is to use an assumed or population-based AIF [19, 30]. In this thesis, an assumed AIF will be used, although it is argued by some researchers that these types of AIFs introduce systematic errors in the parameters and pharmacokinetic analysis [19, 31].

A lot of research has been done into assumed AIFs and it was found that depending on the application one should choose a suitable AIF as there is no AIF that works best for all cases. In a paper by Woolf et al. [30] six different AIFs were analysed to determine which one performed best in assessing breast cancer response. The included AIFs were: Cosine Bolus Parker, Femoral Artery, Fritz-Hansen, Modified Fritz-Hansen, Weinmann and Biexponential Parker. The AIFs were analysed on their ability to minimize the number of computational fit fails, their ability to produce physiologically valid parameters and their ability to correctly detect pCR. In their conclusion, they recommended using Modified Fritz-Hansen or Cosine Bolus Parker when there is no measured AIF as these both performed reasonably well in all three criteria.

In this work, the Cosine Bolus Parker function with parameters and values from Orton et al. is used. [22]. The function is given by the following formula:

$$C^{CA}_{plasma}(t) = \begin{cases} a_B(1-\cos(\mu_B t)) + a_B a_G f(t,\mu_G) & \text{for } 0 \le t \le t_B \\ a_B a_G f(t_B,\mu_G) e^{-\mu_G(t-t_B)} & \text{for } t > t_B \end{cases}$$

The function $f(t,\mu_G)$ is defined below.

$$f(t,a) = \frac{1}{a}(1-e^{-at}) - \frac{1}{a^2+\mu_B^2}\left(a\cos(\mu_B t) + \mu_B \sin(\mu_B t) - ae^{-at}\right)$$

The same values for the input parameters are taken as the ones assumed in the paper, which are as follows:

$$\begin{aligned} a_B &= 2.84 \quad \mu_B = 22.8 \\ a_G &= 1.36 \quad \mu_G = 0.17 \\ t_B &= \frac{2\pi}{\mu_B} \end{aligned}$$

The motivation for this function is that the curves that are generated by it show a similar shape to the curves of measured AIFs. In addition, the terms of the function are relatively simple and easy to calculate with, which is important as this function is needed to calculate the concentration of contrast agent in the tissue for different parameter values. A graph of this function can be seen in Figure 6.1.

By writing $k_{ep} = \frac{K^{trans}}{v_e}$ in Equation 6.1, the following formula is obtained:

$$C^{CA}_{tissue}(t) = K^{trans} \int_0^t C^{CA}_{plasma}(s) \cdot e^{-k_{ep}(t-s)} ds \tag{6.3}$$

In literature the value k_{ep}, which represents the rate between the extravascular extracellular space and the blood plasma [32], is referred to as the *redistribution rate constant* [19] or *efflux rate constant* [2].

One of the advantages of the Cosine Bolus Parker function is that when it is used in the formula above, the integral can be written out into the analytical expression given in Equation 6.4. The proof for this is given in Appendix A.4.

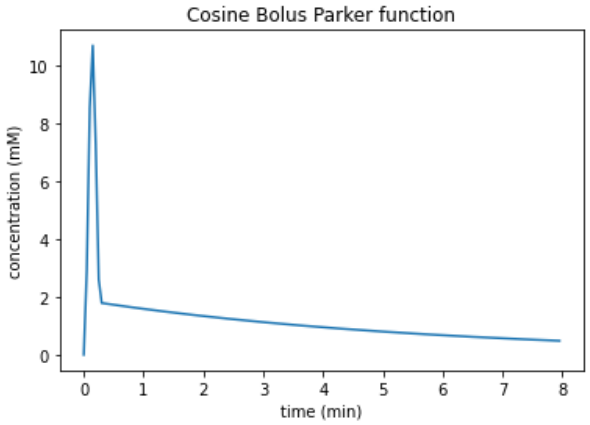

Figure 6.1: Cosine Bolus Parker function which is used as $C_{plasma}^{CA}(t)$

$$C_{tissue}^{CA}(t) = \begin{cases} \frac{a_B a_G K^{trans}}{k_{ep}-\mu_G}\left(f(t,\mu_G) + \left(\frac{k_{ep}-\mu_G}{a_G} - 1\right)f(t,k_{ep})\right) & \text{for } 0 \leq t \leq t_B \\ \frac{a_B a_G K^{trans}}{k_{ep}-\mu_G}\left(f(t_B,\mu_G)e^{-\mu_G(t-t_B)} + \left(\frac{k_{ep}-\mu_G}{a_G} - 1\right)f(t,k_{ep})e^{-k_{ep}(t-t_B)}\right) & \text{for } t > t_B \end{cases} \tag{6.4}$$

Below the influence of the parameter choice for v_e and K^{trans} is demonstrated. From these plots, it becomes clear that in general K^{trans} determines the height and slope of the initial peak while v_e determines the behaviour of the curve after this peak.

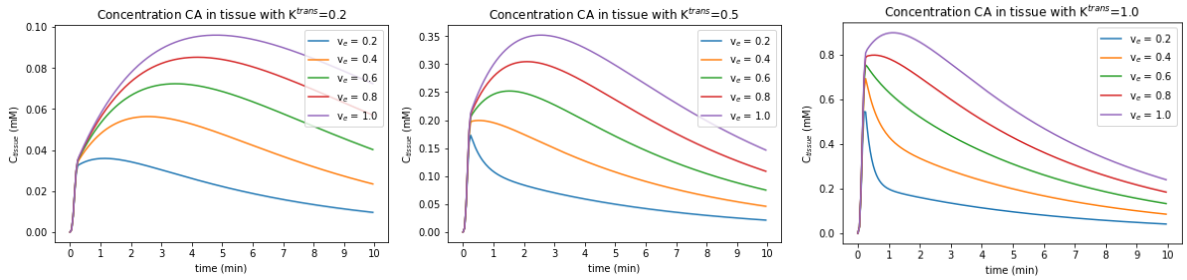

(a) (b) (c)

Figure 6.2: CA concentration for various values of K^{trans}

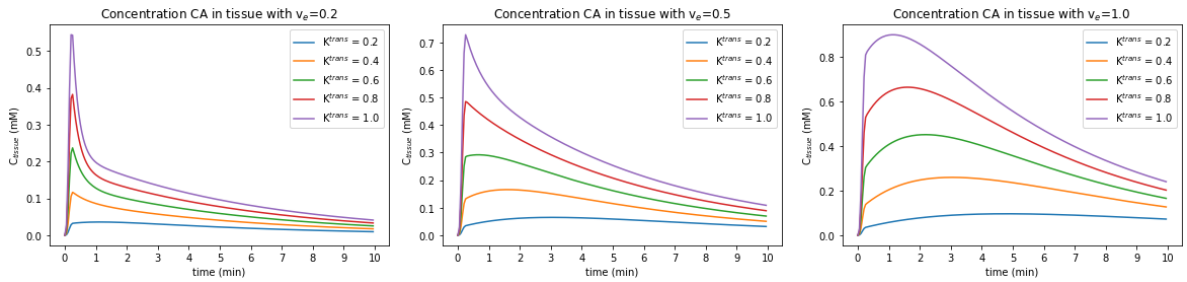

(a) (b) (c)

Figure 6.3: CA concentration for various values of v_e.

6.1.3. Deriving CA concentration from DCE scans

The next step in the process to determine the parameters for the model is to derive the concentration of CA in the tissue of the scans. Just like for the AIFs, there are different ways to obtain these values. In the literature, three different approaches have been identified, which are described below. In Section 5.1, it was explained that the DCE scans consist of 8 scans. For notation, we will denote $s(t_n)$ for the signal intensity of the scan at time t_n, where $n \in \{0, 1, \dots, 7\}$.

Method 1: LC with assumed T_{10} values

Linear conversion (LC) is described by Wake et al. [33]. As the name suggests, LC refers to the linear conversion of signal intensity $s(t)$ from the DCE scans to the concentration $C^{CA}_{plasma}(t)$, as opposed to *non-linear conversion* (NLC), which logically refers to non-linear conversion. For LC, Equation 6.5 can be used to calculate the concentration in each voxel at each time point t_n of the DCE scans.

$$C^{CA}_{plasma}(t_n) = \frac{1}{r_1 T_{10}}\left(\frac{s(t_n)}{s_0} - 1\right) \tag{6.5}$$

In the formula above, s_0 is a constant that describes the proton density and scanner gain [19, 31, 34] which is sometimes taken as the average pre-contrast signal [33, 35]. In addition, r_1 is the longitudinal relaxivity rate of the contrast agent, which is usually taken to be either 4.5 [35, 36] or 3.9 $mM^{-1}s^{-1}$ [33]. The latter was chosen as the approach suggested in that paper is followed here. Lastly, T_{10} is the T_1 value before the CA is injected. T_1 values represent the time it takes for nuclei to align after an MR pulse has been given. They depend on the type of tissue, the strength of the magnetic field (which is 1.5T for our data) and the presence of contrast agents as these shorten T_1 times [35]. Determining these values is crucial as they greatly influence the estimates of the parameters K^{trans}, v_e and v_p [20, 33]. In the study by Wake et al. the basis Kety-Tofts model was considered, meaning that v_p was set to 0. In their simulation study, they found that higher T_{10} values, which were varied between 700 and 2500 ms, yielded lower estimates for K^{trans} and v_e. In addition, they found that for a small flip angle (in their study FA= $12°$) the smallest errors were found with LC combined with an assumed AIF compared to a measured AIF and that in that case K^{trans} and v_e were least affected by the assumed T_{10} value.

In Table 6.1 T_1 literature values for different tissue types are summarised. As no contrast agent was present, these T_1 values can be used as assumed T_{10} values. Since Merchant et al. present values for all three tissue types that we consider, the means of their reported T_1 values are taken as assumed T_{10} values.

Tissue	Rakow-Penner et al. [37]	Merchant et al. [38]
Adipose	296.01 ± 12.94	264.02 ± 2.38
Fibroglandular	1266.18 ± 81.8	795.64 ± 21.12
Tumour	-	876.09 ± 27.83

Table 6.1: Mean T_1 relaxation times and standard deviations in ms from literature for 1.5T

Method 2: NLC with fitted T_1 and assumed T_{10} values

In the same paper by Wake et al. NLC is described as an alternative to LC, which is also used by Tofts [35]. For this method, the concentration of CA is calculated with Equation 6.6.

$$C^{CA}_{plasma}(t_n) = \frac{1}{r_1}\left(\frac{1}{T_{1n}} - \frac{1}{T_{10}}\right) \tag{6.6}$$

For this approach, both papers use assumed T_{10} values and calculate the T_{1n} values by fitting the signal intensities from each DCE image to the so-called *spoiled gradient echo* (SPGRE) equation [19, 33]. For this approach, one needs spoiled gradient echo images with different flip angles in addition to the DCE images, which is done quite often in research related to this topic [2, 4, 18, 31, 39]. It is important to note that in theory, one could measure the T_1 values, but this is very time-consuming [19]. Other approaches than SPGRE include spin-echo images obtained at different repetition times or inversion recovery methods [20]. Compared to these, the SPGRE multi-flip approach requires less time and still maintains a high signal-to-noise ratio, which is important for MRI scans and thus explains

why this approach is widely used in DCE-MRI analysis. Equation 6.7 below describes the SPGRE equation.

$$s(t_n) = s_0 \sin\phi \frac{1 - \exp(-TR/T_{1n})}{1 - \cos\phi \exp(-TR/T_{1n})} \tag{6.7}$$

Here, TR refers to the repetition time of the DCE scan, which is the time between pulses of an MRI and ϕ is the flip angle that was used in the scan.

Method 3: NLC with fitted T_1 and fitted T_{10} values
Lastly, Yankeelov et al. [19] and Chikui et al. [34] use a similar but slightly different approach to the one presented before. NLC is again used, so the concentration is calculated using Equation 6.6. However, instead of using assumed T_{10} values, they use the SPGRE equation to find the T_{10} values.

$$s(t_0) = s_0 \sin\phi \frac{1 - \exp(-TR/T_{10})}{1 - \cos\phi \exp(-TR/T_{10})} \tag{6.8}$$

The next step is to calculate the T_{1n} values. For this, the ratio of $s(t_n)$ to $s(t_0)$, so Equations 6.8 and 6.7, are used and fitted to the data.

$$\frac{s(t_n)}{s(t_0)} = \frac{s_0 \sin\phi \frac{1-\exp(-TR/T_{1n})}{1-\cos\phi \exp(-TR/T_{1n})}}{s_0 \sin\phi \frac{1-\exp(-TR/T_{10})}{1-\cos\phi \exp(-TR/T_{10})}} = \frac{(1 - \exp(-TR/T_{1n}))}{(1 - \exp(-TR/T_{10}))} \frac{(1 - \cos\phi \exp(-TR/T_{10}))}{(1 - \cos\phi \exp(-TR/T_{1n}))}$$

Wake et al. [33] compare methods 1 and 2 and report on how they influence the estimates for K^{trans} and v_e for the basic Kety-Tofts model. In their study, it is clearly shown that methods 1 and 2 lead to different parameter estimates. One of their findings is that when T_{10} is unknown, LC provides more accurate parameters while NLC provides more robust parameters. Another finding that is worth noting is that they suggest combining LC with an assumed AIF when a small FA is used and T_{10} is not measured as this will minimise the uncertainty that is introduced by as assumed T_{10}. Lastly, it was found that LC usually overestimates the parameters, especially for small FA. One of the explanations is given by Guo et al. [20], who claim that for SPGRE signals with small FA there is a strong non-linear relationship between the change in relaxation rate and the signal enhancement.

After implementing these methods, the results of method 2 and 3 turned out to be extremely similar. For this reason, only the results for methods 1 and 2 are presented in Figures 6.4a and 6.4b respectively.

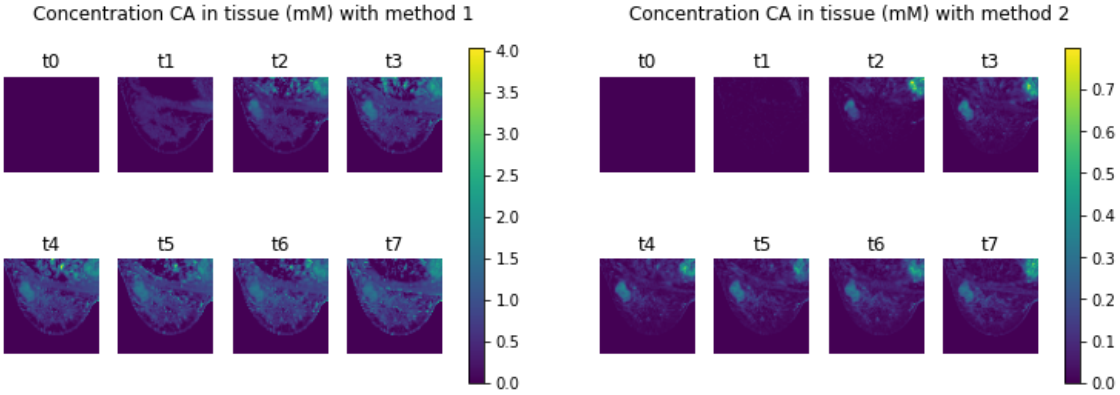

(a) Method 1

(b) Method 2

Figure 6.4: CA concentration

In both pictures, the tumour has a higher concentration of CA than the surrounding tissue, which is to be expected. It is important to note however that the scales for both pictures are quite different and that the calculated concentrations are much higher for LC than for NLC. In the next step, the parameters are fitted with both LC and NLC.

6.1.4. Fitting parameters

In this section we will elaborate on how the parameters are fitted using the information from the previous sections. As a fitting method, the `curve_fit` function from the `scipy.optimize` Python library is used, for which the AIF as described in Equation 6.4 is given as input, together with the DCE images and an array with timestamps corresponding to the time when the DCE images have been made. By definition, it is known that $0 \leq v_e \leq 1$ and in addition it is known from the literature that in general $0 \leq K_{trans} \leq 2$ [18, 19, 22, 33]. For this reason, we also provide the above bounds to the algorithm. To speed up computation time, the parameters are only estimated for each voxel within the breast and all other values are set to zero.

In Figures 6.5 and 6.6 box plots are displayed for the found values of K_{trans} and v_e for p_1, where the orange line indicates the median value as usual and the green arrow indicates the mean value. The box plots of the other patients are similar and therefore left out. Note that K_{trans} is measured in $1/min$ here, but for the model this has to be converted to $1/day$ so all values will have to be multiplied by a factor $(24 * 60)$. In these box plots, there is a clear difference between the found values with LC and NLC. In general, both the K_{trans} and the v_e values for LC are a lot higher than the values for NLC. This is interesting, especially since Wake et al. state that in general LC estimates are lower than NLC estimates for both K_{trans} and v_e. A possible explanation for this is the difference in presumed AIFs: for this study the Cosine-Bolus Parker function was used, but Wake et al. used the original Parker function [21, 33]. Another cause could be that the DCE images of that study were made with a 3T scanner, while the images for this research were made with 1.5T. The difference in magnetic field strength yields different T1 values and could therefore lead to different parameter estimates.

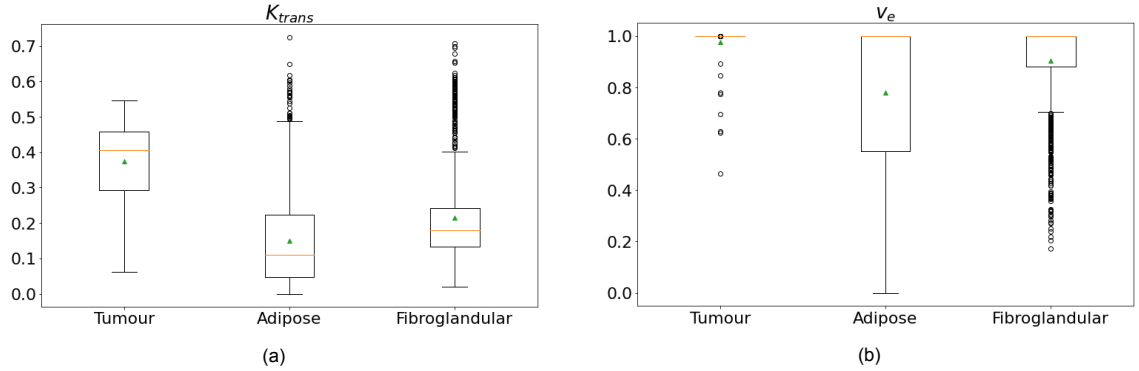

Figure 6.5: Fitted parameter values for p_1 with LC.

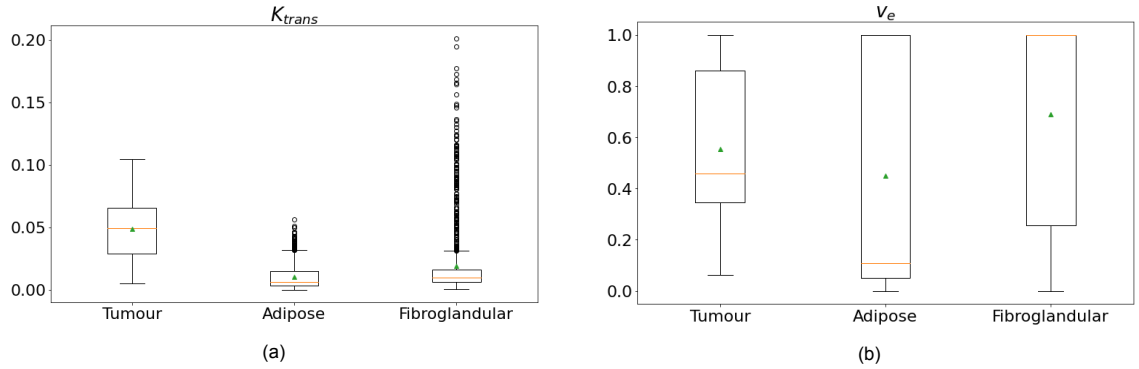

Figure 6.6: Fitted parameter values for p_1 with NLC.

Let us now compare these fitted parameters to some literature values. Using the same AIF and assuming a linear relationship between the T_1 estimates and CA concentration, Orton et al. report a median value for K_{trans} of 0.20 and 0.13 and a median value for v_e of 0.46 and 0.35 for tumour

and lymph tissue respectively. These median values can be compared to the median values that are displayed by the orange line in the box plots. Firstly, considering tumorous tissue, it can be seen that for LC the value of K_{trans} is a lot higher than the one from Orton et al. but for NLC it is a lot lower. On the other hand, the median v_e value in LC is way higher and the NLC value is very close to the literature value. Secondly, considering fibroglandular, i.e. lymph, tissue, the found K_{trans} value with LC is comparable to the literature value but the NLC value is a lot lower. For v_e both LC and NLC values are a lot higher than the value reported by Orton et al. In their paper, they also mention the median values for muscular tissue, but because this thesis only focuses on tumour, adipose and fibroglandular tissue these values are left out for the comparison as muscular tissue is not comparable to these types of tissue. Wake et al. also estimated K_{trans} and v_e values for tumorous tissue in patients with breast cancer, although they used a different AIF. The median K_{trans} value for LC was 0.0016 and the median for NLC was 0.0021 and the median v_e value for LC was 0.34 and for NLC was 0.52. Note that the K_{trans} values are a lot lower than the ones found both in this research and in the paper by Orton et al. The v_e data are more comparable but, as noted before, the parameter values of NLC from Wake are higher than the ones of LC while our values are exactly the other way around. Lastly, Yankeelov et al. [19] report on an average value of 0.0077 for K_{trans} within the tumour, which is a lot lower than the mean value was was found in this study (displayed by the green triangle), and 0.70 for v_e within the tumour, which in turn is higher than the mean value was that presented here. No literature has been found that reported on these parameter estimates for adipose breast tissue. All in all, it seems like NLC provides more realistic values that are in line with literature which is why it was decided to continue working with NLC.

6.1.5. Deriving concentration of drug in plasma

Now that the parameters have been fitted, the following step is to calculate the concentration of drug in the tissue for each voxel. For this, a function $C_{plasma}^{drug}(t)$ that describes the concentration of drug in the plasma is needed. It is difficult to precisely describe this function, as the anti-tumour treatment of the patients consists of different components: carboplatin, paclitaxel, trastuzumab and pertuzumab. Therefore, for simplicity purposes, for now only carboplatin is considered. In a paper by Oguri et al., a triexponential function is given to model the concentration of carboplatin in plasma [40].

$$C_{plasma}^{carboplatin}(t) = A_1 e^{-\gamma_1 t} + A_2 e^{-\gamma_2 t} + A_3 e^{-\gamma_3 t} \tag{6.9}$$

Here, γ_1, γ_2 and γ_3 describe the fast, middle and slow decay processes respectively and A_1, A_2 and A_3 represent the corresponding ordinate intercepts, i.e. the concentration value at $t = 0$. In the paper, the values were fitted to blood sample data taken from patients. Different values were found, depending on the dosage of the patient. The choice was made to take the values of the dosage that most patients had received. Because the γ_1, γ_2 and γ_3 values are given in $1/\text{hour}$ and the time scale of this thesis is in days, these have to be converted to $1/\text{day}$. The following values are taken for the parameters:

$$\begin{aligned} A_1 &= 12.06 \quad \gamma_1 = 70.32 \\ A_2 &= 17.17 \quad \gamma_2 = 12.82 \\ A_3 &= 2.367 \quad \gamma_3 = 0.86 \end{aligned}$$

Using the expression given for $C_{plasma}^{carboplatin}(t)$ in 6.2 yields:

$$\begin{aligned} C_{tissue}^{drug}(\overline{x}, t) &= K^{trans}(\overline{x}) \int_0^t \left(\left(A_1 e^{-\gamma_1 s} + A_2 e^{-\gamma_2 s} + A_3 e^{-\gamma_3 s} \right) \cdot e^{-k_{ep}(\overline{x})(t-s)} \right) ds \\ &= K^{trans}(\overline{x}) \int_0^t \left(\left(\sum_{i \in \{1,2,3\}} A_i e^{-\gamma_i s} \right) \cdot e^{-k_{ep}(\overline{x})(t-s)} \right) ds \\ &= K^{trans}(\overline{x}) e^{-k_{ep}(\overline{x})t} \sum_{i \in \{1,2,3\}} \left(A_i \int_0^t e^{s(k_{ep}(\overline{x}) - \gamma_i)} ds \right) \\ &= K^{trans}(\overline{x}) \sum_{i \in \{1,2,3\}} \frac{A_i}{k_{ep}(\overline{x}) - \gamma_i} \left(e^{-\gamma_i t} - e^{-k_{ep} t} \right) \end{aligned}$$

Using this expression, chemotherapy curves can be calculated for each voxel in the breast. Results will be shown in Section 6.3 where the outcomes of this method are compared to the ones that were made using the Normalised Blood Volume Map.

6.2. Normalised Blood Volume Map

An alternative option exists to calculate the concentration of drug in the tissue, this method will be referred to as the Normalised Blood Volume Map (NBVM). It is also used by Jarrett et al. in the third paper on the DIMCRD model [9]. They motivate their choice by stating that the pharmacokinetic analysis with the Kety-Tofts model is not suitable for DCE scans with a bad temporal resolution, which means that there is a long time gap between two consecutive scans. The temporal resolutions of the DCE scans for the different papers on the DIMCRD model and of this thesis are summarised in Table 6.2 below. The DCE data that was used in the first two papers had a high temporal resolution and the data for the third study had a very low temporal resolution. The temporal resolution for this study lies between those values, which motivated the choice to test both KT and NBVM.

Study	Temporal resolution
Jarrett et al. [7]	14.6-20.2 s
Jarrett et al. [8]	7.27 s
Jarrett et al. [9]	180s
This study	70s

Table 6.2: Temporal resolutions for the three papers on the DIMCRD model and this study.

6.2.1. Overview of steps

Determining $C_{tissue}^{drug}(\overline{x}, t)$ using NBVM consists of the following steps:

1. Subtract the average pre-contrast from the post-contrast values to obtain a baseline-subtracted time course for each voxel. For this, let $s(\overline{x}, t_n)$ denote the DCE signal value in position $\overline{x}$ at time t_n, with $n \in \{0, 1, ...7\}$ as 8 scans were made in total, of which 2 are pre-contrast and 6 are post-contrast. Then the baseline-subtracted time course for each voxel $\overline{x}$ can be calculated as follows:
$$S_b(\overline{x}, t_n) = S(\overline{x}, t_n) - \frac{1}{2}(S(\overline{x}, t_0) + S(\overline{x}, t_1))$$

2. Determine the Area Under the Curve (AUC) value of the baseline-subtracted time course.
$$AUC(\overline{x}) = \int_{t_2}^{t_7} S_b(\overline{x}, t_n)dt$$

3. Normalise the AUC values by the maximum AUC value of the tumour, this yields the NBVM and thus the initial drug distribution, which is denoted by $C_{tissue}^{drug}(\overline{x}, t^*)$, where t^* refers to the time of treatment.
$$C_{tissue}^{drug}(\overline{x}, t^*) = \frac{AUC(\overline{x})}{\max_{\overline{x^*} \in X_{tum}} AUC(\overline{x^*})}$$

4. Multiply the NBVM with an exponential that describes the decay of the drug in the tissue, where β refers to the decay rate of the drug:
$$C_{tissue}^{drug}(\overline{x}, t) = C_{tissue}^{drug}(\overline{x}, t^*)e^{-\beta(t-t^*)}$$

6.2.2. Estimating drug decay rate

In this section we will explain how we choose the value for the drug decay rate parameter β. One option could be to include β in the calibration to find the optimal value, but it was found that this takes extremely long. This is probably caused by its relationships with the drug efficacy α term that the chemotherapy term is multiplied with, which is also included in the calibration. Thus, various combinations of α and β

will lead to the same result which causes a long calibration time. In the research by Jarrett et al, β was included in the calibration but it was restricted to some literature-based bounds [8, 9]. These bounds were based on the terminal elimination half-lives of the drugs, which is the time that it takes after administration for the concentration of drug in plasma to decrease by 50% after reaching an equilibrium, i.e. in the elimination phase of the drug. This should not be confused with normal half-lives of drugs, which refer to the time that it takes for a certain concentration to decrease by 50% from the moment of administration.

Let us first analyse the influence of β on the chemo concentration and the tumour cell number before choosing its value. Figure 6.7a shows the chemo concentration between days 10 and 20, which is when the patient is treated for the first time, for various values of β. As expected, the chemo concentration decreases quicker when β is higher. Note that if $\beta = 0$, the chemo concentration would not decrease anymore after the peak and would stay at its maximum. Figure 6.7b instead shows the influence of β on the total tumour cell number which is displayed on a logarithmic scale. For these plots, the calibration was executed with the given value of β, which means that different chemotherapy curves were used for each simulation and the optimised parameter values differ. As can be seen, the total number of tumour cells for $\beta = 0.20$ starts oscillating after its initial decrease. Although the error at t_2 is the smallest for this value, it does not seem to give realistic results: it can be expected that treatment will kill the tumour cells, which could partially grow back but it should not be as quickly as it is for this case. In addition, a negative D_0 value was found which is also unwanted. It is interesting to see that $\beta = 0.40, \beta = 0.60$ and $\beta = 1.00$ all show different initial behaviour, but after t_1 the curves seem to align. Moreover, it is also curious to see that the behaviour of the curve for $\beta = 0.80$ is quite different from those cases and seems to also oscillate around some equilibrium, which means that the number of tumour cells will never go to zero, just like the case $\beta = 0.20$. In addition, it was found that for smaller β, the time step has to be decreased as otherwise with the optimised values the bound on Δt is not met. From this, it can be concluded that the choice of β heavily influences the behaviour and outcome of the model.

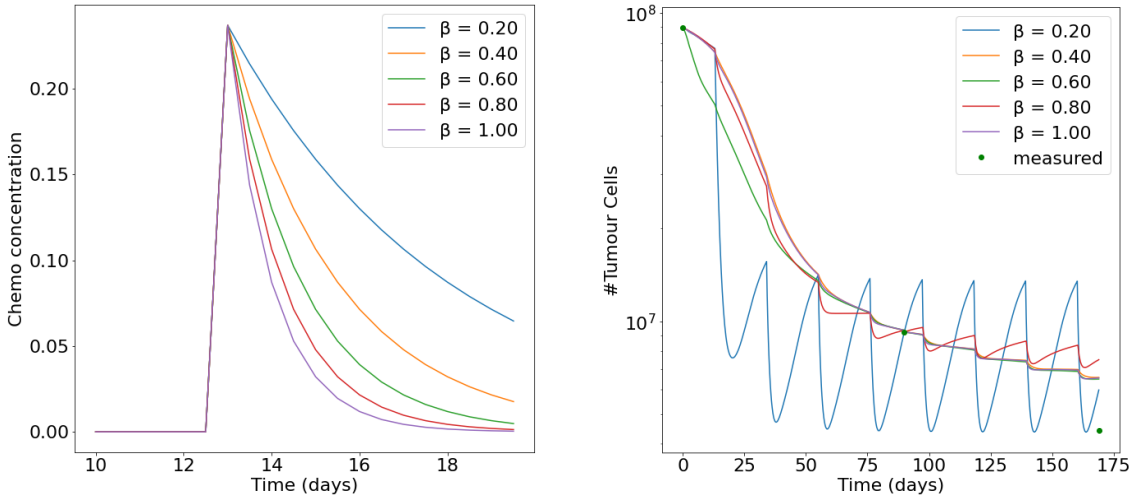

Figure 6.7: Plots displaying the influence of β. On the left, the average chemotherapy concentration between days 10 and 20 is displayed for various β and on the right, the total tumour cell number is displayed, where for the calibration the displayed values of β were used.

As it is not immediately clear from this analysis which value should be chosen for β, let us provide some information found in the literature on the pharmacokinetics of carboplatin. In a paper by van der Vijgh [41], which was also cited by both DIMCRD papers that use NBVM [8, 9], the different values found in papers on the distribution half-life, initial elimination half-life and the terminal elimination half-life of carboplatin are discussed. The value of the terminal elimination half-life in most studies lies around 5 days, although in one paper a much lower value was found. In that paper by Oguri et al., which was also used in this thesis to derive the plasma concentration function in Section 6.1.5, the

found values vary between 0.9 and 1.7 days, depending on the dose that was given [40]. The literature is thus also not fully conclusive on what value should be taken and it is unclear how the β should be chosen based on the terminal elimination half-life.

In the end, the choice was made for $\beta = 0.50$, as this provided the most stable results. With this, we mean that no unexpected negative parameter values were found, the time step remained stable, and the resulting total number of tumour cells did not show the oscillations that were seen for some other values.

6.3. Comparison of methods

In this section, the advantages and disadvantages of both methods to determine the chemotherapy term are discussed and their outcomes are compared. Firstly, let us look at what the average chemo concentration curve looks like after the first treatment for different tissue types, which is displayed in Figure 6.8. It can be observed that for the KT method, the concentration in fibroglandular tissue is higher than the concentration in adipose tissue, and the concentration in adipose tissue is higher than that in tumorous tissue. For NBVM, the concentration is highest in the tumour, followed by the fibroglandular tissue and the adipose tissue. These outcomes for NBVM are comparable to what was found in the paper by Jarrett et al. [9] in which the NBVM was used and it is expected that for targeted therapies like trastuzumab and pertuzumab this is realistic as they target the tumour. For chemotherapy, which targets any type of cell that is dividing, it cannot be guaranteed that the concentration in the tumour is highest. However, there will most likely be more dividing cells in the tumour than in the adipose tissue, which is indeed shown for NBVM but not for KT. Note that the peaks for KT are slightly higher than the ones for NBVM and that the decay rate for KT is a lot higher than for NBVM. Another remark about both figures is that all lines peak at the same time. Chemotherapy is given intravenously, which is why perhaps we would expect it to first peak in the fibroglandular tissue through which it is transported before it peaks in the tumorous or adipose tissue, but both models do not show this.

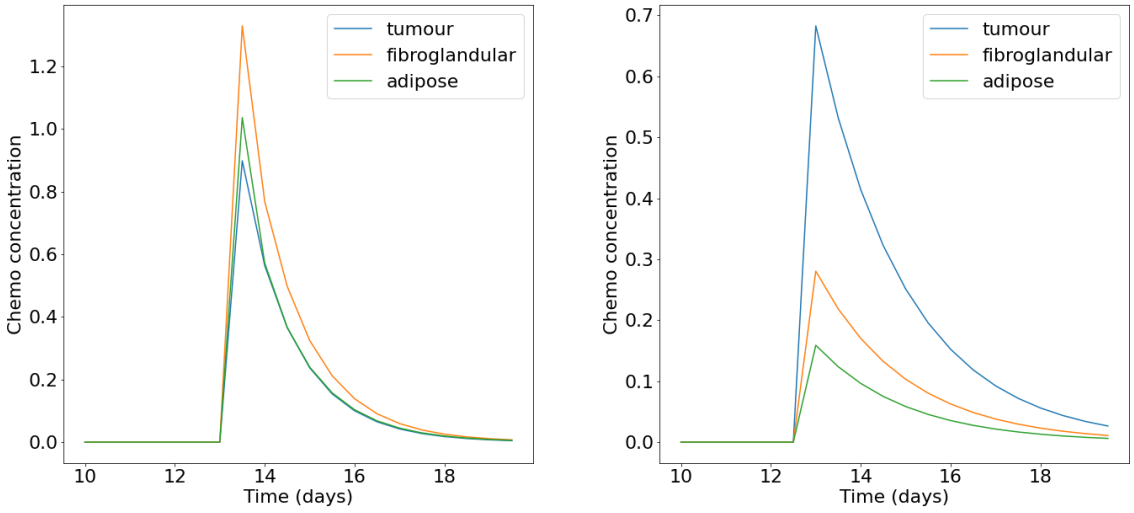

(a) KT (b) NBVM

Figure 6.8: Average chemo concentration per tissue type for Kety-Tofts model (left) and the Normalised Blood Volume Map (right).

Instead of only looking at the average chemo curves per tissue type, we are also interested in how the drug distributes throughout the breast after chemo, which is displayed in Figure 6.9. It can be seen that for KT the concentration in the tumour is indeed quite low compared to the other tissue types and that the image is not very smooth. This is probably because for the fibroglandular tissue almost all calibrated values for v_e were set to one and also the K_{trans} values are quite similar as previously displayed in the box plots in Figure 6.6. Therefore, in the fibroglandular points, the chemo concentration is almost everywhere approximately the same because the concentration is calculated based on these values. In addition, the concentration in some adipose points is relatively high which is unexpected as

explained before. For the NBVM images, the concentration in the tumour is highest, followed by the concentration in the fibroglandular tissue. The image is quite smooth and the CA pattern from the DCE scans can be recognised in which the tumour gave high intensity values because of the CA that spread there. As stated before, this method seems reasonable for targeted therapies, but in our opinion it is in this case also more realistic than KT when looking at the distribution in the different tissue types.

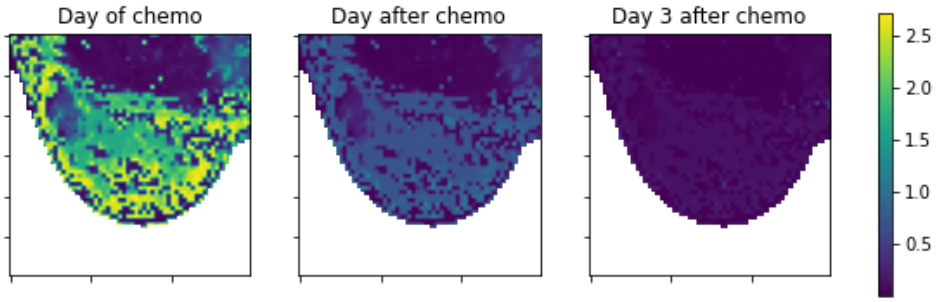

(a) KT

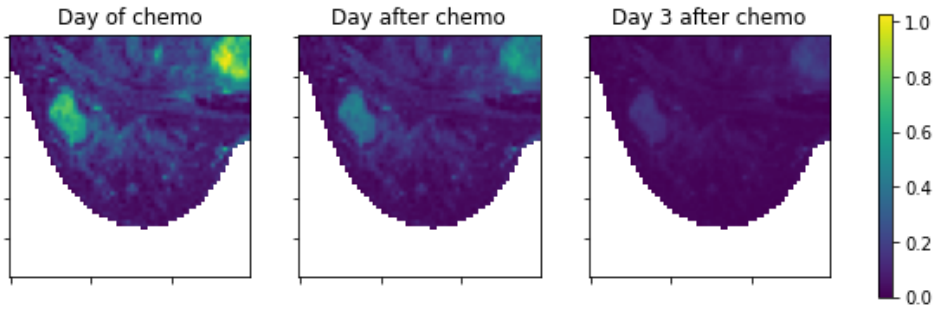

(b) NBVM

Figure 6.9: Distribution of chemo on the day of treatment, the day after and three days after treatment for Kety-Tofts model (top) and Normalised Blood Volume Map (bottom).

Lastly, let us make some final remarks about both methods to calculate the concentration of chemotherapy in the tissue. The advantage of KT is that it is a model based on the physical process of how drugs travel from the blood plasma to the tissue. In addition, it is used in quite a lot of papers. The disadvantage of this method however is that many choices have to be made and many steps have to be taken: firstly we had to choose an AIF, secondly we had to decide to use LC or NLC for determining the concentration of CA in the scans, next multiple parameters had to be fitted for each voxel and lastly we needed to choose the function to describe the concentration of drug in the plasma. In addition, our data might not be suitable for this method as it is downsampled in the spatial domain, which perhaps causes the parameters to take on high and unrealistic values as we saw, and it has a relatively low temporal resolution, which motivated us to also look into NBVM. NBVM was compared to KT an easy and quick method to implement, with little steps to be taken and fewer choices that had to be made. However, it is rather unclear what the NBVM physically represents, what it is based on and what the underlying assumptions are. Furthermore, the only thing that had to be chosen carefully was the parameter β, which turned out to be difficult as different choices led to different results and fitting this parameter was not feasible. As a final remark, it is also important to look at how these models should be used when a different drug than carboplatin is being considered. For KT, the parameters could be kept the same, but a new function C_{plasma}^{drug} has to be chosen that describes the concentration of that drug in the plasma. For NBVM instead, one should introduce another parameter β_2 in addition to β_1 that represents the decay of the other drug. Taking all these things into account, we chose to continue working with NBVM as it seems to give more realistic results, it is more suitable for our data and it is a lot quicker.

6.4. Model analysis

In this section, the chemotherapy-incorporated model is analysed by evaluating the influence of various choices for the parameters, the effect of using all three MRI scans for the calibration and the influence of the slice thickness of the MRI. The results shown in this section are all made based on the data of p_1.

6.4.1. Influence of D_0

Firstly, let us analyse the influence of D_0, for which calibration is first run once. After this calibration, α and $k(\vec{x})$ are kept at the found optimal values and the model is predicted forward with different values of D_0. The results can be shown in various ways. Firstly, the resulting total number of tumour cells over time is shown in Figure 6.10a. In this figure, it can be seen that the trend in the descending number of tumour cells is the same for all values of D_0 as the lines all show similar behaviour, but as D_0 gets bigger the decrease is stronger. It is important to note that the minimisation function in calibration does not minimise the total number of tumour cells, but instead it looks at the squared differences between the measured and predicted number of tumour cells per voxel. This means that the calibration focuses on getting good results on a voxel-by-voxel basis. The sum of the squared errors that were at t_1, which is the calibration time point, and t_2, which is the validation time point, are displayed in Figures 6.10b and 6.10c respectively. The optimal value, which was $D_0 = 2.234 \cdot 10^{-4}$ indeed provides a minimum for the error function at t_1, as can be seen in Figure 6.10b. However, at t_2 this value does not yield a minimum and it can be seen that choosing a bigger value for D_0 would in that case lead to a smaller error at t_2.

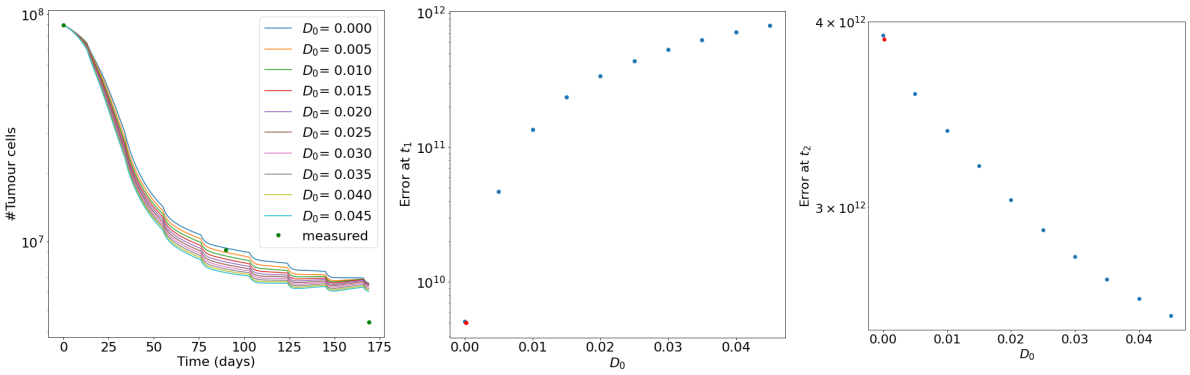

(a) Total number of tumour cells

(b) Error at t_1

(c) Error at t_2

Figure 6.10: Plots displaying the influence of D_0. On the left, the total number of tumour cells is displayed. In the middle and on the right, the sum of the squared errors at t_1 and t_2 respectively are shown. The optimal value for D_0 is displayed in red.

6.4.2. Influence of α

As a second step in the analysis of the model, the role of α is investigated. Similar to what was done in the previous section, the calibration is run once and after this the values for D_0 and $k(\vec{x})$ are kept at the optimal values and the value of α is varied. Figure 6.11 shows the results.

In Figure 6.11a the influence of α is clearly shown: when α is small, the chemotherapy plays a small role and there are little or no oscillations in the tumour cell numbers, but when α is big, then there are many increases and decreases in the number of tumour cells. For bigger values of α, the results do not necessarily seem very realistic: the total number of tumour cells oscillates and the tumour cells grow back as quickly as they are eradicated. In addition, for these values the total number of tumour cells does not go down, so it seems impossible to eradicate all cells. It is questionable if this is what actually happens or if in this case the value of α is just simply too big to describe the behaviour of chemotherapy realistically. Note that none of the curves pass through all three of the measured points.

Figure 6.11b shows that the optimal value for $\alpha = 3.705 \cdot 10^{-2}$ indeed yields a minimum at t_1 so a global minimum was found. This has been further checked by starting the calibration with various initial guesses for α. Like with D_0, this optimal value however is not the optimal value for the error at time t_2 and a bigger value would have given a smaller error at t_2.

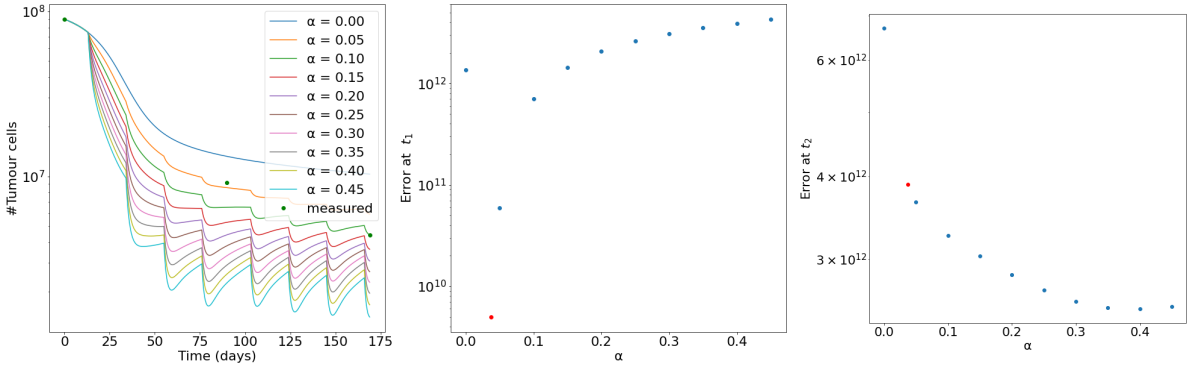

(a) Total number of tumour cells (b) Error at t_1 (c) Error at t_2

Figure 6.11: Plots displaying the influence of α. On the left, the total number of tumour cells is displayed. In the middle and on the right, the sum of the squared errors at t_1 and t_2 respectively are shown. The optimal value for α is displayed in red.

6.4.3. Influence of $k(\overline{x})$

In this section the proliferation rate $k(\overline{x})$ is analysed. It turns out that choices here not only influence the total number of tumour cells but also the spatial distribution of the tumour density. To quantify this at both the calibration (t_1) and validation (t_2), the *mean squared error* (MSE) will be used, which is calculated as follows:

$$MSE(t_i) = \frac{\sum_{\overline{x}}(N(\overline{x}, t_i) - \hat{N}(\overline{x}, t_i))^2}{n}$$

Constant proliferation rate

First let us look at what happens when the proliferation rate is the same value for all voxels, i.e. $k(\overline{x}) = k$. In that case, the optimum value found is $k = -0.04998$. This is interesting, as we would expect to have a positive proliferation rate for the model as the chemotherapy term is the death term and the proliferation thus only represents cell growth. Apparently, the cell death in the model comes both from a negative proliferation term that is constant over time and a treatment term that varies over time. As explained in Section 5.4, bounds can be defined for the parameters because the TRF algorithm is used. For this reason, calibration was run again, this time demanding all parameters to be positive. The optimal value for k in this case is $8.979 \cdot 10^{-31}$, which is extremely small and shows that in that case it is best to basically set $k = 0$.

Let us now analyse the total tumour density and the error that the model makes in these cases, which are shown in Figure 6.12. On the left, the total number of tumour cells is shown. Here, it can be seen that although both cases show different behaviour, they both pass through the first green point, meaning they give a good estimate of the total number of tumour cells in calibration, but they both underestimate the total number of tumour cells at t_2. For the first case (in blue), it can be seen that there is a strong decrease in the total number of tumour cells leading to an underestimation of the number of tumour cells at t_2 and that the curve does not show the same shape that was seen with an initial strong decline which was followed by a more gradual decline. In addition, the influence of chemo that was previously visible in the form of decreases on the days of treatment is no longer visible. This is caused by the fact that α has been calibrated to a small value. Note that the other curve (in orange) for the case with lower bound shows behaviour that is wanted: a strong decrease in tumour cell numbers when the patient is treated and almost constant behaviour when the effect of treatment has decreased. However, the effect of treatment is too strong so unfortunately it also underestimates the total number of tumour cells at t_2.

In addition to the total number of tumour cells, the absolute error at t_1 and t_2 in the middle and on the right respectively are presented for the case without a lower bound. The images for the other case were very similar and are therefore omitted. Here, it can be seen that the model in the case where k is constant for all voxels was not able to make an accurate prediction of the tumour density, as it predicts that there are still tumour cells present in places where there is no more tumour and it underestimates the number of tumour cells in the location of the tumour itself. It thus predicts that the decrease in

tumour cells is approximately the same everywhere in the tumour, while the tumour actually shrinks centrally, which means that the number of tumour cells might not decrease in the innermost part of the tumour. This high error in the tumour density at t_1 is also reflected in the MSE, which is shown in Table 6.3, as these are both a lot higher than the MSE for calibration in which the proliferation rate is determined per voxel, which is generally of order 10^6 or 10^7. The error for the case with the lower bound is higher than the case without the lower bound, which explains why the optimal value for k returned by the TRF algorithm was negative and not positive as a positive k would give a worse result.

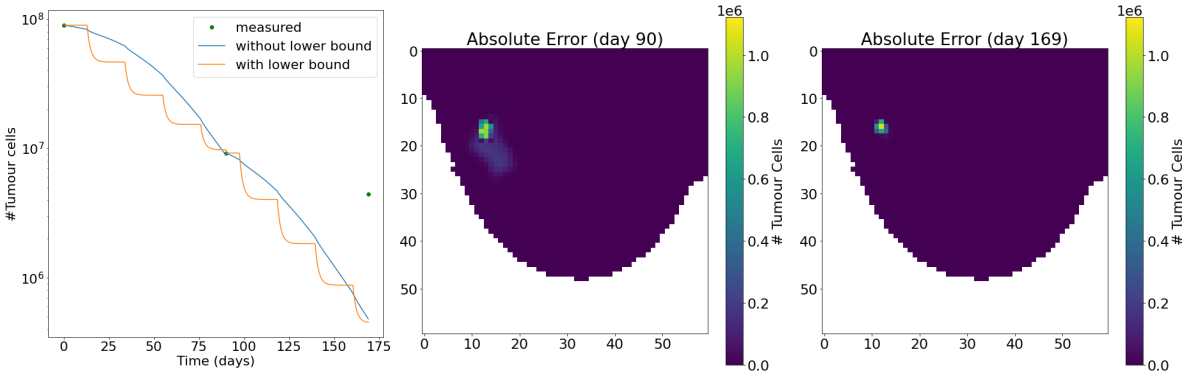

(a) Total number of tumour cells

(b) Absolute error at t_1

(c) Absolute error at t_2

Figure 6.12: Results for taking $k(\overline{x})$ constant for all voxels. On the left, the total number of tumour cells over time is displayed for the cases with and without lower bound on the parameters. In the middle and on the right, the absolute error at t_1 and t_2 respectively are shown.

This is thus a good example to show that it is important to not only look at the curve of the total number of tumour cells but also at the tumour density prediction of the model. In this case, for example the error at t_1 of the total number of tumour cells seems small, but this does not mean that the model made a good prediction. The opposite is the case, as the modelled spatial distribution is far off compared to the measured spatial distribution of the tumour cells, which could be seen in the figures displaying the absolute errors and in the MSE values. It is therefore clear that the proliferation rate should not be constant, as otherwise the model is not able to simulate the shrinkage in the way that the tumour actually shrinks and the errors made by the model are big.

Calibration	$MSE(t_1)$	$MSE(t_2)$
Without lower bound	$1.792 \cdot 10^9$	$7.702 \cdot 10^8$
With lower bound	$2.061 \cdot 10^9$	$7.976 \cdot 10^8$

Table 6.3: Mean squared errors for the calibration with and without lower bound for the case where k is taken constant for all voxels.

Proliferation rate per tissue

The model performance for the case where k is determined for each tissue type has also been investigated, which can be written as follows:

$$k(\overline{x}) = \begin{cases} k_1 & \text{for } \overline{x} \in \text{ tumour} \\ k_2 & \text{for } \overline{x} \in \text{ fibroglandular tissue} \\ k_3 & \text{for } \overline{x} \in \text{ adipose tissue} \end{cases}$$

Calibration returns $k_1 = -0.049, k_2 = -0.354, k_3 = -0.027$. Once again, the results were run in addition with lower bounds on the parameters. This yielded $k_1 = 4.659 \cdot 10^{-29}, k_2 = 1.014 \cdot 10^{-41}, k_3 = 1.528 \cdot 10^{-52}$, which are once again very small values. In Figure 6.13 on the left, the total number of tumour cells is displayed for these cases. Note that this is extremely similar to what was seen in Figure 6.12. As it turns out, also the predicted tumour densities and the MSE for both time points are similar.

This can however easily be explained. The model focuses on calculating the number of tumour cells in each voxel. Therefore, $\frac{\partial N}{\partial t}$ will only be non-zero in voxels that were non-zero at t_0 and which were thus labelled as tumorous tissue, so k_2 and k_3 will not lead to changes in the model prediction. For that reason, there is no difference in the results between having the proliferation rate calculated per tissue or having it constant for all tissue types and also explains why the value of k_1 was almost the same as the value of k. In addition, the proliferation rates are shown in Figure 6.13 in the middle and on the right for the case with and without lower bounds on the parameters respectively.

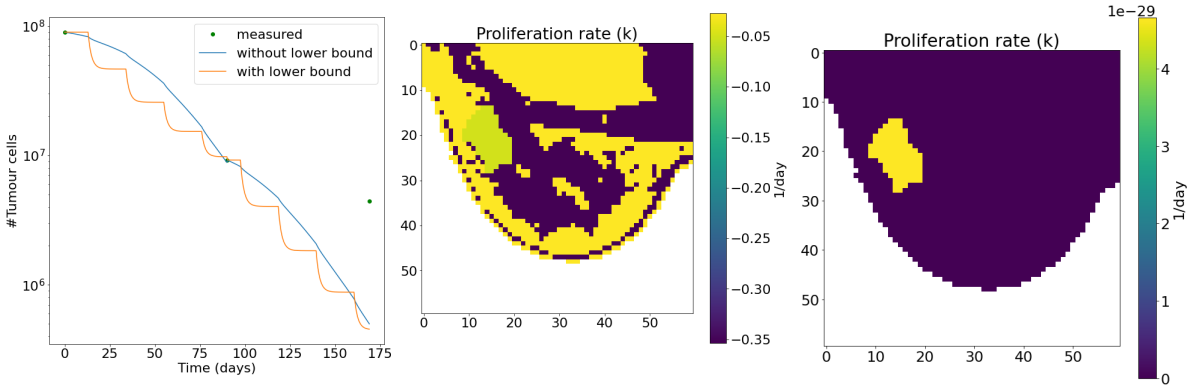

(a) Total number of tumour cells (b) $k(\overline{x})$ without lower bound (c) $k(\overline{x})$ with lower bound

Figure 6.13: Results for calibrating $k(\overline{x})$ per tissue type. On the left the total number of tumour cells over time is displayed. In the middle and on the right, the resulting proliferation map $k(\overline{x})$ is displayed for the case without lower bound and with lower bound respectively.

Proliferation rate per voxel

Lastly, $k(\overline{x})$ is calibrated for each voxel with the reduced mask $\mathcal{K}_{red}$ that was explained in Section 5.4. There are both positive and negative values for the proliferation rates, but it is worth noting that in the literature on the DIMCRD model negative values for the proliferation also occurred [7]. Out of interest, the calibration was like before also run with a lower bound on the parameters so analyse the effect. The results for these two cases are displayed in Figure 6.14. For the classical calibration, i.e. calibration without any bounds, which is displayed in blue, a small effect of the treatment can be seen in the total number of tumour cells and the model overestimates the total number of tumour cells at t_2. For the other case with a lower bound, displayed in orange, there are strong oscillations in the total number of tumour cells which is very different from the behaviour of the curve when no lower bounds are enforced. Also, the proliferation rate is quite different from the first case. Note that the colour scale is different for the proliferation rate maps.

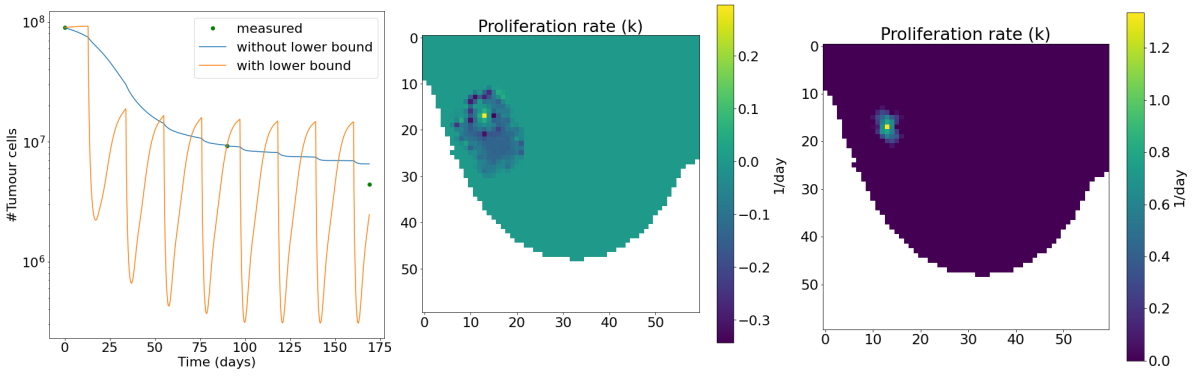

(a) Total number of tumour cells (b) $k(\overline{x})$ without lower bound (c) $k(\overline{x})$ with lower bound

Figure 6.14: Results for calibrating $k(\overline{x})$ per voxel. On the left the total number of tumour cells over time is displayed. In the middle and on the right, the resulting proliferation map $k(\overline{x})$ is displayed for the case without lower bound and with lower bound respectively.

Let us now look at the error on a local level. In Table 6.4 it can be seen that the MSE at t_1 is smaller for the case without lower bound, but the MSE at t_2 is smaller for the case with lower bound.

Calibration	$MSE(t_1)$	$MSE(t_2)$
Without lower bound	$1.380 \cdot 10^6$	$1.099 \cdot 10^9$
With lower bound	$1.462 \cdot 10^7$	$7.052 \cdot 10^8$

Table 6.4: Mean squared errors for the calibration with and without lower bound for the case where k is calibrated for each voxel.

We have thus seen that choosing $k(\overline{x})$ constant for all voxels or all tissue types leads to the same result but differs from the case where $k(\overline{x})$ is calibrated per voxel. For a constant proliferation, the model was not able to properly simulate the decay of tumour cells on a local level, which resulted in large MSE values at t_1. Both positive and negative values were observed, although these negative values can be avoided by imposing bounds on the parameters. However, in other studies, negative values also appeared for the proliferation and when a lower bound was enforced for the calibration per voxel, it resulted in strong oscillations in the total number of tumour cells, which is unwanted. A proliferation rate that is determined on a voxel-by-voxel basis is important to capture the heterogeneity of the tumour that results in different cell growth and death levels in different parts of the tumour. It thus represents an important aspect in connection to the actual dynamic process of tumour growth. Therefore, the proliferation rate is determined per voxel and no bounds will be imposed.

6.4.4. Calibration with all 3 MRI scans

In standard calibration, only the MRI scans at t_0 and t_1 are taken into account and the model is validated by calculating forward from t_1 to t_2 with the optimised parameters. It is expected that if the scan at t_2 is also given as input for the calibration, then the prediction at t_2 would improve as the model already knows the tumour density at t_2. Let us investigate if this is indeed the case so if the alternative calibration with all 3 MRI scans, gives better results compared to the standard calibration with only 2 MRI scans. Figure 6.15 shows on the left the total number of tumour cells for both calibration options. It can be seen that in using the alternative calibration, the total number of tumour cells at t_1 is overestimated but the estimated total number of tumour cells at t_2 is closer than it is for the standard calibration. Quite remarkably, the effect of chemo is not clearly visible for the alternative calibration as there are no sharp decreases in the number of tumour cells on the days on which the patient is treated, which is caused by a small calibrated value for α.

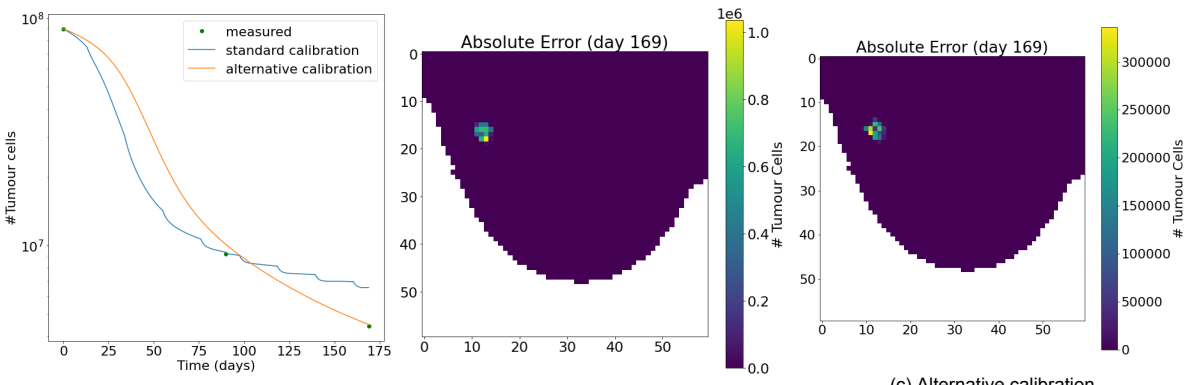

(a) Total number of tumour cells

(b) Standard calibration

(c) Alternative calibration

Figure 6.15: Results for calibration with two (standard) or three (alternative) MRI scans. On the left, the total number of tumour cells for both options is displayed. In the middle, and on the right, the absolute error at t_2 is displayed for the standard calibration and alternative calibration respectively.

As noted before, summarising the performance of the model by only displaying the total number of tumour cells is not completely fair as it leaves out information on how the model performs on a local level. Thus, the MSE values at t_1 and t_2 are compared for the standard calibration with 2 MRI scans and the alternative calibration with 3 MRI scans. The results are shown in Table 6.5, where it can be seen that the MSE at t_1 is a lot lower for the standard than for the alternative calibration option, but

the MSE at t_2 for the alternative calibration is almost a factor 10 lower than the MSE for the standard calibration.

Calibration	$MSE(t_1)$	$MSE(t_2)$
Standard calibration	$1.380 \cdot 10^6$	$1.099 \cdot 10^9$
Alternative calibration	$1.546 \cdot 10^8$	$1.278 \cdot 10^8$

Table 6.5: Mean squared errors for the standard calibration with 2 MRI scans and the alternative calibration with 3 MRI scans.

From this case study, it can be concluded that when the third MRI scan is also taken into account, the prediction at t_2 improves but the prediction at t_1 is less good. What would be interesting to see in the future is, when four MRI scans are available for a patient, if having three MRI scans for calibration improves the prediction for the fourth MRI scan.

6.4.5. Influence of slice thickness

So far the slice thickness, which will be denoted as Δz, was not varied and was always equal to the slice thickness of the DCE scans ($\Delta z = 1.6$ mm). In previous work, it was found that for this slice thickness, the model prediction of the MCRD model was not significantly different from the basic RD model [11]. Therefore, so far the DIRD model was used because it was not expected that the results would differ much from the DIMCRD model and the DIRD model is much faster in its calculations. In this section, the slice thickness is increased and the influence of the mechanics is analysed.

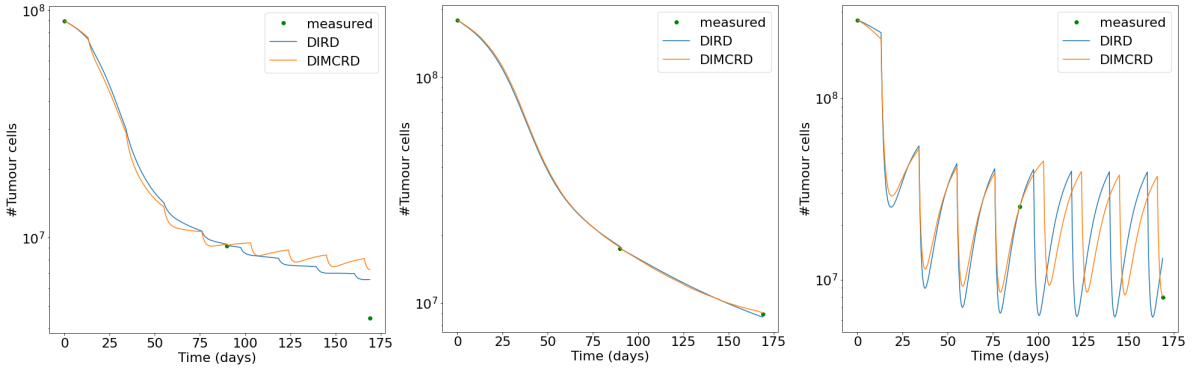

(a) $\Delta z = 1.6$ mm (b) $\Delta z = 3.2$ mm (c) $\Delta z = 4.8$ mm

Figure 6.16: Total number of tumour cells for both the DIRD and the DIMCRD model for different slice thicknesses Δz. Note the different scales on the tumour cell axis.

In Figure 6.16 the total number of tumour cells for both the DIRD and DIMCRD model is shown for slice thicknesses of $1.6, 3.2$ and 4.8 mm. As expected, the total number of measured tumour cells increases as the slice thickness increases, which is logical as the tumour will in general be thicker than just 1.6 mm. What immediately stands out is that for $\Delta z = 1.6$ mm there is quite a difference between the DIRD and DIMCRD model, but this was not expected. Apparently, when chemotherapy is included, there is a difference between the model with and without mechanics, even for this small slice thickness. The number of tumour cells for the DIMCRD model is higher than for the DIRD model after calibration. In the middle, the results are shown for a slice thickness of 3.2 mm. In this case, calibration returned a small value for α, which means that the influence of chemotherapy is not visible anymore and thus the results for both models are similar. On the right, for $\Delta z = 4.8$ mm, it can be seen that there are strong increases and decreases in the number of tumour cells for both models. It is the type of behaviour that was seen before as well, in which the tumour cells grow back as quick as they are killed. Note that the decreases for DIRD are stronger than for DIMCRD and the peaks are all approximately at the same height. which means that most likely because of the mechanics the number of tumour cells did not decrease as hard as it could for the model without mechanics. Thus, the mechanics limit the cell death, which could also be seen similarly in the left figure where the blue line of DIRD stays under the orange line of DIMCRD.

Δz	model	$MSE(t_1)$	$MSE(t_2)$
1.6 mm	DIRD	$1.380 \cdot 10^6$	$1.099 \cdot 10^9$
	DIMCRD	$1.398 \cdot 10^6$	$1.089 \cdot 10^9$
3.2 mm	DIRD	$3.389 \cdot 10^7$	$2.774 \cdot 10^9$
	DIMCRD	$3.818 \cdot 10^7$	$3.406 \cdot 10^9$
4.8 mm	DIRD	$4.540 \cdot 10^7$	$3.451 \cdot 10^9$
	DIMCRD	$4.644 \cdot 10^7$	$1.721 \cdot 10^9$

Table 6.6: Mean squared errors for different slice thicknesses and various models for p_1.

In Table 6.6, the mean squared errors for these cases are presented, where it can be seen that the mean squared error increases as the slice thickness gets bigger. This is logical, as bigger voxels contain more tumour cells and thus the errors increase. The MSE at t_2 of DIMCRD is however does not follow this trend and turns out lower than expected. Also, note that the MSE at t_1 for 1.6 mm is smaller for DIMCRD than for DIRD, but for the other cases the MSE is bigger for DIMCRD than for DIRD. Furthermore, for 1.6 and 4.8 mm, the MSE at t_2 is smaller for DIMCRD than for DIRD, but it is the other way around for 3.2 mm.

Let us now reflect on the choice of slice thickness. In previous work, it was observed that for $\Delta z = 1.6$ mm, there was no difference between the model without mechanics (RD) and the model with mechanics (MCRD) [11]. This is why the slice thickness in that research was increased and this resulted in different outcomes for the RD and MCRD models. However, for the DIRD and DIMCRD models, a difference can already be observed for the small slice thickness. In addition, the curves for this slice thickness showed behaviour that was more in line with what was expected: the influence of chemotherapy was clear, the increases and decreases were not very big and in addition the MSE values were all relatively small. Note however that this last observation was most likely caused by the fact that less tumour cells were present compared to the thicker slices. All in all, it was decided to use $\Delta z = 1.6$ mm in the remainder of this chapter for the results of the other patients.

6.5. Results and comparison of models

In this section, the results will be summarised for the different models and patients. We will analyse the total number of tumour cells over time, the parameter values and various measures that were chosen to quantify the results. The aim is to have a model that can accurately predict for each position in the breast how many tumour cells are present, which means that the local error should be small. For this, the previously introduced mean squared error (MSE) will be used. If the model makes proper predictions on a local level, then the sum over the predicted tumour cells, denoted by $S(t_i) = \sum_{\overline{x}} N(\overline{x}, t_i)$ should be close to the sum over the measured tumour cells, denoted by $\hat{S}(t_i) = \sum_{\overline{x}} \hat{N}(\overline{x}, t_i)$. In previous sections, these values have been plotted to evaluate the different cases as a way to summarise the behaviour of the model on a global scale. To quantify this at t_1 and t_2, the *global relative error* (GRE) will be used. The GRE value represents the relative difference between the sum of the modelled tumour densities and the sum of the measured tumour densities. It is calculated using the following formula:

$$GRE(t_i) = \frac{|S(t_i) - \hat{S}(t_i)|}{S(t_i)}$$

So far the MSE has been introduced to assess the local error and the GRE has been introduced to assess the global error of the model. In addition to these error measures, the *concordance correlation coefficient* (CCC) will also be used to quantify the results. This coefficient is a value between 0 and 1 and it measures the agreement between two sets of data. It has also been used in papers related to using mechanical models to predict tumour growth [7, 8, 14] and thus allows us to compare values. It is calculated using the mean, the variance, covariance and the correlation coefficient:

$$CCC(t_i) = \frac{2 \cdot \rho \cdot \sigma(N(\overline{x}, t_i)) \cdot \sigma(\hat{N}(\overline{x}, t_i))}{\sigma^2(N(\overline{x}, t_i)) + \sigma^2(N(\overline{x}, t_i)) + \frac{1}{N^2}(S(t_i) - \hat{S}(t_i))^2}$$

Here, σ corresponds to the standard deviation and ρ is the Pearson product-moment correlation coefficient, which can be computed by calculating the covariance of $N(\overline{x}, t_i)$ and $\hat{N}(\overline{x}, t_i)$ and dividing this

by the product of their standard deviations.

Now that the measures by which the results will be quantified are introduced, we can move on to present the results of all models for all patients. Note that for p_2 the DCE scan of t_1 instead of t_0 was used to calculate the chemotherapy term as the scan of t_0 was made at a different hospital and was not of the required form.

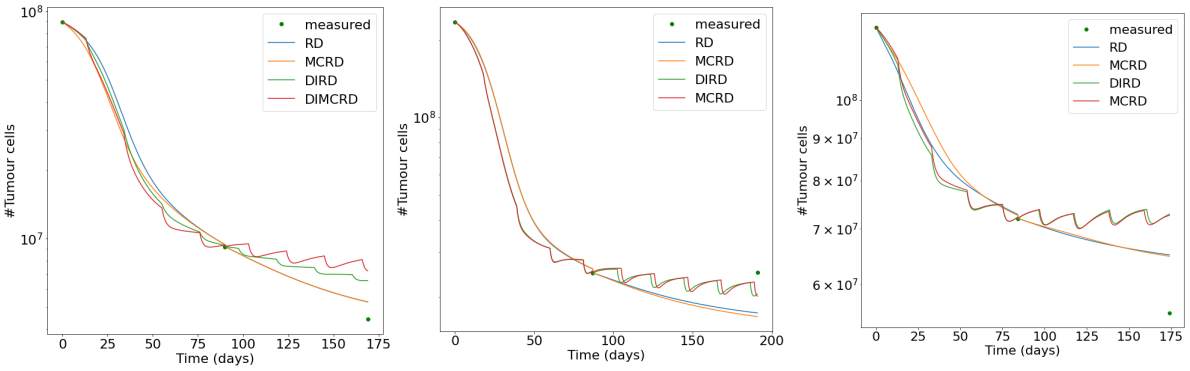

(a) p_1 (b) p_2 (c) p_3

Figure 6.17: Total number of tumour cells for all patients and all models.

Firstly, let us analyse the behaviour of the models over time by looking at the curves that describe the total number of tumour cells, for all models and patients, which are shown in Figure 6.17. In previous research, it was already discussed that the results for RD and MCRD are very similar when a small slice thickness is used, which can also be seen here. For p_1 it was already observed that there is quite a difference between the curves of the DIRD and the DIMCRD models but this difference is smaller for the other patients. In addition, it can be seen that for all patients the curves describing the total number of tumour cells of the chemotherapy models (DIRD and DIMCRD) are higher than the ones of the models without treatment term (RD and MCRD), meaning there is a smaller decay in the number of tumour cells for the chemotherapy models. In the case of p_2, this is beneficial as the models without chemotherapy underestimated the total number of tumour cells, but for p_1 and p_3 it is the other way around, resulting in an overestimate of the number of tumour cells. Furthermore, it is interesting to see for p_3 that the number of tumour cells seems to increase towards t_2 according to the chemotherapy models, while this does not correspond to the measured data. In addition, for this patient the behaviour of the non-mechanical (RD and DIRD) and mechanical (MCRD and DIMCRD) models differ between t_0 and t_1 but there is almost no visible difference between t_1 and t_2.

		D_0	α	mean $k(\overline{x})$	$\min_{\overline{x}} k(\overline{x})$	$\max_{\overline{x}} k(\overline{x})$
p_1	RD	$2.733 \cdot 10^{-3}$	-	$-3.548 \cdot 10^{-3}$	-0.426	0.293
	MCRD	$4.289 \cdot 10^{-3}$	-	$-4.034 \cdot 10^{-3}$	-0.666	0.363
	DIRD	$2.234 \cdot 10^{-3}$	$3.705 \cdot 10^{-2}$	$-5.243 \cdot 10^{-3}$	-0.344	0.296
	DIMCRD	$4.398 \cdot 10^{-3}$	$9.064 \cdot 10^{-2}$	$-4.431 \cdot 10^{-3}$	-0.478	0.469
p_2	RD	$5.143 \cdot 10^{-3}$	-	$-5.780 \cdot 10^{-3}$	-0.452	0.295
	MCRD	$5.081 \cdot 10^{-3}$	-	$-4.836 \cdot 10^{-3}$	-0.390	0.220
	DIRD	$2.972 \cdot 10^{-3}$	0.280	$-4.008 \cdot 10^{-3}$	-0.695	0.781
	DIMCRD	$3.465 \cdot 10^{-3}$	0.263	$-5.620 \cdot 10^{-3}$	-0.680	0.819
p_3	RD	$2.789 \cdot 10^{-3}$	-	$-3.754 \cdot 10^{-3}$	-0.581	0.227
	MCRD	$4.780 \cdot 10^{-4}$	-	$-2.493 \cdot 10^{-3}$	-0.361	0.316
	DIRD	$3.401 \cdot 10^{-4}$	$3.867 \cdot 10^{-2}$	$-6.800 \cdot 10^{-4}$	-0.819	0.283
	DIMCRD	$4.426 \cdot 10^{-4}$	$3.927 \cdot 10^{-2}$	$2.150 \cdot 10^{-4}$	-0.418	0.283

Table 6.7: Optimised parameter values for all models and patients.

In Table 6.7 the calibrated parameter values are summarised, where for the proliferation rate $k(\overline{x})$ the mean, minimum and maximum values are displayed. It turns out that the minimum is always neg-

ative and the maximum is always positive, indicating that there are both negative and positive values. The mean is always very small and in all cases but one the mean is negative. It can be observed for each parameter that it has approximately the same order for the models and patients and there are no extremely high or low values. This is an improvement compared to previous research, in which the value of for example D_0 varied greatly between the order of 10^{-11} to 10^{-3} for different patients and different models [11]. This was probably caused by the Tikhonov regularisation term that was used to overcome the issue of the under-determined problem. As this issue was solved in another way with the reduced mask, it seems like this has improved the model in the sense that there is more similarity in the parameter values. There is however still some variation in these parameter values, which is good as the aim is to have a model with patient-specific parameters.

		$MSE(t_1)$	$MSE(t_2)$	$GRE(t_1)$	$GRE(t_2)$	$CCC(t_1)$	$CCC(t_2)$
p_1	RD	$2.041 \cdot 10^6$	$1.036 \cdot 10^9$	$2.069 \cdot 10^{-2}$	0.190	0.999	0.490
	MCRD	$2.032 \cdot 10^6$	$1.035 \cdot 10^9$	$2.001 \cdot 10^{-2}$	0.191	0.999	0.490
	DIRD	$1.380 \cdot 10^6$	$1.099 \cdot 10^9$	$1.364 \cdot 10^{-2}$	0.480	1.000	0.503
	DIMCRD	$1.398 \cdot 10^6$	$1.089 \cdot 10^9$	$1.382 \cdot 10^{-2}$	0.632	1.000	0.518
p_2	RD	$2.510 \cdot 10^7$	$3.263 \cdot 10^9$	$3.803 \cdot 10^{-2}$	0.303	0.998	0.670
	MCRD	$2.528 \cdot 10^7$	$3.328 \cdot 10^9$	$3.824 \cdot 10^{-2}$	0.326	0.998	0.662
	DIRD	$2.198 \cdot 10^7$	$3.186 \cdot 10^9$	$1.985 \cdot 10^{-2}$	0.174	0.998	0.694
	DIMCRD	$2.139 \cdot 10^7$	$3.174 \cdot 10^9$	$1.933 \cdot 10^{-2}$	0.191	1.000	0.478
p_3	RD	$7.624 \cdot 10^6$	$8.060 \cdot 10^9$	$1.167 \cdot 10^{-2}$	0.175	1.000	0.624
	MCRD	$6.486 \cdot 10^6$	$8.297 \cdot 10^9$	$9.183 \cdot 10^{-3}$	0.171	1.000	0.618
	DIRD	$1.990 \cdot 10^6$	$8.469 \cdot 10^9$	$3.083 \cdot 10^{-3}$	0.316	1.000	0.592
	DIMCRD	$2.029 \cdot 10^6$	$8.468 \cdot 10^9$	$3.275 \cdot 10^{-3}$	0.312	1.000	0.592

Table 6.8: Mean squared errors, global relative errors and concordance correlation coefficient for t_1 and t_2 for all models and patients.

Lastly, the performance of the models is assessed with the introduced MSE, GRE en CCC values, which are shown in Table 6.8 for both t_1 and t_2. The values at t_1 are shown here, as it is also interesting to compare the performance of the models at calibration. For t_1, it can be seen that in general the DIRD and DIMCRD models perform better than the RD and MCRD models: the MSE and GRE values are lower and the CCC values are higher. This is also logical, as in the calibration the sum of the voxel-wise squared difference between the measured and modelled tumour number is minimised, which is quite similar to the MSE. Thus, if the MSE of the RD and MCRD models were lower than the ones of DIRD and DIMCRD, then the calibration should yield $\alpha = 0$ as this would in that case reduce the squared error and it simplifies those models to the RD and MCRD models. In addition, all CCC values are almost equal to 1, which means that the predicted tumour density is very close to the actual tumour density, as expected in calibration.

For t_2 it differs per patient which type of model performs better. In most cases, it even depends on which measure is being looked at which model is best. For example for p_1, the MSE, GRE and CCC values of RD and MCRD are extremely similar and are all better compared to the chemotherapy models. From the curve in Figure 6.17a, it could already be seen that on a global level the RD and MCRD models performed better and thus that their GRE values would be lower compared to DIRD and DIMCRD models. For those chemotherapy models, it can be seen that although the GRE value of DIMCRD is quite a lot higher, it gives better MSE and CCC values compared to the DIRD model. Thus, looking at the MSE and GRE, the models without the chemotherapy term perform better, but looking at the CCC value, the DIMCRD model performs best for this patient.
Next, let us take a look at p_2. Here, the chemotherapy models seem to outperform the models without treatment in almost all aspects except for the CCC value of DIMCRD, which is surprisingly low in comparison to the other CCC scores for this patient. The DIRD model performs exceptionally well for this patient, with the second lowest MSE, lowest GRE and highest CCC value out of all models and patients.
For p_3 quite similar behaviour can be seen compared to p_1. The RD and MCRD models outperform the DIRD and DIMCRD models in all aspects; even the CCC value is higher. The RD model seems best

here, as it has the lowest MSE and highest CCC despite its slightly higher GRE value compared to MCRD. The chemotherapy models perform very comparably, which is what was also concluded from Figure 6.17c, but the DIMCRD model is slightly better in terms of MSE and GRE.

Lastly, before this chapter is concluded, we would also like to compare our CCC values of t_2 to the ones reported on by Jarrett et al. [7]. Their study included five patients of which there was only one HER2+, the others were HER2-. The found CCC values ranged from 0.05 to 0.50 for the MCRD and from 0.08 to 0.51 for the DIMCRD model, with a median of 0.27 and 0.33 respectively. For all five patients, the CCC value of DIMCRD was higher than the one of MCRD. For this study, the CCC values for MCRD lie between 0.490 and 0.662 and for DIMCRD they lie between 0.478 and 0.592. The CCC values for our patients are thus quite a lot higher than the values that were presented by Jarrett et al. However, in our case the CCC value of DIMCRD was higher than the MCRD value for only one out of three patients.

In summary, the performance of the models has been evaluated and their outcomes have been compared. It depended on the measure and the patient which model performed best and it was not clear which model performed best overall. However, we did see that in general the models that included the chemotherapy performed better at t_1, but for t_2 it was not possible to draw such a conclusion. In most cases, including mechanics did not give big differences compared to the standard models. However, the computation time for the MCRD and DIMCRD models was much larger than that of RD and DIRD. It is thus the question if including the mechanics is worth the extra effort. Computing the chemotherapy curves required some extra time before the normal computation, but it did not influence the time that was needed for calibration, which is the bottleneck of the implementation.

7

Three-dimensional extension

In this chapter, steps are taken to extend from a two-dimensional to a three-dimensional model. In the previous chapter, we have explained how the chemotherapy term can be calculated and the resulting two-dimensional model was analysed for various cases and different models. We noticed that the models that included mechanics (MCRD and DIMCRD) took a lot longer than the models without mechanics (RD and DIRD) and their results often did not differ much. By extending into another dimension, the calibration time increases greatly. For that reason, only the RD and DIRD models will be considered in 3D as it is currently infeasible to use MCRD and DIMCRD.

For the two-dimensional model, one slice was chosen from pre-processed data. For the three-dimensional extension, it would in theory be possible to consider all slices of the pre-processed data. In the case of p_1 and p_3, this would result in a total array of size $(60, 60, 120)$ and for p_2 an array of size $(70, 70, 86)$, meaning the number of computations is huge compared to the 2D model. For that reason, not all 120 slices, or 86 in the case of p_2, are considered. Instead, only 3 slices will be considered, as this number turned out to give tolerable computation times. The middle slice is corresponding to the slice that was chosen in 2D and the other slices are the ones above and below that central slice.

In this chapter, the possibilities to work with the 3D model are investigated. For this, firstly the discretisations are updated in Section 7.1. Next, the influence of the slice thickness for the 3D model is analysed in Section 7.2. In addition, the option to decrease the number of voxels in the grid by downsampling the (x, y) plane is explored in Section 7.3 and its results and computation time are compared to the standard grid. Next, in Section 7.4 a comparison is made between having a thick slice in 2D and having three thin slices that cover the same area in 3D. Lastly, results for the 3D implementation for all patients are presented in Section 7.5.

7.1. Discretisations

Now that there is an extra dimension, the discretisations and boundary conditions should be updated. Because only the simple models without mechanics are considered, only the discretisation of the reaction-diffusion equation has to be updated.

$$\begin{aligned}\frac{\partial N_{i,j,k}}{\partial t} = &\frac{D_{i+\frac{1}{2},j,k}\dfrac{\partial N_{i+\frac{1}{2},j,k}}{\partial x} - D_{i-\frac{1}{2},j,k}\dfrac{\partial N_{i-\frac{1}{2},j,k}}{\partial x}}{\Delta x} + \frac{D_{i,j+\frac{1}{2},k}\dfrac{\partial N_{i,j+\frac{1}{2}}}{\partial y} - D_{i,j-\frac{1}{2},k}\dfrac{\partial N_{i,j-\frac{1}{2}}}{\partial y}}{\Delta y} \\ &+ \frac{D_{i,j,k+\frac{1}{2}}\dfrac{\partial N_{i,j,k+\frac{1}{2}}}{\partial z} - D_{i,j,k-\frac{1}{2}}\dfrac{\partial N_{i,j,k-\frac{1}{2}}}{\partial z}}{\Delta z} + k_{i,j,k}N_{i,j,k}\left(1 - \frac{N_{i,j,k}}{\theta}\right) - \alpha C_{i,j,k}N_{i.j,k}\end{aligned} \tag{7.1}$$

In addition to the already existing boundary conditions, homogeneous Neumann boundary conditions are imposed for the $z-$direction. It is thus implicitly assumed that the tumour cells remain within the selected slices and do not diffuse to the slices outside of the domain. This is a simplifying assumption

because the tumour in most cases is not completely covered by those three slices. Writing out Equation 7.1 using central differences and applying Forward Euler, the discretisation given in 7.2 is obtained.

$$
\begin{aligned}
N_{i,j,k}^{m+1} = N_{i,j,k}^{m} \\
&+ \Delta t \Bigg(\frac{1}{2\Delta x^2} \Big(\big(D_{i,j,k} + D_{i-1,j,k}\big) N_{i-1,j,k}^{m} - \big(D_{i-1,j,k} + 2D_{i,j,k} + D_{i+1,j,k}\big) N_{i,j,k}^{m} + \big(D_{i,j,k} + D_{i+1,j,k}\big) N_{i+1,j,k}^{m} \Big) \\
&+ \frac{1}{2\Delta y^2} \Big(\big(D_{i,j,k} + D_{i,j-1,k}\big) N_{i,j-1,k}^{m} - \big(D_{i,j-1,k} + 2D_{i,j,k} + D_{i,j+1,k}\big) N_{i,j,k}^{m} + \big(D_{i,j,k} + D_{i,j+1,k}\big) N_{i,j+1,k}^{m} \Big) \\
&+ \frac{1}{2\Delta z^2} \Big(\big(D_{i,j,k} + D_{i,j,k-1}\big) N_{i,j,k-1}^{m} - \big(D_{i,j,k-1} + 2D_{i,j,k} + D_{i,j,k+1}\big) N_{i,j,k}^{m} + \big(D_{i,j,k} + D_{i,j,k+1}\big) N_{i,j,k+1}^{m} \Big) \\
&+ k_{i,j,k} N_{i,j,k}^{m} \Big(1 - \frac{N_{i,j,k}^{m}}{\theta} \Big) - \alpha C_{i,j,k}^{m} N_{i.j,k}^{m} \Bigg)
\end{aligned}
\tag{7.2}
$$

7.2. Influence of slice thickness

Like for the 2D model, a choice has to be made for the slice thickness. In 3D, this could be more important than in 2D due to the interactions between the slices. Having thick slices means that there are more tumour cells per voxel, which creates a bigger difference between the voxels with tumour cells and the voxels without any tumour cells compared to thin slices. The advantage of thick slices on the other hand is that a larger area is considered, so fewer slices are needed to cover the entire breast region.

In Figure 7.1 the total number of tumour cells for different slice thicknesses is displayed for p_1. Just like for the 2D case, note that the scales of the tumour cell axis are different and that the number of tumour cells increases as the slice thickness increases. All models and slice thicknesses result in an overestimation. For $\Delta z = 3.2$ and $\Delta z = 4.8$ mm, the DIRD model outperforms the RD model regarding this aspect, but for $\Delta z = 1.6$ mm it is the other way around. Just like for the 2D case, for $\Delta z = 3.2$ mm the effect of chemotherapy is not clearly visible as there are no decreases on the days of treatment. However, the curves of the RD and DIRD differ quite a lot and the DIRD model gives a better prediction.

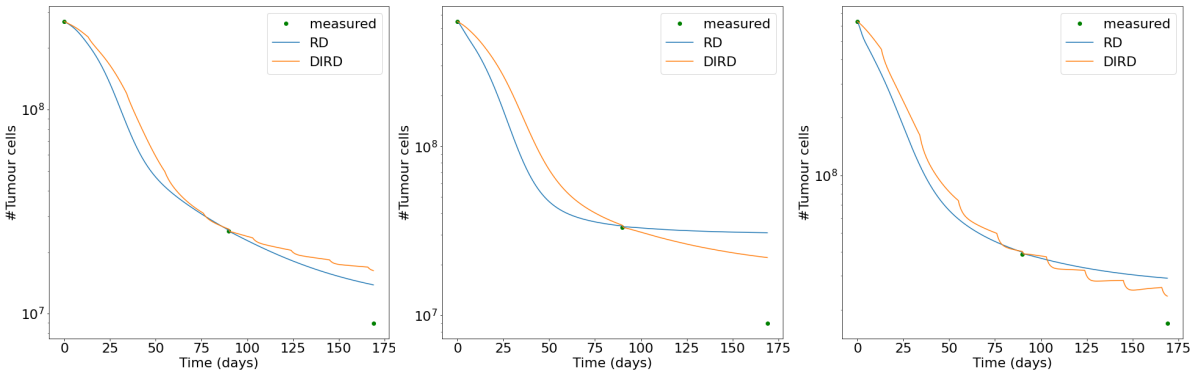

(a) $\Delta z = 1.6$ mm (b) $\Delta z = 3.2$ mm (c) $\Delta z = 4.8$ mm

Figure 7.1: Total number of tumour cells for the RD and DIRD model in 3D for different slice thicknesses Δz.

Once again, the local errors are quantified through the MSE, as displayed in Table 7.1. Interestingly enough, for $\Delta z = 1.6$ mm, the MSE of DIRD is bigger than RD for both t_1 and t_2. For $\Delta z = 3.2$ and $\Delta z = 4.8$ mm, the MSE at t_1 of DIRD is bigger, but the MSE at t_2 is smaller compared to RD. It is surprising to see these MSE values of t_1 because in the 2D case it was observed that the chemotherapy models in general had a lower MSE at t_1 than the standard models. The orders of these errors are however comparable to the 2D results. Since for $\Delta z = 4.8$ mm the influence of chemotherapy is clearly

visible and the DIRD model seems like an improvement compared to RD, this thickness is also used in the next section and the results for the other patients.

Δz	model	$MSE(t_1)$	$MSE(t_2)$
1.6 mm	RD	$9.463 \cdot 10^5$	$1.244 \cdot 10^9$
	DIRD	$1.410 \cdot 10^6$	$1.315 \cdot 10^9$
3.2 mm	RD	$3.355 \cdot 10^6$	$3.602 \cdot 10^9$
	DIRD	$3.361 \cdot 10^6$	$2.838 \cdot 10^9$
4.8 mm	RD	$5.487 \cdot 10^6$	$3.949 \cdot 10^9$
	DIRD	$6.635 \cdot 10^6$	$3.501 \cdot 10^9$

Table 7.1: Mean squared errors for different slice thicknesses and various models for p_1.

7.3. Downsampled (x, y) plane

Currently, only three slices are considered for the 3D implementation, but this means that a large part of the breast and certain parts of the tumour are not included. To model the entire tumour, more slices should be considered, so therefore it is interesting to investigate options to decrease the computation time, which in this section will be done by downsampling the (x, y) plane. Before going into that, let us make some remarks on other options that were considered. In the previous chapter, the influence of the proliferation rate has been investigated, where also the option to have a constant proliferation for all voxels was researched. Having only one value for $k(\vec{x})$ of course greatly decreases the calibration time, but it turned out that because of this the model was no longer able to make accurate predictions of the tumour density on a local level, which resulted in big MSE values. In 3D this option was also looked into, but this gave the same issues that were addressed before. Another option that was considered, was relaxing the convergence criterion of the TRF algorithm in calibration. This was possible, but the results deteriorated a lot which is why that option was also rejected. Therefore, it was decided to instead investigate another option to speed up the computations, namely downsampling the (x, y) plane. Note that the data that was used previously had already been downsampled by a factor three and this is now increased to a factor six. This means each slice consists of a $(30, 30)$ grid which used to be a $(60, 60)$ grid.

Like before, both the total number of tumour cells and the MSE values are compared for the standard grid and this downsampled grid. In Figure 7.2, it can be seen that the measured number of tumour cells remains the same while the curves for these different grids vary. What stands out is that the error at t_1 in the number of tumour cells for the downsampled grid is very large for both RD and DIRD. This is also reflected in the MSE values in Table 7.2, where the MSE at t_1 is of order 10^8 while for the normal grid it is of order 10^6. Although the final points of the curves seem to end around the same height as they did for the normal grid, the MSE values at t_2 are a factor 10 bigger for the downsampled grid. Note also that there are no clear decreases on the days of treatment for the DIRD model applied to the downsampled grid, but still the RD and DIRD models show different curves. It is however important to note that the computation time of the downsampled grid was considerably lower than that of the normal grid: the calibration for the normal grid took almost six times as long as the calibration for the downsampled grid.

Grid	model	$MSE(t_1)$	$MSE(t_2)$
Normal grid	RD	$5.487 \cdot 10^6$	$3.949 \cdot 10^9$
	DIRD	$6.635 \cdot 10^6$	$3.501 \cdot 10^9$
Downsampled grid	RD	$4.286 \cdot 10^8$	$3.991 \cdot 10^{10}$
	DIRD	$5.626 \cdot 10^8$	$3.510 \cdot 10^{10}$

Table 7.2: Mean squared errors for normal and downsampled grid and various models for p_1.

The goal here was to see if with a downsampled grid proper results could still be obtained so that in the future perhaps this method could be used to decrease the computations when the full breast region is considered. However, even though the computation time went down considerably, the results were

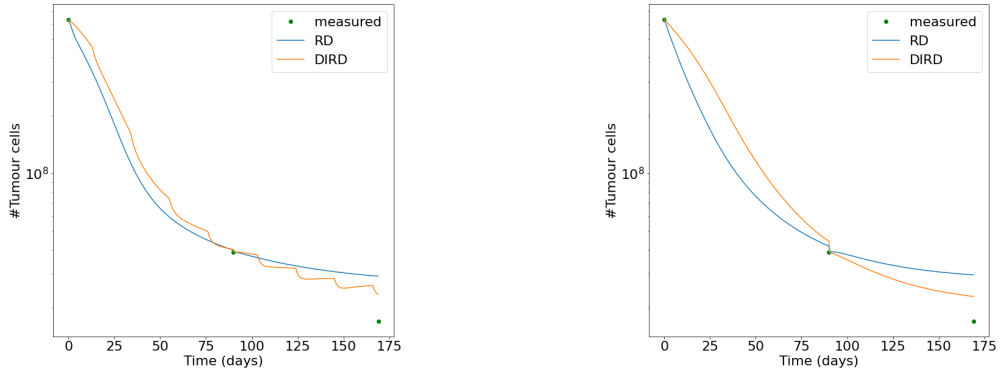

(a) Normal grid

(b) Downsampled grid

Figure 7.2: Comparison of the total number of tumour cells for the normal grid and the downsampled grid.

not good. In calibration, the error was a lot larger than the error for the normal grid and also in validation the model performed a lot worse compared to the normal grid. It thus seems like too much information is lost and that this is not an appropriate measure to decrease the number of computations.

7.4. Comparison of 3D model versus 2D model

In this section a comparison is made between the result of the 2D model with a thick slice and the 3D model with 3 thin slices. The aim is to use the same physical region within the breast and compare the outcome of the 2D model that just has one slice of 4.8 mm and the outcome of the 3D model with three slices of 1.6 mm.

The results presented in Figure 7.3 and Table 7.3 are based on the data of p_1. For the 2D simulation, all MSE values are higher than the ones found for the 3D simulation. Note however that the MSE values at t_2 are of the same order, but there is quite a big difference between the values at t_1 of 2D and 3D. The local errors of the 3D model thus increased a lot more between t_1 and t_2 than they did for 2D. Also, in the 2D simulation, the DIRD model predicted heavy oscillations that are not at all visible in the 3D case. Note also the difference between curves of the RD model in 2D and in 3D, which for 3D results in a better approximation on both a global and local level. All in all, it seems like the 3D model gives better results than the 2D model for this use case. Note however that only one patient was considered, so the results might differ for the other patients. Furthermore, the computation time of the 3D implementation was considerably longer than the computation time of the 2D implementation, which also poses the question of whether the small improvements that were seen for the 3D model are worth the extra computation time.

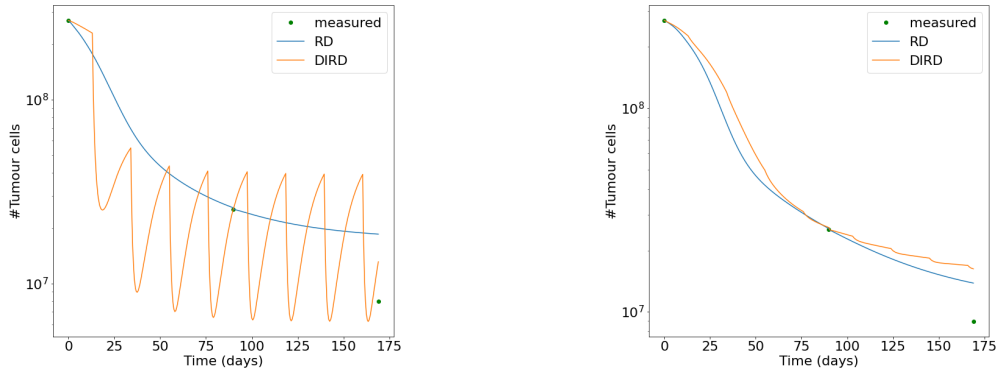

(a) 2D (4.8 mm)

(b) 3D (3 slices of 1.6 mm)

Figure 7.3: Comparison of the total number of tumour cells for the 2D model with a thick slice of 4.8 mm and the 3D model with 3 slices of 1.6 mm.

	Model	$MSE(t_1)$	$MSE(t_2)$
2D (1 slice of 4.8 mm)	RD	$5.900 \cdot 10^7$	$6.528 \cdot 10^9$
	DIRD	$4.540 \cdot 10^7$	$3.451 \cdot 10^9$
3D (3 slices of 1.6 mm)	RD	$9.463 \cdot 10^5$	$1.244 \cdot 10^9$
	DIRD	$1.410 \cdot 10^6$	$1.315 \cdot 10^9$

Table 7.3: Mean squared errors for t_1 and t_2 for the two-dimensional model with a thick slice and the three-dimensional model with three thin slices.

7.5. Results and comparison of models

Let us now present and analyse the performance of RD and DIRD in 3D for all patients. In Figure 6.17 the total number of tumour cells are shown. The results for p_1 and p_2 seem quite good as both curves of RD and DIRD go through the measured point at t_1 and get quite close to the measured total number of tumour cells at t_2. Note that for p_2 in 2D all models made an underestimation but for 3D RD and DIRD instead overestimate the total number of tumour cells at t_2. For p_3 both models do not seem to be able to make a proper prediction and the DIRD model shows strong oscillations that do not go down over time.

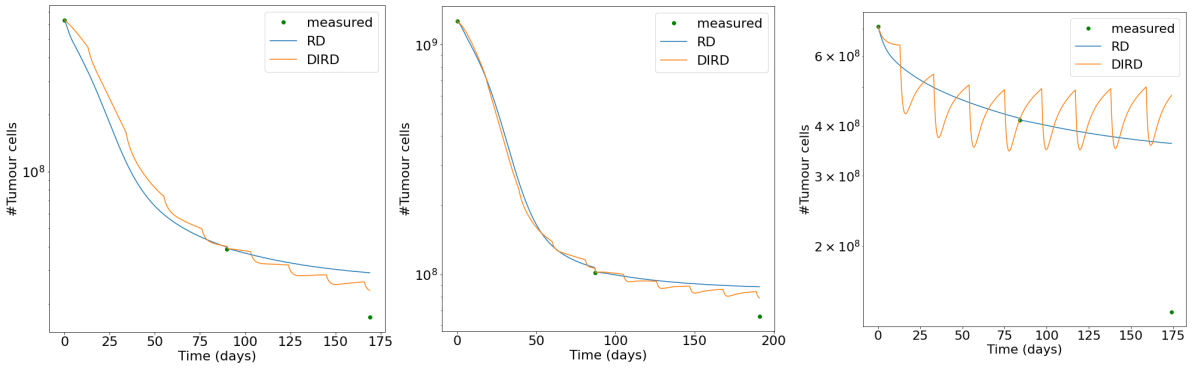

(a) p_1 (b) p_2 (c) p_3

Figure 7.4: Total number of tumour cells of the RD and DIRD models in 3D for all patients.

The optimised parameter values are summarised in Table 7.4. Here, it stands out that for p_3, D_0 is a lot smaller than for the other patients and models and α is relatively big, which explains the heavy oscillations that can be seen for this patient. In 2D the proliferation rate stayed within the range $(-1, 1)$, but for the 3D case, larger values are observed. A possible explanation is that the slices are three times as thick as they were for the 2D case, meaning there can be up to three times as many tumour cells in one voxel, i.e. θ is a lot higher. As the proliferation rate is determined per voxel, this could have led to higher proliferation rates as it is part of the reaction term in the modelling equations.

		D_0	α	mean $k(\overline{x})$	$\min_{\overline{x}} k(\overline{x})$	$\max_{\overline{x}} k(\overline{x})$
p_1	RD	$4.742 \cdot 10^{-2}$	-	$-1.232 \cdot 10^{-2}$	-4.047	1.854
	DIRD	$1.892 \cdot 10^{-2}$	$7.154 \cdot 10^{-2}$	$-4.344 \cdot 10^{-3}$	-0.735	1.059
p_2	RD	$4.224 \cdot 10^{-2}$	-	$-8.070 \cdot 10^{-3}$	-2.023	2.524
	DIRD	$1.980 \cdot 10^{-2}$	$3.595 \cdot 10^{-2}$	$-5.617 \cdot 10^{-3}$	-1.323	1.775
p_3	RD	$2.422 \cdot 10^{-2}$	-	$-8.157 \cdot 10^{-3}$	-1.452	0.506
	DIRD	$1.763 \cdot 10^{-4}$	0.299	$-2.434 \cdot 10^{-3}$	-2.961	1.640

Table 7.4: Optimised parameter values of the RD and DIRD models in 3D for all patients.

The same measures as before are used to quantify the results, which are presented in Table 7.5. In general, it can be seen that compared to the 2D results the orders of the errors are comparable but slightly larger and that the CCC scores are relatively low. All models perform better at t_1 compared to t_2 for all patients. However, while before it was concluded that the chemotherapy models always

outperformed the models without chemotherapy at t_1, this is no longer the case: the MSE of all patients is larger and the GRE of patient p_3 is also larger for the DIRD model than for the RD model at t_1. This is rather unexpected, as in this case it would be more logical for the calibration to return a very small value for α, or even $\alpha = 0$, thus reducing the DIRD model to the RD model which has better results at t_1, but this did not happen. For the validation time point t_2, it can be seen that RD has a lower MSE and GRE for p_1 and p_3. For p_2, however, the MSE and GRE values of DIRD are better than the values of the RD model. Lastly, the CCC values are better for RD compared to DIRD for all patients. The bad performance of both models for p_3 is also reflected in the high error values, especially in the GRE at t_2. One possible explanation for this is that at t_2 there was only one slice with tumour cells in it while at t_1 all slices still contained quite a lot of tumour cells. Thus, although the initial decrease was rather small, this patient in the end responded well to treatment, which the models did not predict.

		$MSE(t_1)$	$MSE(t_2)$	$GRE(t_1)$	$GRE(t_2)$	$CCC(t_1)$	$CCC(t_2)$
p_1	RD	$5.487 \cdot 10^6$	$3.949 \cdot 10^9$	$2.322 \cdot 10^{-2}$	0.717	0.999	0.381
	DIRD	$6.635 \cdot 10^6$	$3.501 \cdot 10^9$	$3.204 \cdot 10^{-2}$	0.386	0.999	0.372
p_2	RD	$6.031 \cdot 10^7$	$9.388 \cdot 10^9$	$5.618 \cdot 10^{-2}$	0.346	0.998	0.554
	DIRD	$1.205 \cdot 10^8$	$9.145 \cdot 10^9$	$5.234 \cdot 10^{-2}$	0.203	0.998	0.308
p_3	RD	$1.409 \cdot 10^8$	$6.295 \cdot 10^{10}$	$1.135 \cdot 10^{-2}$	1.649	0.999	0.304
	DIRD	$5.122 \cdot 10^7$	$9.323 \cdot 10^{10}$	$3.692 \cdot 10^{-3}$	2.497	0.999	0.248

Table 7.5: Mean squared errors, global relative errors and concordance correlation coefficient for t_1 and t_2 of the RD and DIRD models in 3D for all patients.

8

Discussion and recommendations

In this chapter, the results presented in previous chapters are discussed and recommendations are made for future research. First, some remarks are made on the pre-processing steps and suggestions are made to improve the calibration and other aspects of the implementation in Section 8.1. Next, the methods that were used to calculate the chemotherapy term are discussed in Section 8.2 and lastly the 2D and 3D results are discussed in Section 8.3.

8.1. Model implementation

In this thesis, the pre-processed data from Oudhof was used [11]. However, as noted in that thesis, there is still room for improvement in how the data was pre-processed. For example, to reduce noise in the MRI images, it is possible to use a Gaussian filter [14]. In addition, after the tumour has been segmented by the radiologist, one could use a fuzzy c-means algorithm to refine the boundaries as was done in certain papers [8, 9]. Furthermore, for the data of this thesis the segmentation was done before registration, but it might be better to do this after registration as this is also the order that was followed in other research [3, 5, 6, 8]. On the other hand, the current order allows the future use of a tumour volume preserving registration algorithm to make sure the tumour volume does not change during registration [3, 6, 42]. Another relevant remark to make here is that the tumour densities are estimated using the ADC values found in the DW scans. In addition to cellularity, many factors like cell size and cell membrane permeability play a role in changes in these ADC values, so the estimated tumour densities are only an approximation of the actual tumour densities. Although many studies use the ADC values to calculate tumour densities, they all comment on the ambiguity of its interpretation and recommend finding a better way to estimate the tumour densities more precisely [6–9, 14]. Moreover, it should be noted that for the tissue segmentation a voxel was assumed to be either fibroglandular, adipose or tumorous. This is of course a simplification of reality, just like the assumption that a tumorous voxel consists of only tumour cells.

Although α, D_0 and $k(\overline{x})$ were all considered as patient-specific parameters and calibrated as such, the other parameters (γ, E, λ and ν) were given literature values while these most likely also differ per patient. In the future, it should therefore be considered to determine these parameters per patient as well by for example using modality independent elastography to estimate the breast elasticity parameters based on MRI scans [3]. In addition, it should be noted that the carrying capacity θ is assumed to be constant in time and space, and it might be interesting to investigate options to make this a spatiotemporal parameter, although this would complicate the model as it requires some modelling equations for θ. In a paper by Hormuth et al. [14], the MCRD model was for example implemented with $\theta(\overline{x})$ instead of θ.

The calibration in this thesis was done with the Trust Region Reflective algorithm, which is different from the Levenberg-Marquardt algorithm that was usually applied in the literature [3, 5, 6, 8, 9, 11, 14, 17]. The advantage of TRF is that it is relatively faster and bounds can be imposed on the parameters. This was in general not done as these bounds slowed down the algorithm, but if calibration without

bounds yielded a negative value for α or D_0, then calibration was run again with lower bounds for these parameters. It is however questionable whether this approach is correct, as it is rather strange that these parameters can become negative and it thus begs the question of what goes wrong. Perhaps the model is not able to capture the behaviour of the measured tumour densities for those cases, as many modelling assumptions are made and not all aspects of tumour growth are included. In the future, it would be good to investigate other non-linear least squares algorithms to see if a different algorithm gives better and faster results. The time factor is especially important here because the calibration in which the algorithm is used is the bottleneck in the implementation. Having a faster non-linear least squares algorithm could thus significantly speed up the implementation. One of the papers on the MCRD model in 3D for example describes how the parameters can be estimated through an inverse problem that is based on the adjoint state method, which is supposed to be numerically efficient [6].
The time integration is currently done with the explicit Forward Euler method, which is conditionally stable and thus restricts the time step. One of the possible improvements to look into is using an implicit or a semi-implicit method instead, as this would allow a bigger time step and thus reduces the computations. Calculating one iteration however usually takes longer for implicit methods compared to explicit methods as it involves solving a system of linear equations. It is therefore not immediately clear whether this change will improve the computation time of calibration, in which the calculation from t_0 to t_1 has to be performed many times with different parameter values.
Another aspect of the implementation that should be made quicker is solving the linear-elastic equation for the mechanically coupled models. This was now done with a direct solver, but in the future a Krylov subspace method like the Conjugate Gradient method could be used. By using a preconditioner like an incomplete Cholesky decomposition, additional speedup can be achieved. This will help in reducing the calibration time as well, which is especially important for the three-dimensional implementation, where the mechanical models were not used due to this time complexity issue.

To overcome the issue of the under-determined problem, a reduced mask was introduced. The proliferation rate was calibrated for each voxel within this mask, and for the other voxels in the ROI the average of their neighbours was taken. This decision was made based on the observation that in previous work the proliferation rate seemed to have a smooth distribution [11]. However, due to the averaging, some voxels will have gotten a higher or lower value than they would have gotten in standard calibration without the reduced mask, which means that the calibrated proliferation rate is perhaps less optimal. Additionally, the number of parameters was reduced quite a lot while it only had to be reduced by two to make sure the number of unknowns equalled the number of data points, so perhaps this approach was too rigorous. On the other hand, this reduction of parameters has made the calibration a lot faster. Since most papers did not comment on how they dealt with the under-determined problem, there might be other approaches that work better. One possible solution would be to include an extra MRI scan in the calibration phase, which would create more data points, but making an extra MRI scan is currently not part of the protocol and comes with additional costs.

In future research, it would be interesting to investigate the timing of the second MRI scan that is used in calibration as well. In some papers, the second MRI was already made after one round of treatment [3, 5, 6, 8], while in others it was made after several rounds of treatments [9], just like in this thesis. It is possible that this timing plays a big role in how accurate the model prediction at t_2 is and would therefore be relevant to research. In addition, from a practical perspective, knowing how well the tumour responds to treatment after one treatment round is better than knowing this halfway through treatment.

An important realisation for this study is that the MRI data was viewed as ground truth and that the assumption was made that the measured tumour cells from the MRI corresponded exactly with the tumour cells present in the tissue. Although it was found that for HER2+ patients radiologic complete response often predicts pathologic complete response [16], it will not always be the case, which is exactly the reason why in surgery tissue is extracted and sent to the laboratory to inspect the tissue for remaining tumour cells. This is thus a limiting assumption in this work and something to keep in mind for practical implementation because even if the model can perfectly predict the tumour density found in the MRI at the end of treatment, it might not correspond with the actual tumour density in the tissue.

8.2. Chemotherapy

In this work, both the Kety-Tofts model and Normalised Blood Volume Map were used to calculate the chemotherapy term, which were compared in Section 6.3. As stated in that section, KT has been extensively described in various literature and is based on a physical process. Only the standard KT model was used, so v_p was set to zero for simplicity, which was also done in one of the papers on the DIMCRD model [8]. Many steps had to be taken to obtain the fitted parameters that were needed to calculate the chemotherapy curves. Both the fitted parameters and the resulting drug distributions did not give results that seemed realistic. One explanation that was given for this was that this method may not be suitable for the data due to the temporal resolution, which was also the reason why NBVM was used in the paper by Jarrett et al. [9]. This method has only been described in the two papers that used the DIMCRD model and there is thus less scientific support for this method compared to KT. In addition, this method assumed that the highest concentration of chemotherapy would be in the tumour, but it is not certain that this reflects reality as chemotherapy in general kills all dividing cells. On the other hand, this method was rather easy to implement and calculating the chemotherapy curves was quick, although it was quite a struggle to find a suitable value for β. The choice for this parameter influenced the results a lot and in some cases, it was observed that the number of tumour cells showed unrealistic oscillations with no global decrease. Therefore, one of the recommendations is to include β in the calibration in the same way that the papers on DIMCRD did [8, 9].

In the analysis of the DIRD and DIMCRD model, it was sometimes observed that there were heavy oscillations in the total number of tumour cells. From a certain point onward, the model in that case predicted that the tumour cells grew back as quickly as they were eradicated. It seemed like the model reached some sort of equilibrium state around which the number of tumour cells fluctuated between two asymptotes. This would make it impossible for the curve to go to zero at any point and thus there is no way that all tumour cells will be eradicated. Although this was not investigated further, it is relevant to look into the cause of this unrealistic behaviour, because in general tumour cells will not grow back that quickly and the number of tumour cells will go down over time during treatment.

Another important remark to make here is that the chemotherapy curves were all based on the DCE scan at t_0. However, a tumour changes the vasculature and changes shape as treatment progresses. As NBVM assumes that the concentration of the drug is highest within the tumour, this means that at t_0 and t_1 the same area contains a high concentration while in reality, the tumour at t_1 has shrunk and thus the area with a high concentration should be a lot smaller. It is therefore important to use the DCE scan of t_0 for the chemotherapy curves between t_0 and t_1 and use the DCE scan of t_1 to derive the chemotherapy curves between t_1 and t_2 in future research as this might improve the results, which is also the approach that was followed in the papers that used NBVM [8, 9]. For p_2, the DCE scan of t_1 has been used as the DCE scan of t_0 was not suitable: since this scan was made at a different hospital, the dimensions differed a lot compared to the other scans and there was no information on the MRI protocol. Therefore, it was not clear how much time there was between the scans and how many pre- and post-contrast scans were made, which is information that is needed to calculate the chemotherapy curves. Thus, to still include this patient, the only possibility was to use the scan of t_1 as this one was made at EMC, although this could have influenced the results for this patient and could have caused for example different calibrated proliferation rates compared to when the DCE scan of t_0 was used.

Furthermore, it is important to note that in calculating the chemotherapy term only the days on which chemotherapy was given have been taken into account. This means that the dosage and other components of treatment were not included as data. In the future, it will be interesting to also incorporate these to model the treatment more accurately. As the immunotherapy components trastuzumab and pertuzumab spread in a different way than chemotherapy, an option to model this would be to use PET scans as data and derive the drug concentration curves as was done in a recent paper by Jarret et al. [9]. In that paper, this extended chemotherapy model was investigated for two patients and it was found that the model that uses both MRI and PET was better at distinguishing pCR from non-pCR outcomes.

The DIRD equation would then look as follows for treatment consisting of two components:

$$\frac{\partial N(\overline{x},t)}{\partial t} = \nabla \cdot (D\nabla N(\overline{x},t)) + k(\overline{x})N(\overline{x},t)\Big(1 - \frac{N(\overline{x},t)}{\theta}\Big) - C^{drug}(\overline{x},t),$$

where

$$C^{drug}(\overline{x},t) = \alpha_1 C^{drug_1}(\overline{x},t^*)e^{-\beta_1 t} + \alpha_2 C^{drug_2}(\overline{x},t^*)e^{-\beta_2 t}.$$

This however introduces extra global parameters, which could complicate the calibration and requires the availability of both MRI and PET scans for patients. Furthermore, both the original model and this extended model only take into account the efficacy and decay rate of a drug and assume that all cancer cells respond in the same matter, but when multiple components are considered, it is important to also model the different mechanisms of each drug and their drug synergy.

8.3. Results

In the analysis of the 2D models, it was observed that the total number of tumour cells of the DIRD and DIMCRD models was higher than that of the RD and MCRD models, which means that the chemotherapy models predicted a more limited decay in the number of tumour cells. This was a positive result for p_2, as RD and MCRD in that case underestimated the total number of tumour cells, but a negative result for p_1 and p_3. For p_3 the curves of the chemotherapy models even increased towards the end. These curves were used to evaluate the behaviour of the models over time, which especially for the chemotherapy models was interesting as this sometimes displayed unexpected oscillations, which have already been discussed in the previous section. It should be noted, however, that for these curves the sum is taken over all voxels, which means that local underestimates and local overestimates in voxels could compensate for each other. For that reason, the results were also quantified by looking at the MSE, GRE and CCC values for both t_1 and t_2. For calibration, it was concluded that the DIRD and DIMCRD models had better MSE, GRE and CCC values than RD and MCRD. However, when the models were used to predict forward for validation, it was not possible to draw such a conclusion because this varied per patient and per measure. Therefore, it is not clear whether including the mechanics and/or the chemotherapy in the prediction gives better quantitative results in 2D. The CCC values of DIMCRD at t_2 were not better than the values of MCRD for all patients, as opposed to what was found in the literature [7].

For the 3D results, only the RD and DIRD models were evaluated, so the mechanics were not included. It turned out that the DIRD model did not outperform RD at t_1 in the way that was seen for the 2D results. However, the MSE and GRE values of DIRD were better at t_2 for two out of three patients. On the other hand, all CCC values of RD were better than the values of DIRD. Thus, for the 3D case, it is not completely clear whether RD is better than DIRD or not as it differed per patient and measure. One of the limitations of the 3D simulations is that only three slices were considered when in most cases the tumour was also present in other slices. It is however not completely clear if in future research all slices in the breast need to be included or if a smaller number can be chosen as long as the tumour is completely included in them. Another big limitation of the 3D implementation was that only the RD and DIRD models were used and that thus mechanics were not taken into account, while the mechanics could play an important role in 3D. It would thus be interesting to compare the results in 3D with and without mechanics to further investigate the relevance of including the mechanics. In the future, it is therefore recommended to speed up the implementation with the previously mentioned options to allow the MCRD and DIMCRD models to be used in 3D.

It is important to reflect on whether the three-dimensional extension has improved the model as well, where it should also be noted that the computation time was a lot longer and it was not possible to run all models. In 3D, the MSE and GRE values were in general higher and the CCC values were lower compared to 2D, so the results seemed less good. It is however not fair to compare these 2D and 3D results in this way, as for the 2D implementation only a thin slice was considered and for 3D the domain consisted of three thick slices, which means that the physical domain was a lot bigger and each voxel contained a lot more tumour cells. In Section 7.4 an attempt was made to compare the 2D and 3D implementations for the same breast region and there it was found that the 3D model seemed slightly better, although this comparison was only made for one patient. Even though in one of the papers on

the DIMCRD model it was found that the 3D MCRD and DIMCRD implementations gave more accurate tumour density predictions than in 2D, it turned out that those differences were not significant [7]. Thus, to be able to evaluate whether extending the model into 3D improves the model, firstly the implementation should be made quicker so the MCRD and DIMCRD models can also be used and secondly more patients should be included so a better comparison can be made between the 2D and 3D models.

Especially this last point should be emphasised because the limited group of patients was one of the reasons why it was difficult to draw conclusions on which model performed best in the analysis of the quantitative results of the models. The fact that only three patients were included is therefore a big limitation of this research and it is thus strongly recommended to involve more patients in later research. This will help in concluding which model gives the best results and in understanding which parts of the models will need to be improved upon. In the selection of patients, it would also be a good addition to include patients that achieved pCR after their chemotherapy and immunotherapy treatment. Currently, all patients included in this thesis did not achieve pCR, meaning there were still tumour cells remaining at the end of treatment. It is crucial to also include HER2+ pCR patients in future efforts because the models should be able to capture that outcome of treatment as well.

In the comparison of the models, the performance has been analysed in multiple ways to determine which model was best and to see if the extensions have improved the accuracy of the predictions. In general, models are simplifications of reality in which many modelling assumptions are made, as is also the case for the models considered in this thesis. By adding more aspects to a model, a model usually gets more realistic but this does not always mean that the results become better. In addition, often a more complex model has a higher computation time. This is also what was seen in this thesis and in other research on reaction-diffusion based cancer models. The RD model is the most basic variant and by including mechanics more physical aspects are taken into account, but the computation time increased a lot and the results did not necessarily get better, although this appeared to also depend on the slice thickness that was used. In the RD and MCRD models, the proliferation rate was constant in time, which was one of the modelling assumptions, while the decay of tumour cells due to treatment is not constant in time. This was the motivation for including the chemotherapy term in the DIRD and DIMCRD models. This however introduced extra parameters that had to be estimated or calibrated. Due to this addition, the model has become more non-linear and seemed more sensitive to small changes in the parameter values. Furthermore, there was a higher chance of overfitting, as was often seen with unrealistic oscillating curves. In the presented results, the chemotherapy models turned out to not necessarily be better in terms of MSE, GRE and CCC than the models without chemotherapy; the results were usually comparable and the errors were of the same order. This study focused on including the treatment data and investigating which model gave the closest results to reality. It is however also important to reflect on whether including a treatment term helps to predict how many treatment rounds are required. Between t_0 and t_1, the treatment is set and because the proliferation rate is constant over time in the RD and MCRD models, it is rather hard to make such a prediction. The only possibility would be to assume all treatment rounds have the same components, dosage and frequency, and just predict the model forward in time from t_1 onward, see when the total number of tumour cells hits zero and derive the number of rounds from this. The DIRD and DIMCRD models offer more possibilities for this, as the chemotherapy curves can be adjusted based on which days the treatment is given and, when the models have been further developed, the components and their dosage could be taken into account as well. In that way, in silico experiments can be done to test if increasing for example the dosage or frequency gives better results, in a similar way to what was done in the paper by Jarrett et al. [8]. There is thus more flexibility in the chemotherapy models than there is in the models without chemotherapy to predict how many rounds of treatment are necessary. However, the predictions of the models are at this point not accurate enough and should therefore first be improved before they can be used for this.

9 Conclusion

The aim of this thesis was to answer the following research question:

How can the MCRD model be improved to achieve better results in modelling chemotherapy and the growth of tumours to determine the correct number of treatment rounds in HER2+ breast cancer patients?

In this chapter, a summary is made of the research that was done and the results that were presented, and the research question is answered.

To improve the implementation, firstly some steps were taken to solve the issue of the under-determined problem. While in previous research a Tikhonov parameter was used [11], in this work a reduced mask within the ROI has been introduced. Instead of calibrating $k(\overline{x})$ for each voxel within the ROI, this is now only determined for the set of voxels within the reduced mask, which additionally also reduces computation time. The proliferation rate of the other voxels in the ROI is calculated by taking the average of their neighbouring voxels. In addition, a different non-linear least squares algorithm was used, which was faster and allowed for bounds on the parameters that had to be optimised.

In the standard MCRD model, the proliferation rate represented both cell growth and cell death. This term was however not time dependent while in reality cell death varies over time due to treatment. Therefore, as an extension to this model, a chemotherapy term was added to simulate cell death through treatment. To calculate this term, the standard Kety-Tofts model and the Normalised Blood Volume Map were used, of which the latter turned out to be the best option for the DCE data that was used for this research.

In the model analysis, the influence of the fitted parameters was investigated, where the option to have a constant proliferation rate instead of a proliferation rate per voxel was also explored. It was found that in that case the model no longer properly models the decay of tumour cells on a local level, so it is logical to determine this per voxel to maintain the heterogeneity within the tumour. In addition, a test was made to see if calibrating with all three MRI scans indeed improved the prediction, which turned out to be the case. As a final part of the model analysis, the influence of the slice thickness was explored. It turned out that for the standard slice thickness there was already a difference between the chemotherapy model with and without mechanics, which was not the case for the models without chemotherapy.

To investigate whether this addition of the chemotherapy term improved the model, a comparison was made between the results of the four different types of reaction-diffusion models (RD, MCRD, DIRD and DIMCRD) in 2D. The mean squared error, global relative error and concordance correlation coefficient were used to quantify the results. It was concluded that in calibration the chemotherapy models all outperformed the models without chemotherapy, but at the validation time point for which the models made a prediction, it was not possible to conclude this. Although higher CCC values were found compared to literature, the CCC values of the chemotherapy models were not always higher

than the ones of the models without chemotherapy. It is thus not possible to conclude that adding chemotherapy has improved the prediction in terms of MSE, GRE or CCC values. On the other hand, including this treatment term is an essential step to take to be able to use a model to predict how many rounds of therapy are needed to eradicate all tumour cells.

As a final step, the model was extended to 3D. The influence of the slice thickness was again analysed and for this case it was concluded that having a thick slice was the best option. Several options were considered to decrease the number of computations, of which the results for downsampling the (x, y) plane were presented. This however did not turn out to be a good option for this, as the local errors increased a lot in comparison to the normal grid and the effect of chemotherapy was not visible in the same way as before. In comparing the 2D results and 3D results for the same breast region, it was found that the 3D model had slightly better results on a local and global level, although the computation time was a lot longer. The 3D model predictions were evaluated for all patients but again it was not possible to draw a conclusion on which model performed best for all patients and all measures. However, when looking at the CCC values, the RD model gave more accurate results than DIRD. Compared to 2D the results seemed less good and the computation time for 3D was a lot higher. On the other hand, to accurately model all the dynamics within the breast, the 3D model is probably more realistic than for example using the 2D model with a thick slice, because it is expected that the interaction between the slices plays an important role and thus including this will likely result in more accurate results.

Various limitations were discussed and recommendations were given to improve the model. One of the limitations is the small cohort of patients that were considered for this study. In the future, the sample size should be increased and the group of patients should also include patients with pCR. Another limitation of this study was that in the 3D implementation only three slices were used and only the models without mechanics were considered due to the computation time of the mechanically coupled models. The calibration should thus be made quicker by for example choosing a different non-linear least squares algorithm and using an iterative method to solve the linear-elastic equation. Furthermore, to properly incorporate the treatment schedule of the patients, it is advised to use the second MRI scan for determining the chemotherapy curves between the calibration and validation point and to include an immunotherapy term in addition to the chemotherapy term.

The goal of this thesis was to extend the MCRD model by including the treatment schedule of patients and by extending the model from 2D to 3D. Although the drug-incorporated model does not always give better results compared to the model without chemotherapy, it is more suitable to predict the required number of treatment rounds because it offers more flexibility to simulate different treatment frequencies, components and dosages. It is not clear if the 3D model improves the predictions, so the implementation first needs to be further developed before conclusions can be drawn on this.

A

Appendix

A.1. Acquisition parameters for the first MRI scan of p_2

	DW-MRI	DCE-MRI
Scan sequence	*unknown*	*unknown*
Repetition time (ms)	9337	4.33
Echo time (ms)	108	1.29
Flip angle (degrees)	90	*unknown*
Voxel dimension (mm)	1.89 × 1.89	0.80 × 0.80
Acqusition matrix	190 ×116	448 × 448

Table A.1: MRI acquisition parameters for the first scan at t_0 of p_2

A.2. Pre-processing information

A.2.1. Registration

Before extracting values from the MRI scans, it is important to align the images. The reason behind this is that in different scans the breast may not be in the same position so we need to perform a correction for motion. We want to compare precise changes in the tissue and thus need to compare the pixel values of the same location in the breast. If this step is skipped, the model might report that for example the tumour moved to the left between the first and second scan when in fact the breast was located slightly to the left in the second scan and the tumour did not move at all. This process of aligning different scans is called *registration*. Before registration, the MRI scans are upscaled to make sure that the number of slices in the z-direction is the same for each scan. After upscaling, the voxel spacing has of course been changed, which is taken into account during the registration step. In addition, measures were taken to make sure that both DCE and DW covered the same part of the breast by for example excluding certain slices if needed. As a next step, the registration is performed with functions from the Python library `itk-elastics` which is an open source toolbox for rigid and nonrigid registration of images. Two different types of registration are used: rigid and non-rigid registration. In *rigid registration*, the internal architecture of an image is preserved and the images are only transformed with a rotation or translation. In *nonrigid registration*, also called elastic registration, an image is stretched to match the other image. This method thus accounts for local deformations [2]. During the first registration step, inter-scan registration with a non-rigid algorithm is applied to the DCE images of different time points, meaning the DCE scans of time t_0 and t_2 are both aligned to the DCE scan at time t_1. Next, intra-scan registration is performed by a rigid registration algorithm to align the DW and DCE images of the same time points, so the DW scan at time t_0 is aligned with the DCE scan at time t_0, and DW at t_1 is aligned with DCE at t_1, and DW at t_2 is aligned with DCE at t_2. Lastly, the DW scan at t_0 and DW at t_2 images are aligned with DCE at t_1 with nonrigid registration. After this final step, all images are aligned properly so the data can be analysed properly. More details about these steps can be found in [11].

A.2.2. Tissue segmentation

To use the model and be able to display results in a proper way, certain segmentations of the tissue need to be created. Firstly, it will be useful to distinguish between interior and exterior points as the three-dimensional matrices with all voxel intensities contain a lot of points that are located outside the breast. For this, region-growing is used to create a mask that can be used in displaying the results of the model. Note that because of registration this mask is the same for the MRI scans that were made at different time points.

Secondly, the tumour needs to be located on the scans of all three time points. There are different approaches to this. One approach that is described in some literature consists of computing the average of the pre-contrast images, and the average of the post-contrast images and a voxel is marked as a tumorous voxel if the increase between these averages is more than a certain threshold, which is usually taken to be 80% [3–6, 31]. Next, the biggest group of voxels within the region of interest that is marked as a tumour is taken as the tumour for the analysis. This method thus uses the fact that tumours light up because of the contrast agent. Another approach that is found in the literature is to manually draw a region of interest around the tumour and apply a fuzzy c-means algorithm to refine the boundaries of the tumour [8, 9]. This algorithm is a clustering algorithm where points can belong to multiple clusters with a certain likelihood. For this thesis, however, the tumour has been manually segmented by dr A.I.M Obedijn who is a breast cancer radiologist at Erasmus MC. This is similar to the second approach without using fuzzy c-means and is also done in other image-driven breast cancer research [19, 20, 33]. Figure A.1 shows the resulting tumour for p_1 at the start of treatment when a threshold of 80% is used and when the segmentation is performed by a radiologist respectively. Note that these images have been downsampled to reduce the number of computations needed by the model later on.

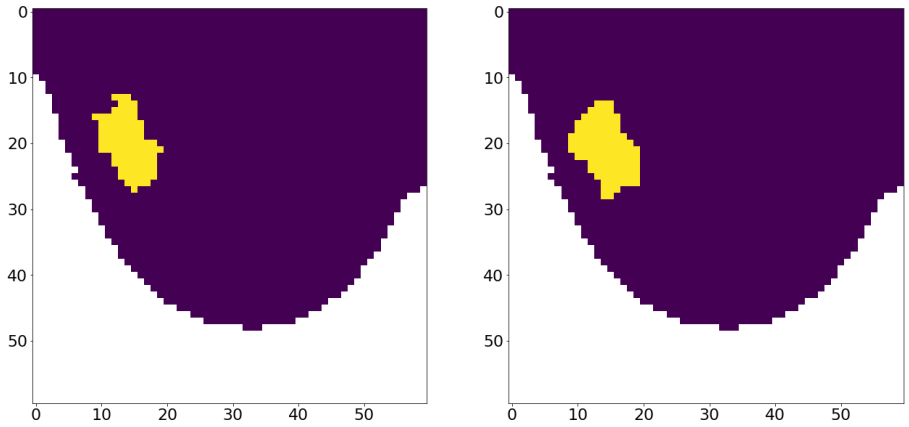

(a) Tumour segmentation with 80% threshold.

(b) Tumour segmentation by radiologist.

Figure A.1: Result of tumour segmentation for p_1 with different methods.

Lastly, to include the mechanical properties of different tissue types, a segmentation between fibroglandular and adipose tissue is needed. In the work of Oudhof [11], three different methods are investigated: using a simple threshold, applying contrast limited adaptive histogram equalization (which is also used by Jarrett et al. [8]) and applying global histogram equalization. It turned out that global histogram equalization provided the best results and thus this method was used to compute the segmentations for the data. Figure A.2 shows the segmentation results for p_1 at t_0.

A.2.3. Tumour density

To obtain the number of tumour cells per voxel within the tumour, the DW images at the three different time points are used. For this, firstly the *apparent diffusion coefficients* (ADC) are calculated for each voxel on the registered scans. As explained before, these ADC values are a measure of the rate of water diffusion within the tissue. These values are calculated per voxel using the formula below.

$$ADC = \frac{1}{3} \sum_{i=x,y,z} \frac{\ln(\frac{S_0}{S_i})}{b_i},$$

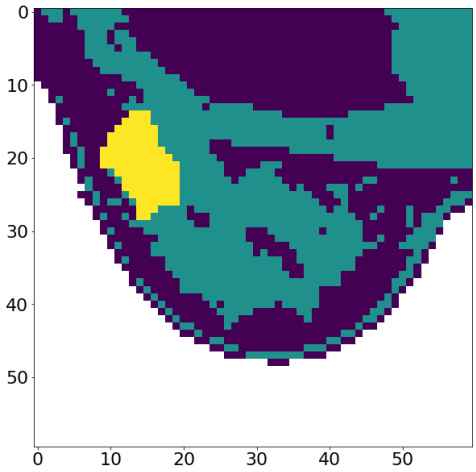

Figure A.2: Segmentation of tissue. Tumour, adipose and fibroglandular tissue are shown in yellow, purple and green, respectively.

Here, i is the direction of diffusion-weighting, b_i is the amount of diffusion-weighting applied to the sample and S_i and S_0 are the signal intensities in each voxel with and without diffusion gradients respectively. Using these ADC values, an estimate of the number of tumour cells is made, which is represented by $N(\overline{x}, t)$. It has been shown by many researchers that there is an inverse relationship between ADC values and cellularity [17], thus indicating that tissue with a low ADC value contains many cells.

$$N(\overline{x}, t) = \theta\Big(\frac{ADC_w - ADC(\overline{x}, t)}{ADC_w - ADC_{min}}\Big)$$

In the above formula, θ represents the same carrying capacity as in Equations 3.1 and 3.5, ADC_w is the ADC value of free water, ADC_{min} is the smallest ADC values measured in the tumour, corresponding to the voxel with the largest number of cells, and $ADC(\overline{x}, t)$ is the ADC value of the voxel $\overline{x}$ on time t.

A.3. Stability criterion

As stated before, for Explicit Euler there is a bound on Δt to ensure stability of the method. In this section we work out the stability condition, for which we follow the same approach as the one used by Oudhof [11]. For this analysis we need to write the system as a linear system of the form $N^{m+1} = N^m + \Delta t A N^m$, which is why firstly the proliferation is linearized around the numerical solution $\tilde{N}$. In [11] it was shown that this leads to $f(N) \approx k\frac{\tilde{N}^m}{\theta} + kN(1-2\frac{\tilde{N}}{\theta})$ and that the constant can be ignored in the stability analysis. This leads to the following equation.

$$\begin{aligned} N_{i,j}^{m+1} = N_{i,j}^m + \Delta t\Bigg(& \frac{1}{2\Delta x^2}\Big(\big(D_{i,j} + D_{i-1,j}\big)N_{i-1,j}^m - \big(D_{i-1,j} + 2D_{i,j} + D_{i+1,j}\big)N_{i,j}^m + \big(D_{i,j} + D_{i+1,j}\big)N_{i+1,j}^m\Big) \\ & + \frac{1}{2\Delta y^2}\Big(\big(D_{i,j} + D_{i,j-1}\big)N_{i,j-1}^m - \big(D_{i,j-1} + 2D_{i,j} + D_{i,j+1}\big)N_{i,j}^m + \big(D_{i,j} + D_{i,j+1}\big)N_{i,j+1}^m\Big) \\ & + k_{i,j}N_{i,j}^m\Big(1 - 2\frac{\tilde{N}_{i,j}}{\theta}\Big) - \alpha C_{i,j}^m N_{i,j}^m\Bigg) \end{aligned}$$

This leads to a system $N^{m+1} = N^m + \Delta t A N^m$, where $A = \frac{1}{2\Delta x^2}\mathcal{X} + \frac{1}{2\Delta y^2}\mathcal{Y} + \mathcal{R}$, for which $\mathcal{X}, \mathcal{Y}$ and $\mathcal{R}$ are defined below.

$$\mathcal{X} = \begin{pmatrix} X_1 & \tilde{X}_1 & & & \\ \tilde{X}_1 & X_2 & \tilde{X}_2 & & \\ & \ddots & \ddots & \ddots & \\ & & \tilde{X}_{n_x-2} & X_{n_x-1} & \tilde{X}_{n_x-1} \\ & & & \tilde{X}_{n_x-1} & X_{n_x} \end{pmatrix}$$

$$X_i = \begin{pmatrix} -\left(D_{i-1,1} + 2D_{i,1} + D_{i+1,1}\right) & & \\ & \ddots & \\ & & -\left(D_{i-1,n_y} + 2D_{i,n_y} + D_{i+1,n_y}\right) \end{pmatrix}$$

$$\tilde{X}_i = \begin{pmatrix} D_{i-1,1} + D_{i,1} & & \\ & \ddots & \\ & & D_{i-1,n_y} + D_{i,n_y} \end{pmatrix}$$

$$\mathcal{Y} = \begin{pmatrix} Y_1 & & & & \\ & Y_2 & & & \\ & & \ddots & & \\ & & & Y_{n_x-1} & \\ & & & & Y_{n_x} \end{pmatrix}$$

$$Y_i = \begin{pmatrix} -\left(D_{i,0} + 2D_{i,1} + D_{i,2}\right) & \left(D_{i,1} + D_{i,2}\right) & & & \\ \left(D_{i,1} + D_{i,2}\right) & -\left(D_{i,1} + 2D_{i,2} + D_{i,3}\right) & \left(D_{i,2} + D_{i,3}\right) & & \\ & \ddots & \ddots & \ddots & \\ & \left(D_{i,n_y-1} + D_{i,n_y-2}\right) & -\left(D_{i,n_y-2} + 2D_{i,n_y-1} + D_{i,n_y}\right) & \left(D_{i,n_y-1} + D_{i,n_y}\right) & \\ & & \left(D_{i,n_y} + D_{i,n_y-1}\right) & -\left(D_{i,n_y-1} + 2D_{i,n_y} + D_{i,n_y+1}\right) \end{pmatrix}$$

$$\mathcal{R} = \begin{pmatrix} R_1 & & & & \\ & R_2 & & & \\ & & \ddots & & \\ & & & R_{n_x-1} & \\ & & & & R_{n_x} \end{pmatrix}$$

$$R_i = \begin{pmatrix} k_{i,1}\left(1 - 2\frac{\tilde{N}_{i,1}}{\theta}\right) - \alpha C_{i,1}^m & & & \\ & k_{i,2}\left(1 - 2\frac{\tilde{N}_{i,2}}{\theta}\right) - \alpha C_{i,2}^m & & \\ & & \ddots & \\ & & & k_{i,n_y}\left(1 - 2\frac{\tilde{N}_{i,n_y}}{\theta}\right) - \alpha C_{i,n_y}^m \end{pmatrix}$$

In the expressions above, n_x and n_y refer to the number of points in x-direction and y-direction respectively. Note that the matrix A is symmetric, so $A^T = A$. This means that all eigenvalues are real, which is an important observation because this means that for Forward Euler the stability condition is given by $\Delta t \leq \frac{2}{-\lambda}$ for all eigenvalues λ of the matrix A. To determine these eigenvalues, let us apply the Gershgorin Circle Theorem [25].

Theorem A.3.1. *The eigenvalues λ of a general $n \times n$ matrix A are located in the complex plane in the union of circles $|\lambda - a_{i,i}| \leq \sum_{j=1 i \neq j}^{m} |a_{i,j}|$.*

Writing out this expression for any i, j yields:

$$\left|\lambda - \left(-\frac{1}{2\Delta x^2}\left(D_{i-1,j} + 2D_{i,j} + D_{i+1,j}\right) - \frac{1}{2\Delta y^2}\left(D_{i,j-1} + 2D_{i,j} + D_{i,j+1}\right) + \left(k_{i,j}\left(1 - 2\frac{\tilde{N}_{i,j}}{\theta}\right) - \alpha C_{i,j}\right)\right|$$
$$\leq \frac{1}{2\Delta x^2}\left(D_{i-1,j} + 2D_{i,j} + D_{i+1,j}\right) + \frac{1}{2\Delta y^2}\left(D_{i,j-1} + 2D_{i,j} + D_{i,j+1}\right)$$

To simplify the expression, we introduce the following notation:

$$D_x = D_{i-1,j} + 2D_{i,j} + D_{i+1,j}$$
$$D_y = D_{i,j-1} + 2D_{i,j} + D_{i,j+1}$$
$$R = k_{i,j}\left(1 - 2\frac{\tilde{N}_{i,j}}{\theta}\right) - \alpha C_{i,j}$$

This leads to the following bound on the eigenvalues of A:

$$\left|\lambda + \frac{1}{2\Delta x^2}D_x + \frac{1}{2\Delta y^2}D_y - R\right| \leq \frac{1}{2\Delta x^2}D_x + \frac{1}{2\Delta y^2}D_y$$
$$\begin{cases}\lambda \leq R \\ \lambda \geq -\frac{1}{\Delta x^2}D_x - \frac{1}{\Delta y^2}D_y + R\end{cases}$$

Now note that we already know that $\lambda \leq 0$ since we do not have an exponentially growing solution. Therefore, only the second inequality plays a role. Let us first rewrite the R-term before we use the expression for the stability criterion in $\Delta t \leq \frac{2}{-\lambda}$.

Claim A.3.1. $R \geq -|k|_{\max} - \alpha C_{\max}$

Proof. By definition of θ, we know that $0 \leq \hat{N}_{i,j} \leq \theta$, so $0 \leq \frac{\hat{N}_{i,j}}{\theta} \leq 1$ and thus $-1 \leq 1 - 2\frac{\hat{N}_{i,j}}{\theta} \leq 1$. From this it can be concluded that $-|k|_{\max} \leq k_{i,j}\left(1 - 2\frac{\hat{N}_{i,j}}{\theta}\right) \leq |k|_{\max}$. Since no negative concentrations can appear, we can conclude that $0 \leq C_{i,j} \leq C_{\max}$. In addition we know $\alpha > 0$, from which we know that $-\alpha C_{\max} \leq -\alpha C_{i,j} \leq 0$. Combining the above, we know that
$-|k|_{\max} - \alpha C_{\max} \leq k_{i,j}\left(1 - 2\frac{\tilde{N}_{i,j}}{\theta}\right) - \alpha C_{i,j} = R.$ □

Writing $D_{\max}$ for the maximum diffusion in the breast, we can easily conclude that

$$D_x = D_{i-1,j} + 2D_{i,j} + D_{i+1,j} \leq 4D_{\max}$$
$$D_y = D_{i,j-1} + 2D_{i,j} + D_{i,j+1} \leq 4D_{\max}$$

Let us now use the information from above to rewrite the expression.

$$\lambda \geq -\frac{1}{\Delta x^2}D_x - \frac{1}{\Delta y^2}D_y + R \geq -4D_{\max}\left(\frac{1}{\Delta x^2} + \frac{1}{\Delta y^2}\right) - |k|_{\max} - \alpha C_{\max}$$

This expression can now be filled into the stability criterion to find the final bound on Δt.

$$\Delta t \leq \frac{2}{4D_{\max}\left(\frac{1}{\Delta x^2} + \frac{1}{\Delta y^2}\right) + |k|_{\max} + \alpha C_{\max}} \leq \frac{2}{-\lambda}$$

Thus, if the bound given in Equation A.3.1 is met, then we know that $\Delta t \leq \frac{2}{-\lambda}$ and thus in that case Forward Euler is stable.

$$\Delta t \leq \frac{2}{4D_{\max}\left(\frac{1}{\Delta x^2} + \frac{1}{\Delta y^2}\right) + |k|_{\max} + \alpha C_{\max}} \tag{A.3.1}$$

A.4. Proof for Section 6.1.2

In this section we will provide the proof that by using the Cosine Bolus Parker function as $C^{CA}_{plasma}(t)$ in Equation A.4.1 yields Equation A.4.2.

$$C^{CA}_{tissue}(t) = K^{trans}\int_0^t C^{CA}_{plasma}(s) \cdot e^{-k_{ep}(t-s)}ds \tag{A.4.1}$$

$$C_{tissue}^{CA}(t) = \begin{cases} \frac{a_B a_G K^{trans}}{k_{ep}-\mu_G}\Big(f(t,\mu_G) + \big(\frac{k_{ep}-\mu_G}{a_G} - 1\big)f(t,k_{ep})\Big) & \text{for } 0 \le t \le t_B \\ \frac{a_B a_G K^{trans}}{k_{ep}-\mu_G}\Big(f(t_B,\mu_G)e^{-\mu_G(t-t_B)} + \big(\frac{k_{ep}-\mu_G}{a_G} - 1\big)f(t,k_{ep})e^{-k_{ep}(t-t_B)}\Big) & \text{for } t > t_B \end{cases} \tag{A.4.2}$$

As a reminder, the Cosine Bolus Parker function is given by

$$C_{plasma}^{CA}(t) = \begin{cases} a_B(1-\cos(\mu_B t)) + a_B a_G f(t,\mu_G) & \text{for } 0 \le t \le t_B \\ a_B a_G f(t_B,\mu_G)e^{-\mu_G(t-t_B)} & \text{for } t > t_B, \end{cases} \tag{A.4.3}$$

where

$$f(t,a) = \frac{1}{a}(1-e^{-at}) - \frac{1}{a^2+\mu_B^2}\Big(a\cos(\mu_B t) + \mu_B \sin(\mu_B t) - ae^{-at}\Big).$$

Our proof will be separated into two different parts. Firstly we will prove the case for $0 \le t \le t_B$ and secondly we will prove the case $t > t_B$.

Claim A.4.1. *For* $0 \le t \le t_B$, $C_{tissue}^{CA}(t) = \frac{a_B a_G K^{trans}}{k_{ep}-\mu_G}\Big(f(t,\mu_G) + \big(\frac{k_{ep}-\mu_G}{a_G} - 1\big)f(t,k_{ep})\Big)$

Proof. By the Kety-Tofts model, we know that

$$C_{tissue}^{CA}(t) = K^{trans}\int_0^t C_{plasma}^{CA}(s)\cdot e^{-k_{ep}(t-s)}ds.$$

Note that to prove this first case, this integral should be equal to

$$\frac{a_B a_G}{k_{ep}-\mu_G}\Big(f(t,\mu_G) + \big(\frac{k_{ep}-\mu_G}{a_G} - 1\big)f(t,k_{ep})\Big).$$

Now let us fill in the definition for $C_{plasma}^{CA}(s)$ from the Cosine Bolus Parker function for $0 \le t \le t_B$ and write out the terms within the integral.

$$\int_0^t C_{plasma}^{CA}(s)\cdot e^{-k_{ep}(t-s)}ds = \int_0^t \Big(a_B(1-\cos(\mu_B s)) + a_B a_G f(s,\mu_G)\Big)\cdot e^{-k_{ep}(t-s)}ds$$

$$= \int_0^t \Bigg(a_B(1-\cos(\mu_B s)) + a_B a_G\Big(\frac{1}{\mu_G}(1-e^{-\mu_G s}) - \frac{1}{\mu_G^2+\mu_B^2}\Big(\mu_G\cos(\mu_B s) + \mu_B\sin(\mu_B s) - \mu_G e^{-\mu_G s}\Big)\Big)\Bigg)\cdot e^{-k_{ep}(t-s)}ds$$

$$= a_B\int_0^t (1-\cos(\mu_B s))e^{-k_{ep}(t-s)}ds + \frac{a_B a_G}{\mu_G}\int_0^t (1-e^{-\mu_G s})e^{-k_{ep}(t-s)}ds - \frac{a_B a_G \mu_G}{\mu_G^2+\mu_B^2}\int_0^t \cos(\mu_B s)e^{-k_{ep}(t-s)}ds$$

$$- \frac{a_B a_G \mu_B}{\mu_G^2+\mu_B^2}\int_0^t \sin(\mu_B s)e^{-k_{ep}(t-s)}ds + \frac{a_B a_G \mu_G}{\mu_G^2+\mu_B^2}\int_0^t e^{-\mu_G s}e^{-k_{ep}(t-s)}ds$$

We will now write out each integral separately. For this, we apply partial integration twice for the $\cos(\mu_B s)$ and $\sin(\mu_B s)$ terms.

$$\int_0^t \cos(\mu_B s)e^{k_{ep}s}ds = \Big[\frac{1}{\mu_B}\sin(\mu_B s)e^{k_{ep}s}\Big]_{s=0}^{s=t} - \frac{k_{ep}}{\mu_B}\int_0^t \sin(\mu_B s)e^{k_{ep}s}ds$$

$$= \frac{1}{\mu_B}\sin(\mu_B t)e^{k_{ep}t} - \frac{k_{ep}}{\mu_B}\Big(\Big[-\frac{1}{\mu_B}\cos(\mu_B s)e^{k_{ep}s}\Big]_{s=0}^{s=t} + \frac{k_{ep}}{\mu_B}\int_0^t \cos(\mu_B s)e^{k_{ep}s}ds\Big)$$

$$\Big(1+\frac{k_{ep}^2}{\mu_B^2}\Big)\int_0^t \cos(\mu_B s)e^{k_{ep}s}ds = \frac{1}{\mu_B^2}\Big(e^{k_{ep}t}\big(\mu_B\sin(\mu_B t) + k_{ep}\cos(\mu_B t)\big) - k_{ep}\Big)$$

$$\int_0^t \cos(\mu_B s)e^{k_{ep}s}ds = \frac{1}{k_{ep}^2+\mu_B^2}\Big(e^{k_{ep}t}\big(k_{ep}\cos(\mu_B t) + \mu_B\sin(\mu_B t)\big) - k_{ep}\Big)$$

$$\int_0^t \sin(\mu_B s)e^{k_{ep}s}ds = \Big[-\frac{1}{\mu_B}\cos(\mu_B s)e^{k_{ep}s}\Big]_{s=0}^{s=t} + \frac{k_{ep}}{\mu_B}\int_0^t \cos(\mu_B s)e^{k_{ep}s}ds$$

$$= -\frac{1}{\mu_B}\cos(\mu_B t)e^{k_{ep}t} + \frac{1}{\mu_B} + \frac{k_{ep}}{\mu_B}\Big(\Big[\frac{1}{\mu_B}\sin(\mu_B s)e^{k_{ep}s}\Big]_{s=0}^{s=t} - \frac{k_{ep}}{\mu_B}\int_0^t \sin(\mu_B s)e^{k_{ep}s}ds\Big)$$

$$(1+\frac{k_{ep}^2}{\mu_B^2})\int_0^t \sin(\mu_B s)e^{k_{ep}s}ds = \frac{1}{\mu_B^2}\Big(e^{k_{ep}t}\big(k_{ep}\sin(\mu_B t) - \mu_B\cos(\mu_B t)\big) + \mu_B\Big)$$

$$\int_0^t \sin(\mu_B s)e^{k_{ep}s}ds = \frac{1}{k_{ep}^2+\mu_B^2}\Big(e^{k_{ep}t}\big(-\mu_B\cos(\mu_B t) + k_{ep}\sin(\mu_B t)\big) + \mu_B\Big)$$

The next step is to calculate all the integrals and write them into convenient forms.

$$\int_0^t (1-\cos(\mu_B s))e^{-k_{ep}(t-s)}ds = \int_0^t e^{-k_{ep}(t-s)}ds - e^{-k_{ep}t}\int_0^t \cos(\mu_B s)e^{k_{ep}s}ds$$

$$= \frac{1}{k_{ep}}\big[e^{-k_{ep}(t-s)}\big]_{s=0}^{s=t} - \frac{e^{-k_{ep}t}}{k_{ep}^2+\mu_B^2}\Big(e^{k_{ep}t}\big(k_{ep}\cos(\mu_B t) + \mu_B\sin(\mu_B t)\big) - k_{ep}\Big)$$

$$= \frac{1}{k_{ep}}\big(1-e^{-k_{ep}t}\big) - \frac{1}{k_{ep}^2+\mu_B^2}\big(k_{ep}\cos(\mu_B t) + \mu_B\sin(\mu_B t) - k_{ep}e^{-k_{ep}t}\big) = f(t,k_{ep})$$

$$\int_0^t (1-e^{-\mu_G s})e^{-k_{ep}(t-s)}ds = e^{-k_{ep}t}\int_0^t e^{k_{ep}s} - e^{s(k_{ep}-\mu_G)}ds = e^{-k_{ep}t}\Big[\frac{1}{k_{ep}}e^{k_{ep}s} - \frac{1}{k_{ep}-\mu_G}e^{s(k_{ep}-\mu_G)}\Big]_{s=0}^{s=t}$$

$$= e^{-k_{ep}t}\Big(\frac{1}{k_{ep}}\big(e^{k_{ep}t}-1\big) - \frac{1}{k_{ep}-\mu_G}\big(e^{t(k_{ep}-\mu_G)}-1\big)\Big)$$

$$= \frac{1}{k_{ep}}\big(1-e^{-k_{ep}t}\big) - \frac{1}{k_{ep}-\mu_G}\big(e^{-\mu_G t}-e^{-k_{ep}t}\big)$$

$$= \frac{1}{k_{ep}(k_{ep}-\mu_G)}\big(k_{ep}-\mu_G - k_{ep}e^{-k_{ep}t} + \mu_G e^{-k_{ep}t} - k_{ep}e^{-\mu_G t} + k_{ep}e^{-k_{ep}t}\big)$$

$$= \frac{1}{k_{ep}(k_{ep}-\mu_G)}\Big(k_{ep}\big(1-e^{-\mu_G t}\big) - \mu_G\big(1-e^{-k_{ep}t}\big)\Big)$$

$$= \frac{1}{k_{ep}-\mu_G}\Big(\big(1-e^{-\mu_G t}\big) - \frac{\mu_G}{k_{ep}}\big(1-e^{-k_{ep}t}\big)\Big)$$

$$\int_0^t \cos(\mu_B s)e^{-k_{ep}(t-s)}ds = e^{-k_{ep}t}\int_0^t \cos(\mu_B s)e^{k_{ep}s}ds$$

$$= \frac{e^{-k_{ep}t}}{k_{ep}^2+\mu_B^2}\Big(e^{k_{ep}t}\big(k_{ep}\cos(\mu_B t) + \mu_B\sin(\mu_B t)\big) - k_{ep}\Big)$$

$$= \frac{1}{k_{ep}^2+\mu_B^2}\big(k_{ep}\cos(\mu_B t) + \mu_B\sin(\mu_B t) - k_{ep}e^{-k_{ep}t}\big)$$

$$\int_0^t \sin(\mu_B s)e^{-k_{ep}(t-s)}ds = e^{-k_{ep}t}\int_0^t \sin(\mu_B s)e^{k_{ep}s}ds$$

$$= \frac{e^{-k_{ep}t}}{k_{ep}^2+\mu_B^2}\Big(e^{k_{ep}t}\big(-\mu_B\cos(\mu_B t) + k_{ep}\sin(\mu_B t)\big) + \mu_B\Big)$$

$$= \frac{1}{k_{ep}^2+\mu_B^2}\big(-\mu_B\cos(\mu_B t) + k_{ep}\sin(\mu_B t) + \mu_B e^{-k_{ep}t}\big)$$

$$\int_0^t e^{-\mu_G s} e^{-k_{ep}(t-s)} ds = e^{-k_{ep}t} \int_0^t e^{s(k_{ep}-\mu_G)} ds = \frac{1}{k_{ep}-\mu_G} e^{-k_{ep}t} \left[e^{s(k_{ep}-\mu_G)} \right]_{s=0}^{s=t}$$
$$= \frac{1}{k_{ep}-\mu_G} e^{-k_{ep}t} \left(e^{t(k_{ep}-\mu_G)} - 1 \right) = \frac{1}{k_{ep}-\mu_G} \left(e^{-\mu_G t} - e^{-k_{ep}t} \right)$$

We can now combine the above information into the long expression that was found before.

$$\int_0^t C_{plasma}^{CA}(s) \cdot e^{-k_{ep}(t-s)} ds = a_B \int_0^t (1 - \cos(\mu_B s)) e^{-k_{ep}(t-s)} ds + \frac{a_B a_G}{\mu_G} \int_0^t (1 - e^{-\mu_G s}) e^{-k_{ep}(t-s)} ds$$
$$- \frac{a_B a_G \mu_G}{\mu_G^2 + \mu_B^2} \int_0^t \cos(\mu_B s) e^{-k_{ep}(t-s)} ds - \frac{a_B a_G \mu_B}{\mu_G^2 + \mu_B^2} \int_0^t \sin(\mu_B s) e^{-k_{ep}(t-s)} ds + \frac{a_B a_G \mu_G}{\mu_G^2 + \mu_B^2} \int_0^t e^{-\mu_G s} e^{-k_{ep}(t-s)} ds$$
$$= a_B f(t, k_{ep}) + \frac{a_B a_G}{\mu_G} \frac{1}{k_{ep}-\mu_G} \left(\left(1 - e^{-\mu_G t}\right) - \frac{\mu_G}{k_{ep}} \left(1 - e^{-k_{ep}t}\right) \right)$$
$$- \frac{a_B a_G \mu_G}{\mu_G^2 + \mu_B^2} \frac{1}{k_{ep}^2 + \mu_B^2} \left(k_{ep} \cos(\mu_B t) + \mu_B \sin(\mu_B t) - k_{ep} e^{-k_{ep}t} \right)$$
$$- \frac{a_B a_G \mu_B}{\mu_G^2 + \mu_B^2} \frac{1}{k_{ep}^2 + \mu_B^2} \left(- \mu_B \cos(\mu_B t) + k_{ep} \sin(\mu_B t) + \mu_B e^{-k_{ep}t} \right)$$
$$+ \frac{a_B a_G \mu_G}{\mu_G^2 + \mu_B^2} \frac{1}{k_{ep}-\mu_G} \left(e^{-\mu_G t} - e^{-k_{ep}t} \right)$$
$$= a_B \left(f(t, k_{ep}) + \frac{a_G}{k_{ep}-\mu_G} \left(\frac{1}{\mu_G} \left(1 - e^{-\mu_G t}\right) - \frac{1}{k_{ep}} \left(1 - e^{-k_{ep}t}\right) \right) \right.$$
$$- \frac{a_G \mu_G}{(\mu_G^2 + \mu_B^2)(k_{ep}^2 + \mu_B^2)} \left(k_{ep} \cos(\mu_B t) + \mu_B \sin(\mu_B t) - k_{ep} e^{-k_{ep}t} \right)$$
$$- \frac{a_G \mu_B}{(\mu_G^2 + \mu_B^2)(k_{ep}^2 + \mu_B^2)} \left(- \mu_B \cos(\mu_B t) + k_{ep} \sin(\mu_B t) + \mu_B e^{-k_{ep}t} \right)$$
$$\left. + \frac{a_G \mu_G}{(\mu_G^2 + \mu_B^2)(k_{ep}-\mu_G)} \left(e^{-\mu_G t} - e^{-k_{ep}t} \right) \right)$$

We will leave the first line as it is for now and focus on the lower three lines of the expression. Let us now take the $\cos(\mu_B t)$ term together and rewrite them.

$$a_G \cos(\mu_B t) \left(\frac{\mu_G k_{ep} - \mu_B^2}{(\mu_G^2 + \mu_B^2)(k_{ep}^2 + \mu_B^2)} \right) = a_G \cos(\mu_B t) \left(\frac{(\mu_G k_{ep} - \mu_B^2)(k_{ep} - \mu_G)}{(\mu_G^2 + \mu_B^2)(k_{ep}^2 + \mu_B^2)(k_{ep} - \mu_G)} \right)$$
$$= \frac{a_G \cos(\mu_B t)}{(k_{ep} - \mu_G)} \left(\frac{\mu_G k_{ep}^2 - \mu_G^2 k_{ep} - \mu_B^2 k_{ep} + \mu_B^2 \mu_G}{(\mu_G^2 + \mu_B^2)(k_{ep}^2 + \mu_B^2)} \right)$$
$$= \frac{a_G \cos(\mu_B t)}{(k_{ep} - \mu_G)} \left(\frac{\mu_G (k_{ep}^2 + \mu_B^2) - k_{ep}(\mu_G^2 + \mu_B^2)}{(\mu_G^2 + \mu_B^2)(k_{ep}^2 + \mu_B^2)} \right)$$
$$= \frac{a_G}{(k_{ep} - \mu_G)} \left(\frac{1}{\mu_G^2 + \mu_B^2} \mu_G \cos(\mu_B t) - \frac{1}{k_{ep}^2 + \mu_B^2} k_{ep} \cos(\mu_B t) \right)$$

Next, we do the same for the $\sin(\mu_B t)$ term.

$$\begin{aligned}
a_G \sin(\mu_B t)\Big(\frac{\mu_G\mu_B + k_{ep}\mu_B}{(\mu_G^2+\mu_B^2)(k_{ep}^2+\mu_B^2)}\Big) &= a_G \sin(\mu_B t)\Big(\frac{(\mu_G\mu_B + k_{ep}\mu_B)(k_{ep}-\mu_G)}{(\mu_G^2+\mu_B^2)(k_{ep}^2+\mu_B^2)(k_{ep}-\mu_G)}\Big) \\
&= \frac{a_G \sin(\mu_B t)}{(k_{ep}-\mu_G)}\Big(\frac{\mu_G\mu_B k_{ep} - \mu_G^2\mu_B + \mu_B k_{ep}^2 - \mu_G\mu_B k_{ep} + \mu_B^3 - \mu_B^3}{(\mu_G^2+\mu_B^2)(k_{ep}^2+\mu_B^2)}\Big) \\
&= \frac{a_G \sin(\mu_B t)}{(k_{ep}-\mu_G)}\Big(\frac{\mu_B(k_{ep}^2+\mu_B^2) - \mu_B(\mu_G^2+\mu_B^2)}{(\mu_G^2+\mu_B^2)(k_{ep}^2+\mu_B^2)}\Big) \\
&= \frac{a_G}{(k_{ep}-\mu_G)}\Big(\frac{1}{\mu_G^2+\mu_B^2}\mu_B \sin(\mu_B t) - \frac{1}{k_{ep}^2+\mu_B^2}\mu_B \sin(\mu_B t)\Big)
\end{aligned}$$

Finally, let us look at the $e^{-k_{ep}t}$ terms.

$$\begin{aligned}
a_G e^{-k_{ep}t}\Big(\frac{\mu_G k_{ep} - \mu_B^2}{(\mu_G^2+\mu_B^2)(k_{ep}^2+\mu_B^2)} - \frac{\mu_G}{(\mu_G^2+\mu_B^2)(k_{ep}-\mu_G)}\Big) &= a_G e^{-k_{ep}t}\Big(\frac{(\mu_G k_{ep} - \mu_B^2)(k_{ep}-\mu_G) - \mu_G(k_{ep}^2+\mu_B^2)}{(\mu_G^2+\mu_B^2)(k_{ep}^2+\mu_B^2)(k_{ep}-\mu_G)}\Big) \\
&= \frac{a_G e^{-k_{ep}t}}{(k_{ep}-\mu_G)(k_{ep}^2+\mu_B^2)}\Big(\frac{\mu_G k_{ep}^2 - \mu_G^2 k_{ep} - \mu_B^2 k_{ep} + \mu_G\mu_B^2 - \mu_G k_{ep}^2 - \mu_G\mu_B^2}{(\mu_G^2+\mu_B^2)}\Big) \\
&= \frac{a_G e^{-k_{ep}t}}{(k_{ep}-\mu_G)(k_{ep}^2+\mu_B^2)}\Big(-\frac{k_{ep}(\mu_G^2+\mu_B^2)}{(\mu_G^2+\mu_B^2)}\Big) = \frac{a_G}{(k_{ep}-\mu_G)}\Big(\frac{-1}{k_{ep}^2+\mu_B^2}k_{ep}e^{-k_{ep}t}\Big)
\end{aligned}$$

Now let us fill in these new expressions into the expression we found before.

$$\begin{aligned}
\int_0^t C_{plasma}^{CA}(s)\cdot e^{-k_{ep}(t-s)}ds &= a_B\Big(f(t,k_{ep}) + \frac{a_G}{k_{ep}-\mu_G}\Big(\frac{1}{\mu_G}\big(1-e^{-\mu_G t}\big) - \frac{1}{k_{ep}}\big(1-e^{-k_{ep}t}\big)\Big) \\
&+ \frac{a_G}{(k_{ep}-\mu_G)}\Big(\frac{1}{\mu_G^2+\mu_B^2}\mu_G\cos(\mu_B t) - \frac{1}{k_{ep}^2+\mu_B^2}k_{ep}\cos(\mu_B t)\Big) \\
&+ \frac{a_G}{(k_{ep}-\mu_G)}\Big(\frac{1}{\mu_G^2+\mu_B^2}\mu_B\sin(\mu_B t) - \frac{1}{k_{ep}^2+\mu_B^2}\mu_B\sin(\mu_B t)\Big) \\
&+ \frac{a_G}{(k_{ep}-\mu_G)}\Big(\frac{-1}{k_{ep}^2+\mu_B^2}k_{ep}e^{-k_{ep}t}\Big) + \frac{a_G}{(k_{ep}-\mu_G)}\Big(\frac{1}{\mu_G^2+\mu_B^2}\mu_G e^{-\mu_G t}\Big)\Big) \\
&= a_B\Big(f(t,k_{ep}) + \frac{a_G}{k_{ep}-\mu_G}\Big(\frac{1}{\mu_G}\big(1-e^{-\mu_G t}\big) - \frac{1}{\mu_G^2+\mu_B^2}\Big(\mu_G\cos(\mu_B t) + \mu_B\sin(\mu_B t) - \frac{1}{\mu_G}e^{-\mu_G t}\Big)\Big) \\
&- \frac{a_G}{k_{ep}-\mu_G}\Big(\frac{1}{k_{ep}}\big(1-e^{-k_{ep}t}\big) - \frac{1}{k_{ep}^2+\mu_B^2}\Big(k_{ep}\cos(\mu_B t) + \mu_B\sin(\mu_B t) - \frac{1}{k_{ep}}e^{-k_{ep}t}\Big)\Big)\Big) \\
&= a_B\Big(f(t,k_{ep}) + \frac{a_G}{k_{ep}-\mu_G}\big(f(t,\mu_G) - f(t,k_{ep})\big)\Big) = \frac{a_B a_G}{k_{ep}-\mu_G}\Big(f(t,\mu_G) + \Big(\frac{k_{ep}-\mu_G}{a_G} - 1\Big)f(t,k_{ep})\Big)
\end{aligned}$$

We have thus proven the case $0 \le t \le t_B$.

□

We now move on to the case $t > t_B$.

Claim A.4.2. *For* $t > t_B$, $C_{tissue}^{CA}(t) = K^{trans}\Big(\int_0^{t_B} C_{plasma}^{CA}(s)\cdot e^{-k_{ep}(t_B-s)}ds + \int_{t_B}^t C_{plasma}^{CA}(s)\cdot e^{-k_{ep}(t-s)}ds\Big)$

Proof. By the Kety-Tofts model, we again know that:

$$\begin{aligned}
C_{tissue}^{CA}(t) &= K^{trans}\int_0^t C_{plasma}^{CA}(s)\cdot e^{-k_{ep}(t-s)}ds \\
&= K^{trans}\Big(\int_0^{t_B} C_{plasma}^{CA}(s)\cdot e^{-k_{ep}(t_B-s)}ds + \int_{t_B}^t C_{plasma}^{CA}(s)\cdot e^{-k_{ep}(t-s)}ds\Big)
\end{aligned}$$

Thus, to prove the claim, we need to show that the sum of the integrals is equal to

$$\frac{a_B a_G}{k_{ep}-\mu_G}\Big(f(t_B,\mu_G)e^{-\mu_G(t-t_B)}+\Big(\frac{k_{ep}-\mu_G}{a_G}-1\Big)f(t,k_{ep})e^{-k_{ep}(t-t_B)}\Big).$$

It was just shown that:

$$\int_0^t C^{CA}_{plasma}(s)\cdot e^{-k_{ep}(t-s)}ds=\frac{a_B a_G}{k_{ep}-\mu_G}\Big(f(t,\mu_G)+\Big(\frac{k_{ep}-\mu_G}{a_G}-1\Big)f(t,k_{ep})\Big)$$

When we now divide by $e^{-k_{ep}t}$ and multiply with $e^{-k_{ep}t_b}$, we obtain:

$$\int_0^{t_B} C^{CA}_{plasma}(s)\cdot e^{-k_{ep}(t_B-s)}ds=\frac{a_B a_G}{k_{ep}-\mu_G}\Big(f(t_B,\mu_G)e^{-k_{ep}(t-t_B)}+\Big(\frac{k_{ep}-\mu_G}{a_G}-1\Big)f(t_B,k_{ep})e^{-k_{ep}(t-t_B)}\Big)$$

We calculate the final term that is still left.

$$\begin{aligned}\int_{t_B}^t C^{CA}_{plasma}(s)\cdot e^{-k_{ep}(t-s)}ds &= a_B a_G f(t_B,\mu_G)e^{\mu_G t_B-k_{ep}t}\int_{t_B}^t e^{s(k_{ep}-\mu_G)}ds\\ &=\frac{a_B a_G}{k_{ep}-\mu_G}f(t_B,\mu_G)e^{\mu_G t_B-k_{ep}t}\Big(e^{t(k_{ep}-\mu_G)}-e^{t_B(k_{ep}-\mu_G)}\Big)\\ &=\frac{a_B a_G}{k_{ep}-\mu_G}\Big(f(t_B,\mu_G)e^{-\mu_G(t-t_B)}-f(t_B,\mu_G)e^{-k_{ep}(t-t_B)}\Big)\end{aligned}$$

Let us now add up the integrals.

$$\begin{aligned}&\int_0^{t_B} C^{CA}_{plasma}(s)\cdot e^{-k_{ep}(t_B-s)}ds+\int_{t_B}^t C^{CA}_{plasma}(s)\cdot e^{-k_{ep}(t-s)}ds\\ &=\frac{a_B a_G}{k_{ep}-\mu_G}\Big(f(t,\mu_G)e^{-k_{ep}(t-t_B)}+\Big(\frac{k_{ep}-\mu_G}{a_G}-1\Big)f(t,k_{ep})e^{-k_{ep}(t-t_B)}\Big)\\ &+\frac{a_B a_G}{k_{ep}-\mu_G}\Big(f(t_B,\mu_G)e^{-\mu_G(t-t_B)}-f(t_B,\mu_G)e^{-k_{ep}(t-t_B)}\Big)\\ &=\frac{a_B a_G}{k_{ep}-\mu_G}\Big(f(t_B,\mu_G)e^{-\mu_G(t-t_B)}+\Big(\frac{k_{ep}-\mu_G}{a_G}-1\Big)f(t,k_{ep})e^{-k_{ep}(t-t_B)}\Big)\end{aligned}$$

This proves the case for $t > t_B$. □

A.5. Poster for Workshop

From the 6th until the 8th of July 2022, the workshop *Nonlinear Diffusion Equations with Applications in Biology* took place in Nijmegen. This workshop, organised by the Radbound University, was aimed to combine the theory of nonlinear diffusion equations and their modelling applications in biology. During the workshop, the poster shown on the next page was presented during the poster session. It was awarded with the Best Poster Award.

Modelling Breast Cancer: Mechanically Coupled Reaction-Diffusion model to predict tumour response in HER2+ patients

E. Slingerland[@*] N.L. Oudhof[*] A. Jager[†] L. Rens[*] M.B. van Gijzen[*]

[@]e.slingerland@student.tudelft.nl, [*]Delft Institute of Applied Mathematics, TU Delft, [†]Department of Oncology, Erasmus Medical Center

Introduction

Goal: *Predict the needed number of chemotherapy rounds for breast cancer patients.*
Method: *Model the amount of tumour cells in each position in the breast with a reaction-diffusion equation.*
Model input: *DCE and DW MRI scans before and during treatment.*
Model output: *Predicted tumour density at the conclusion of treatment.*

Model

The **Mechanically Coupled Reaction-Diffusion** (MCRD) model, described in various literature [1–3], combines available qualitative data from the Dynamic Contrast Enhanced (DCE) and Diffusion Weighted (DW) MRI scans with a **spatiotemporal reaction-diffusion model** that takes the **mechanical properties** of the tissue into account to predict the tumour density in each position of the breast for one patient. Recently, the model has been extended to also include a **chemotherapy term** that is based on the patients' treatment schedule [4–6]. Equations 1, 2 and 3 describe the MCRD model, for which the descriptions of the variables and parameters are given in Table 1 and 2 respectively.

$$\frac{\partial N(\overline{x},t)}{\partial t} = \nabla \cdot (D\nabla N(\overline{x},t)) + k(\overline{x})N(\overline{x},t)(1-\frac{N(\overline{x},t)}{\theta}) - \alpha C^{drug}_{tissue}(\overline{x},t)N(\overline{x},t) \quad (1)$$

$$D = D_0 e^{-\gamma \sigma_{vm}(\overline{x},t)} \quad (2)$$

$$\nabla \cdot G\nabla \vec{u} + \nabla \frac{G}{1-2\nu}(\nabla \cdot \vec{u}) + \lambda \nabla N(\overline{x},t) = 0 \quad (3)$$

Variable	Description
$N(\overline{x},t)$	Number of tumour cells in the voxel at position $\overline{x}$ at time t
$D(\overline{x},t)$	Diffusion coefficient of tumour cells (mm^2/day)
σ_{vm}	Von Mises stress (kPa)
G	Shear modulus due to breast tissue properties (kPa)
$\vec{u}$	Displacement vector due to tumour growth (mm)
$C^{drug}_{tissue}(\overline{x},t)$	Concentration of drugs in tissue in voxel at position $\overline{x}$ at time t (μM)

Table 1: Variables and their descriptions

Parameter	Description
$k(\overline{x})$	Proliferation rate of tumour cells per voxel (1/day)
θ	Capacity of tumour cells in one voxel
α	Efficacy of the drug against tumour cells ($1/\mu M \cdot$ day)
D_0	Diffusion coefficient in absence of stress (mm^2/day)
γ	Coupling constant for von Mises stress (1/kPa)
ν	Material property of Poisson ratio
λ	Coupling constant for displacement vector

Table 2: Parameters and their descriptions

To apply this model, a grid is determined based on the MRI scans, thus discretising the breast into voxels. Note that θ, which represents the maximum number of tumour cells that can fit into a voxel, is calculated based on the data. Furthermore, γ and λ are assigned literature values and $k(\overline{x})$, D_0 and α are calibrated in the simulation. For the spatial discretization the **Finite Difference Method** is used and for the temporal discretization **Forward Euler** is applied. Figure 1 shows the steps that are taken in calculating the MCRD model forward in time.

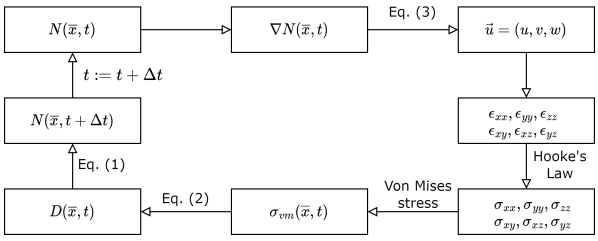

Figure 1: Steps to iterate forward

Modelling pipeline

In the implementation, several steps have to be taken to get a model prediction, including some **pre-processing** steps of the data. The dataset for the research consists of DCE and DW MRI scans before (t_0), during (t_1) and after treatment (t_2) for a group of HER2+ breast cancer patients that were selected by the involved internist-oncologist. The **modelling pipeline** is described below and illustrated in Figure 2.

- **Registration**: Using both rigid and non-rigid registration, the images from different sessions are aligned to correct for body movements.
- **Tissue segmentation**: The tissue is segmented into tumorous, fibroglandular and adipose tissue.
- **Calculating tumour density**: The tumour segmentation and calculated apparent diffusion coefficients (ADC) values are combined to determine tumour cell density for the three time points t_0, t_1 and t_2.
- **Calculating chemotherapy concentrations**: The concentration of drug at each time t and in each voxel $\overline{x}$ can either be calculated by using the (Extended) **Kety-Tofts model** of by computing the initial drug distribution and multiplying this with a function describing the decay of the drug in the tissue.
- **Calibration**: Based on initial guesses, the **optimal value** for the **patient-specific parameters** $k(\overline{x})$, D_0 and α are determined by running the model forward in time from t_0 to t_1 and comparing the estimated tumour density $N(\overline{x},t_1)$ with the actual tumour density $\hat{N}(\overline{x},t_1)$.
- **Evaluation**: The model is run from t_1 to t_2, yielding $N(\overline{x},t_2)$ which is compared to $\hat{N}(\overline{x},t_2)$ to evaluate the results.

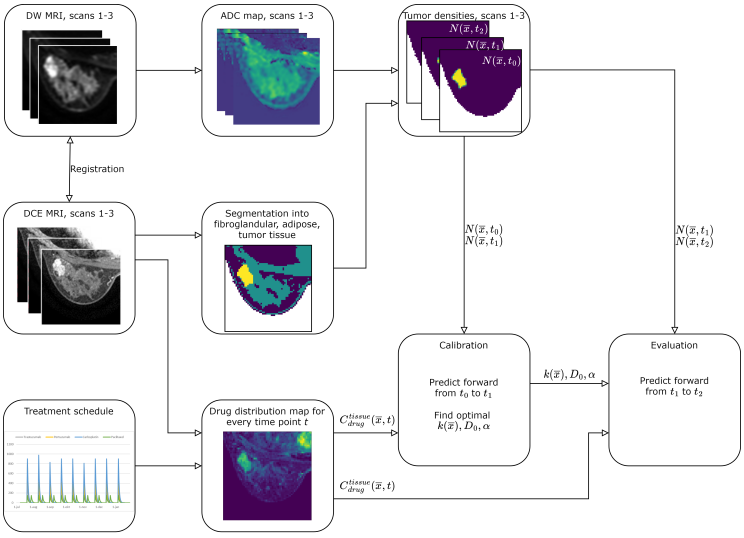

Figure 2: Modelling pipeline

Results

In the first part of this research, the chemotherapy term was left out (i.e. $\alpha = 0$) and a **comparison** was made between the **2D RD model**, which consists only of Equation 1, and the **2D MCRD model** [7]. The second part of the research consisted of incorporating the chemotherapy term by **including the treatment schedule** of the patient in the two-dimensional model, as this was expected to improve the predictions. Figure 3 displays the results of the 2D MCRD model for one of the patients. Presently, the option to **extend the model to 3D** is also being researched, where most likely computational complexities will have to be overcome.

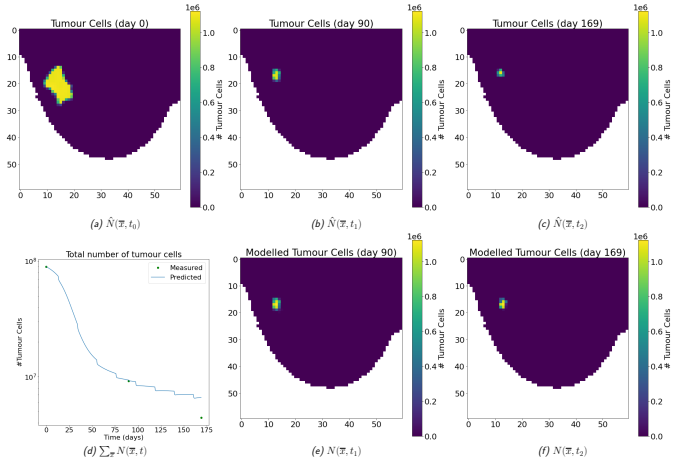

Figure 3: Results of the 2D MCRD model with chemotherapy for one patient. The top row shows the measured tumour densities with from left to right t_0, t_1, t_2, the bottom row shows the predicted tumour densities.

Conclusion

To **predict tumour response** in HER2+ patients, a 2D MCRD model has been implemented that uses MRI scans as input. Finite Difference was used for the spatial discretization, and Forward Euler was used for the forward calculations in time. In the implementation, the data had to be pre-processed by **registration** and **segmentation** to calculate the required quantities. After calibration, in which the **patient-specific** parameters were optimised by the model, the model is predicted forward in time to yield an **estimate of the tumour density at the conclusion of therapy**. Currently, our research focuses on improving and analysing the model that **includes the treatment schedule** and on **extending from 2D to 3D**.

References

[1] Jared A Weis et al. "A mechanically coupled reaction-diffusion model for predicting the response of breast tumors to neoadjuvant chemotherapy". In: *Physics in Medicine and Biology* 58.17 (2013), pp. 5851–5866. ISSN: 00319155. DOI: 10.1088/0031-9155/58/17/5851.

[2] Jared A Weis et al. "Predicting the response of breast cancer to neoadjuvant therapy using a mechanically coupled reaction-diffusion model". In: *Cancer Research* 75.22 (2015), pp. 4697–4707. ISSN: 15387445. DOI: 10.1158/0008-5472.CAN-14-2945.

[3] Jared A Weis, Michael I Miga, and Thomas E Yankeelov. "Three-dimensional image-based mechanical modeling for predicting the response of breast cancer to neoadjuvant therapy". In: *Computer Methods in Applied Mechanics and Engineering* 314 (2017), pp. 494–512. ISSN: 00457825. DOI: 10.1016/j.cma.2016.08.024. URL: http://dx.doi.org/10.1016/j.cma.2016.08.024.

[4] Angela M Jarrett et al. "Incorporating drug delivery into an imaging-driven, mechanics-coupled reaction diffusion model for predicting the response of breast cancer to neoadjuvant chemotherapy: Theory and preliminary clinical results". In: *Physics in Medicine and Biology* 63.10 (2018). ISSN: 13616560. DOI: 10.1088/1361-6560/aac040.

[5] Angela M Jarrett et al. "Evaluating patient-specific neoadjuvant regimens for breast cancer via a mathematical model constrained by quantitative magnetic resonance imaging data". In: *Neoplasia (United States)* 22.12 (2020), pp. 820–830. ISSN: 14765586. DOI: 10.1016/j.neo.2020.10.011.

[6] Angela M. Jarrett et al. "Towards integration of 64Cu-DOTA-trastuzumab PET-CT and MRI with mathematical modeling to predict response to neoadjuvant therapy in HER2 + breast cancer". In: *Scientific Reports* 10.1 (2020), pp. 1–14. ISSN: 20452322. DOI: 10.1038/s41598-020-77397-0. URL: https://doi.org/10.1038/s41598-020-77397-0.

[7] Nathalie Lisa Oudhof. "Predicting tumour response". Master thesis. Delft University of Technology, 2022. URL: http://resolver.tudelft.nl/uuid:bbdc3da4-6cba-41c5-a2f5-781468946265.

Erasmus MC Universitair Medisch Centrum Rotterdam

TU Delft Delft University of Technology

Department of Oncology

Delft Institute of Applied Mathematics

Bibliography

[1] Hyuna Sung et al. “Global Cancer Statistics 2020: GLOBOCAN Estimates of Incidence and Mortality Worldwide for 36 Cancers in 185 Countries”. In: *CA: A Cancer Journal for Clinicians* 71.3 (2021), pp. 209–249. ISSN: 0007-9235. DOI: 10.3322/caac.21660.

[2] Xia Li et al. “Analyzing spatial heterogeneity in DCE-and DW-MRI parametric maps to optimize prediction of pathologic response to neoadjuvant chemotherapy in breast cancer”. In: *Translational Oncology* 7.1 (2014), pp. 14–22. ISSN: 19365233. DOI: 10.1593/tlo.13748. URL: http://dx.doi.org/10.1593/tlo.13748.

[3] Jared A. Weis et al. “A mechanically coupled reaction-diffusion model for predicting the response of breast tumors to neoadjuvant chemotherapy”. In: *Physics in Medicine and Biology* 58.17 (2013), pp. 5851–5866. ISSN: 00319155. DOI: 10.1088/0031-9155/58/17/5851.

[4] Nkiruka C. Atuegwu et al. “Parameterizing the logistic model of tumor growth by DW-MRI and DCE-MRI data to predict treatment response and changes in breast cancer cellularity during neoadjuvant chemotherapy”. In: *Translational Oncology* 6.3 (2013), pp. 256–264. ISSN: 19365233. DOI: 10.1593/tlo.13130.

[5] Jared A. Weis et al. “Predicting the response of breast cancer to neoadjuvant therapy using a mechanically coupled reaction-diffusion model”. In: *Cancer Research* 75.22 (2015), pp. 4697–4707. ISSN: 15387445. DOI: 10.1158/0008-5472.CAN-14-2945.

[6] Jared A. Weis, Michael I. Miga, and Thomas E. Yankeelov. “Three-dimensional image-based mechanical modeling for predicting the response of breast cancer to neoadjuvant therapy”. In: *Computer Methods in Applied Mechanics and Engineering* 314 (2017), pp. 494–512. ISSN: 00457825. DOI: 10.1016/j.cma.2016.08.024. URL: http://dx.doi.org/10.1016/j.cma.2016.08.024.

[7] Angela M. Jarrett et al. “Incorporating drug delivery into an imaging-driven, mechanics-coupled reaction diffusion model for predicting the response of breast cancer to neoadjuvant chemotherapy: Theory and preliminary clinical results”. In: *Physics in Medicine and Biology* 63.10 (2018), pp. 1–29. ISSN: 13616560. DOI: 10.1088/1361-6560/aac040.

[8] Angela M. Jarrett et al. “Evaluating patient-specific neoadjuvant regimens for breast cancer via a mathematical model constrained by quantitative magnetic resonance imaging data”. In: *Neoplasia (United States)* 22.12 (2020), pp. 820–830. ISSN: 14765586. DOI: 10.1016/j.neo.2020.10.011.

[9] Angela M Jarrett et al. “Towards integration of 64Cu-DOTA-trastuzumab PET-CT and MRI with mathematical modeling to predict response to neoadjuvant therapy in HER2 + breast cancer”. In: *Scientific Reports* 10.1 (2020), pp. 1–14. ISSN: 20452322. DOI: 10.1038/s41598-020-77397-0. URL: https://doi.org/10.1038/s41598-020-77397-0.

[10] David G. Hicks and Swati Kulkarni. “HER2+ breast cancer: Review of Biologic Relevance and Optimal Use of Diagnostic Tools”. In: *American Journal of Clinical Pathology* 129.2 (2008), pp. 263–273. ISSN: 00029173. DOI: 10.1309/99AE032R9FM8WND1.

[11] Nathalie Lisa Oudhof. *Predicting tumour response (Master Thesis)*. Delft University of Technology, 2022. URL: http://resolver.tudelft.nl/uuid:bbdc3da4-6cba-41c5-a2f5-781468946265.

[12] Larry Norton. “Evolving Concepts in the Systemic Drug Therapy of Breast Cancer”. In: *Seminars in Oncology* 24.4 (1997), pp. 10–3.

[13] L Norton. “Kinetic Concepts in the Systemic Drug Therapy of Breast Cancer”. In: *Seminars in Oncology* 26.1 (1999), pp. 11–20.

[14] David A. Hormuth et al. “A mechanically coupled reaction-diffusion model that incorporates intratumoural heterogeneity to predict in vivo glioma growth”. In: *Journal of the Royal Society, Interface* 14.128 (2017). ISSN: 17425662. DOI: 10.1098/rsif.2016.1010.

[15] Larry Norton. “Conceptual Basis for Advances in the Systemic Drug Therapy of Breast Cancer”. In: *Seminars in Oncology* 24.4 (1997), pp. 11–2.

[16] Mette S. van Ramshorst et al. “MRI predicts pathologic complete response in HER2-positive breast cancer after neoadjuvant chemotherapy”. In: *Breast Cancer Research and Treatment* 164.1 (2017), pp. 99–106. ISSN: 15737217. DOI: 10.1007/s10549-017-4254-0.

[17] David A. Hormuth et al. “Mechanically coupled reaction-diffusion model to predict glioma growth: Methodological details”. In: *Methods in Molecular Biology* 1711.1 (2018), pp. 225–241. ISSN: 10643745. DOI: 10.1007/978-1-4939-7493-1{_}11.

[18] Thomas E. Yankeelov et al. “Integration of quantitative DCE-MRI and ADC mapping to monitor treatment response in human breast cancer”. In: *Magnetic Resonance Imaging* 25.1 (2007), pp. 1–13. ISSN: 15378276. DOI: 10.1016/j.mri.2006.09.006.Integration. URL: https://www.ncbi.nlm.nih.gov/pmc/articles/PMC3624763/pdf/nihms412728.pdf.

[19] Thomas Yankeelov and John Gore. “Dynamic Contrast Enhanced Magnetic Resonance Imaging in Oncology:Theory, Data Acquisition,Analysis, and Examples”. In: *Current Medical Imaging Reviews* 3.2 (2007), pp. 91–107. ISSN: 15734056. DOI: 10.2174/157340507780619179.

[20] Jun Yu Guo et al. “Dynamic contrast-enhanced magnetic resonance imaging parameters independent of baseline T10 values”. In: *Magnetic Resonance Imaging* 27.9 (2009), pp. 1208–1215. ISSN: 0730725X. DOI: 10.1016/j.mri.2009.05.015. URL: http://dx.doi.org/10.1016/j.mri.2009.05.015.

[21] Geoff J.M. Parker et al. “Experimentally-derived functional form for a population-averaged high-temporal-resolution arterial input function for dynamic contrast-enhanced MRI”. In: *Magnetic Resonance in Medicine* 56.5 (2006), pp. 993–1000. ISSN: 15222594. DOI: 10.1002/mrm.21066.

[22] Matthew R. Orton et al. “Computationally efficient vascular input function models for quantitative kinetic modelling using DCE-MRI”. In: *Physics in Medicine and Biology* 53.5 (2008), pp. 1225–1239. ISSN: 00319155. DOI: 10.1088/0031-9155/53/5/005.

[23] Allen D. Elster. *MRI Questions - DCE Parameters*. 2021. URL: https://mriquestions.com/dce-tissue-parmeters.html.

[24] Ishita Garg and Michael I. Miga. “Preliminary investigation of the inhibitory effects of mechanical stress in tumor growth”. In: *Medical Imaging 2008: Visualization, Image-guided Procedures, and Modeling*. Vol. 6918. 69182L. 2008, pp. 1–11. ISBN: 9780819471024. DOI: 10.1117/12.773376.

[25] C. Vuik et al. *Numerical Methods for Ordinary Differential Equations*. 2nd ed. Delft: Delft Academic Press, 2016. ISBN: 9789065623737.

[26] J. van Kan, A. Segal, and F. Vermolen. *Numerical Methods in Scientific Computing*. 2nd ed. Delft: Delft Academic Press, 2014. ISBN: 9789065623638.

[27] Angela M Jarrett et al. “Evaluating patient-specific neoadjuvant regimens for breast cancer via a mathematical model constrained by quantitative magnetic resonance imaging data”. In: *Neoplasia (United States)* 22.12 (2020), pp. 820–830. ISSN: 14765586. DOI: 10.1016/j.neo.2020.10.011.

[28] Thu Minh Le et al. “Numerical optimization applying trust-region reflective least squares algorithm with constraints to optimize the non-linear creep parameters of soft soil”. In: *Applied Mathematical Modelling* 41 (2017), pp. 236–256. ISSN: 0307904X. DOI: 10.1016/j.apm.2016.08.034. URL: http://dx.doi.org/10.1016/j.apm.2016.08.034.

[29] Thomas F. Coleman and Yuying Li. “An interior trust region approach for nonlinear minimization subject to bounds”. In: *SIAM Journal on Optimization* 6.2 (1996), pp. 418–445. ISSN: 10526234. DOI: 10.1137/0806023.

[30] David K. Woolf et al. “Arterial input functions in dynamic contrast-enhanced magnetic resonance imaging: Which model performs best when assessing breast cancer response?” In: *British Journal of Radiology* 89.1063 (2016). ISSN: 00071285. DOI: 10.1259/bjr.20150961.

[31] Xia Li et al. “A novel AIF tracking method and comparison of DCE-MRI parameters using individual and population-based AIFs in human breast cancer”. In: *Physics in Medicine and Biology* 56.17 (2011), pp. 5753–5769. ISSN: 00319155. DOI: 10.1088/0031-9155/56/17/018.

[32] Paul S. Tofts et al. “Estimating kinetic parameters from dynamic contrast-enhanced T1- weighted MRI of a diffusable tracer: Standardized quantities and symbols”. In: *Journal of Magnetic Resonance Imaging* 10.3 (1999), pp. 223–232. ISSN: 10531807. DOI: 10.1002/(SICI)1522-2586(199909)10:3<223::AID-JMRI2>3.0.CO;2-S.

[33] Nicole Wake et al. “Accuracy and precision of quantitative DCE-MRI parameters: How should one estimate contrast concentration?” In: *Magnetic Resonance Imaging* 52.May (2018), pp. 16–23. ISSN: 18735894. DOI: 10.1016/j.mri.2018.05.007. URL: https://doi.org/10.1016/j.mri.2018.05.007.

[34] Toru Chikui et al. “The principal of dynamic contrast enhanced MRI, the method of pharmacokinetic analysis, and its application in the head and neck region”. In: *International Journal of Dentistry* 2012 (2012), pp. 1–10. ISSN: 16878728. DOI: 10.1155/2012/480659.

[35] Paul Tofts. “T1-weighted DCE Imaging Concepts: Modelling, Acquisition and Analysis”. In: *Signal* 500.450 (2010), p. 400.

[36] Tofts P.S., Berkowitz B., and Schnall M.D. “Quantitative analysis of dynamic Gd-DTPA enhancement in breast tumors using a permeability model”. In: *Magnetic Resonance in Medicine* 33.4 (1995), pp. 564–568. ISSN: 0740-3194. DOI: 10.1002/mrm.1910330416.

[37] Rebecca Rakow-Penner et al. “Relaxation times of breast tissue at 1.5T and 3T measured using IDEAL”. In: *Journal of Magnetic Resonance Imaging* 23.1 (2006), pp. 87–91. ISSN: 15222586. DOI: 10.1002/jmri.20469.

[38] T. E. Merchant et al. “Application of a Mixed Imaging Sequence for MR Imaging Characterization of Human Breast Disease”. In: *Acta Radiologica* 34.4 (Jan. 1993), pp. 356–361. ISSN: 0284-1851. DOI: 10.1080/02841859309173257.

[39] Nkiruka C. Atuegwu et al. “Integration of diffusion-weighted MRI data and a simple mathematical model to predict breast tumor cellularity during neoadjuvant chemotherapy”. In: *Magnetic Resonance in Medicine* 66.6 (2011), pp. 1689–1696. ISSN: 15222594. DOI: 10.1002/mrm.23203.

[40] S. Oguri et al. “Pharmacokinetics of Carboplatin”. In: *Journal of clinical pharmacology* 28 (1988), pp. 208–215.

[41] Wim J.F. van der Vijgh. “Clinical Pharmacokinetics of Carboplatin”. In: *Clinical Pharmacokinetics* 21.4 (1991), pp. 242–261.

[42] Xia Li et al. “A nonrigid registration algorithm for longitudinal breast MR images and the analysis of breast tumor response”. In: *Magnetic Resonance Imaging* 27.9 (2009), pp. 1258–1270. ISSN: 0730725X. DOI: 10.1016/j.mri.2009.05.007.